Luiz Fernando Vieira

**Trajectory-Dependent Simulation of
Nanoparticle Translocation**

Tese de Doutorado

Thesis presented to the Programa de Pós–graduação em Engenharia Mecânica, do Departamento de Engenharia Mecânica da PUC-Rio in partial fulfillment of the requirements for the degree of Doutor em Engenharia Mecânica.

Advisor   : Prof. Paulo Roberto de Sousa Mendes
Co-advisor: Prof. Michael-Jon A. Hore

Rio de Janeiro
May 2022

PONTIFÍCIA UNIVERSIDADE CATÓLICA
DO RIO DE JANEIRO

Luiz Fernando Vieira

Trajectory-Dependent Simulation of Nanoparticle Translocation

Thesis presented to the Programa de Pós–graduação em Engenharia Mecânica da PUC-Rio in partial fulfillment of the requirements for the degree of Doutor em Engenharia Mecânica. Approved by the Examination Committee:

Prof. Paulo Roberto de Sousa Mendes
Advisor
Departamento de Engenharia Mecânica – PUC-Rio

Prof. Michael-Jon A. Hore
Co-Advisor
Case Western Reserve University – CWRU

Prof. Monica Feijó Naccache
Departamento de Engenharia Mecânica – PUC-Rio

Prof. Gary E. Wnek
Case Western Reserve University – CWRU

Prof. João Manuel Luis Lopes Maia
Case Western Reserve University – CWRU

Prof. Christopher Wirth
Case Western Reserve University – CWRU

Rio de Janeiro, May the 3rd, 2022

Luiz Fernando Vieira

Graduated in Materials Engineering by the Universidade Federal de Santa Catarina (UFSC) in 2010, obtained his Master degree in Mechanical Engineering at the same university (UFSC) in 2012. Researcher at the Instituto Nacional de Tecnologia (INT/MCTI) since 2013, where manages and executes Research and Development projects on polymer and composite materials, in partnership with industry.

Acknowledgments

This dissertation would not be a reality without the support and assistance of many people and organizations.

My deepest gratitude to my advisers, prof. Michael Hore and prof. Paulo Roberto de Sousa Mendes. I was very lucky to have advisers that not only were present and supportive when I needed them, but also encouraged following my ideas and contributed actively to the development of my scientific independence. There is still a lot to learn, and I hope to somehow keep learning from them for the years to come.

To my committee members, prof. Monica Naccache, prof. Gary Wnek, prof. João Maia and prof. Christopher Wirth, thank you for accepting the invitation and for all the help along the way.

Extra thanks to prof. Maia, for the conception and global coordination of the Macro/CAPES program, and to prof. Naccache for the coordination of the program on PUC-Rio.

I also received a lot of support from administrative staff: huge thanks to Theresa Claytor at CWRU, Carina Beline at PUC-Rio, Raquel Braz at INT, and surely many others that helped in that matter.

It would not be possible to me to join this program without the support of Dr. Marcia Gomes, at the time my direct boss at INT and today the institution's vice-director. I also thank my subsequent direct bosses, coordinators, and directors that continued supporting the leave of absence. A special thanks to my colleagues Dr. Valéria Costa and Djanira Costa for always encouraging me to continue my academic training.

I appreciate the support of Dr. Fernando Luís Peixoto and Dr. Aurélio Sabino Neto on my candidature in the program and for having mentored me in my beginning years in science.

During this program I was fortunate to meet people from all over the world, who helped me in several ways and made my life much more interesting; Members of the Hore Group, Dr. William Lenart, Dr. Xiaolong Lang, Dr. Yuan Wei, Weiwei Kong, William Oltjen and Alexandra Weinhofer;

Members of Macro/CAPES program, Dr. Erika Barcelos, Dr. Lucio Souza, Dr. Claudio Souza, Dr. Felipe Leis, Dr. Lucivan Barros, Dr. Gustavo Schinazi, Dr. Italo Silva, Dr. Irlaine Machado, Gabriel Pinto, Dr. Ana Maria Honorato and Gabriela Justino;

People from several research groups, Dr. Shaghayegh Khani, Dr. Vivek Pandey, Saeed Akbari, Yuki Kondo, Dana Klein, Dr. Thanyada Sukmanee, Sunsheng Zhu, Dr. Molin Guo and so many others that I certainly left out.

I would like to thank my parents for always having valued and supported my education throughout the years.

Finally, thank you to my beloved wife, Juçara, who believes in me more than I do - I could not have made it this far without her.

Abstract

Vieira, Luiz Fernando; de Sousa Mendes, Paulo Roberto (Advisor); J. A. Hore, Michael (Co-Advisor). **Trajectory-Dependent Simulation of Nanoparticle Translocation**. Rio de Janeiro, 2022. 128p. Tese de Doutorado – Departamento de Engenharia Mecânica, Pontifícia Universidade Católica do Rio de Janeiro.

This dissertation focuses on the transport of nanoparticles through nanopores - nanoparticle translocation - and how this phenomenon can be used as a characterization tool known as nanopore sensing. Nanoparticles not only occur widely in nature but also have been extensively engineered in academic research and industrial development. Due to their unique properties, nanoparticles are used in several industrial applications. Characterization tools that are accessible, easy to use, and robust are key for both research and quality control in nanoparticle science and technology. Rarely all these desirable characteristics are encountered in a single characterization tool. For example, Dynamic Light Scattering (DLS) is known to provide easy measurements of nanoparticle size but is prone to errors when analyzing dispersed and mixed distributions. On the other hand, direct visualization of the particles by Transmission Electron Microscopy (TEM) provides accurate information on particle size but is difficult to perform with high throughput and is prone to sampling bias. Nanopore sensing can, however, measure physical properties both at a single particle level and with high throughput. Experiments were successful in characterizing particle concentration, size, and charge. However, the experimental results are not always readily interpretable. In response, modeling and simulation tools are used to shed light on the complex relationships coming from the nanoscale environment. Despite the great amount of development in this area, there is still a lack of trajectory-dependent simulations that can effectively reproduce the pulses from the translocation of a freely interacting particle. Here, Poisson-Nernst-Planck formalism was combined with Machine Learning and Dynamic Monte-Carlo to form a simulation tool that captures the drift-diffusion motion of hard particles and the current pulses corresponding to these trajectories. Spheres and rods were simulated translocating pores of different dimensions. The simulations suggest inherent limitations in resolution due to the Brownian effect. Whereas previous studies were able to simulate only a few trajectories or estimated the statistics of the features using theoretical arguments, in this study hundreds of trajectories were simulated, calculating statistics directly from the population of results. The framework developed in this research can

be expanded to investigate other nanopore systems, helping the development of nanopore sensing.

Keywords

Nanoparticles; Diffusion; Electrophoresis; Translocation; Nanopore.

Resumo

Vieira, Luiz Fernando; de Sousa Mendes, Paulo Roberto; J. A. Hore, Michael. **Simulação da translocação de nanopartículas com dependência da trajetória**. Rio de Janeiro, 2022. 128p. Tese de Doutorado – Departamento de Engenharia Mecânica, Pontifícia Universidade Católica do Rio de Janeiro.

Esta tese trata do movimento de nanopartículas através de nanoporos – translocação – e como esse fenômeno pode ser utilizado como ferramenta de caracterização. Nanopartículas, não apenas ocorrem amplamente na natureza, mas também têm sido extensivamente aprimoradas em pesquisas acadêmicas e em desenvolvimento industrial. Devido às suas propriedades únicas, nanopartículas são utilizadas em diversas aplicações industriais. Ferramentas de caracterização que são acessíveis, fáceis de usar e robustas são fundamentais para pesquisa e controle de qualidade na ciência e tecnologia de nanopartículas. Raramente todas essas características desejáveis são encontradas em uma única ferramenta de caracterização. Por exemplo, o Espalhamento Dinâmico de Luz é uma técnica conhecida por ser de fácil execução, mas mede o tamanho de muitas partículas ao mesmo tempo, sendo propensa a erros em distribuições dispersas e mistas. Por outro lado, a visualização direta das partículas por Microscopia Eletrônica de Transmissão fornece informações precisas sobre o tamanho das partículas, mas é difícil de se realizar em larga escala e é propensa a viés de amostragem. O Sensoriamento via Nanoporos pode, no entanto, medir propriedades físicas em cada partícula individualmente e em alta escala. Experiências foram bem-sucedidas na caracterização da concentração, tamanho e carga elétrica de nanopartículas. No entanto, os resultados experimentais nem sempre são facilmente interpretáveis. Ferramentas de modelagem e simulação são usadas para esclarecer as relações complexas provenientes do ambiente em nanoescala. Apesar do grande desenvolvimento nesta área, simulações dependentes de trajetória que possam efetivamente reproduzir os pulsos da translocação ainda são escassas. Aqui, o formalismo de Poisson-Nernst-Planck foi combinado com aprendizagem de máquina e Monte-Carlo Dinâmico para formar uma ferramenta de simulação que captura o movimento de difusão e eletroforese, obtendo os pulsos de corrente correspondentes a essas trajetórias. Esferas e hastes foram simuladas translocando poros de diferentes dimensões. As simulações sugerem limitações inerentes na resolução devido ao efeito Browniano. Enquanto estudos anteriores conseguiram simular apenas algumas trajetórias ou estimar estatísticas usando argumentos teóricos, neste estudo foram calculadas centenas de trajetórias, calculando estatísticas diretamente da população de resultados. A estrutura desenvolvida nesta pesquisa pode ser

expandida para investigar outros sistemas, auxiliando no desenvolvimento do sensoriamento via nanoporos.

Palavras-chave

Nanopartículas; Difusão; Eletroforese; Translocação; Nanoporo.

Table of contents

List of figures

List of tables

1
Introduction

Nanoparticles not only occur widely in nature but also have been extensively engineered in academic research and industrial development. Due to their unique properties, nanoparticles are used in applications such as mechanical reinforcement in nanocomposites; for imaging and molecular diagnostics; as rheological, antimicrobial, and UV protective additives; as catalysts; in energy applications such as in solar cells or batteries; and in many other products (STARK et al., 2015).

Viewed as a miniaturized version of the Coulter Counter used for counting microparticles, nanopore sensing initially attracted the attention of researchers as a promising DNA sequencing platform. In addition to that, nanopore sensing is regarded as a feasible technique to characterize nanoparticles. Scattering characterization techniques such as Dynamic Light Scattering (DLS) are known to provide easy measurements from the average of many particles but are prone to errors in analyzing disperse and mixed distributions. On the other hand, direct visualization of the particles by Transmission Electron Microscopy (TEM) and other microscopy techniques, provide accurate information on
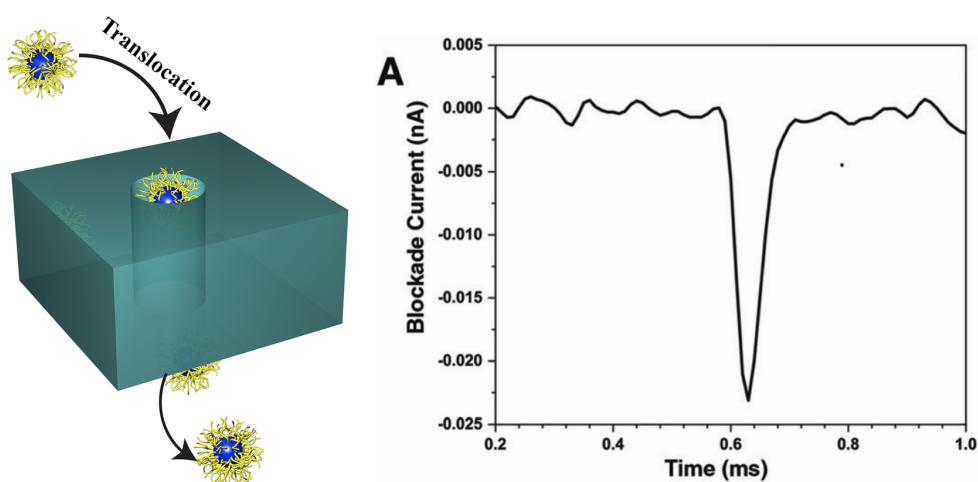
Figure 1.1: Electrical signal of a translocation event of a nanoparticle passing a 100 *mm* thick / 80 *nm* diameter nanopore. Current trace reproduced from (LENART et al., 2019).

Solid-state   **Punctured**   **Nanopipete**
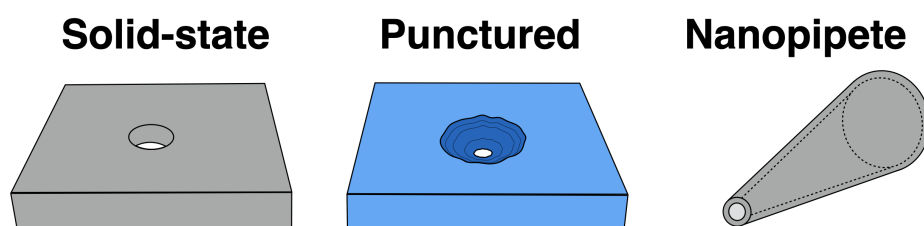
Figure 1.2:   Representation of typical types of membranes used in nanopore sensing.

particle size but are difficult to perform on large samples. Nanopore sensing can, however, measure physical properties both at a single particle level and at high throughput. Average values corresponding to the ensemble of objects can be obtained by analyzing the results of many translocation events.

Experimental translocation measurements have successfully studied several particle systems such as polymeric and inorganic spheres, rods, cuboids, vesicles, and virus-like particles. In particular, it has been successful in characterizing the size, surface charge, and concentration of particles in the submicrometer range. The stiffness of soft particles with these techniques has also been studied. Studies exploring these investigations will be discussed after presenting the technology in nanopore sensing and the physical aspects of particle and fluid motion in nanopores.

1.1
Technology for Nanopore Sensing of Nanoparticles

In this section, the principal components of a nanopore sensing device will be presented. Protocols like the ones from Graf et al. (2019) and Beamish et al. (2013), although not specific for nanoparticle characterization, provide additional information about the preparation and execution of the analysis.

1.1.1
Membranes

Presumably, the most important piece of a nanopore sensing device is the body that contains the nanopore, usually called by "membrane". Typical types of membranes used in nanopore sensing of nanoparticles are shown in Figure 1.2.

1.1.1.1
Planar, Solid-State

Planar, solid-state membranes are the most common class of membranes used in translocation experiments. Two main groups of membranes in this category can be distinguished: polymeric and inorganic membranes.

Inorganic membranes are created with semiconductor microfabrication techniques such as chemical/physical deposition, lithography, chemical/plasma etching and focused ion beam milling, using materials like silicon nitride, fused silica and glass. Zhang et al. (2015) reviewed the fabrication of nanochannels by many of these techniques. Due the precision and great level of maturity of microfabrication techniques, these membranes are extensively used in nanopore sensing of nanoparticles (AKAHORI et al., 2020; HE et al., 2017; TSUTSUI et al., 2018a; DEBLOIS; BEAN; WESLEY, 1977; HOLDEN; WATKINS; WHITE, 2012; LENART et al., 2019; HARMS et al., 2011; DARVISH et al., 2016; TSUTSUI et al., 2018b; TSUTSUI et al., 2016; DARVISH; GOYAL; KIM, 2015; SHI; RANA; ESFANDIARI, 2018; LEE et al., 2018; VENTA et al., 2014a; ARJMANDI et al., 2012; KISHIMOTO et al., 2020; TANAKA et al., 2016; ARIMA et al., 2018; ITO et al., 2004; COGLITORE et al., 2019; TAN et al., 2016; HOLDEN et al., 2011; BACRI et al., 2011; HALL et al., 2011; LEE et al., 2019; JUBERY et al., 2012; EDWARDS et al., 2015; WU et al., 2016).

Polymeric membranes are typically made of polyurethane sheets with pores made by puncture with a microneedle. These membranes are elastic and the pore diameter can be tunable using a commercial apparatus (see section 1.1.6). Several investigations were made using this type of membrane (WILLMOTT; YU; VOGEL, 2010; SIKORA; SHARD; MINELLI, 2016; URAM et al., 2006; ROBERTS et al., 2012; COUMANS et al., 2014; VOGEL et al., 2012; COLBY; COLSON; GRINSTAFF, 2013; SOMERVILLE et al., 2013; PLATT; WILLMOTT; LEE, 2012; LANE et al., 2015; VOGEL et al., 2011; ANDERSON et al., 2013; BLUNDELL; VOGEL; PLATT, 2016; KOZAK et al., 2012; MAUGI et al., 2020; RYUZAKI et al., 2017; WILLMOTT et al., 2010).

Carbon nanotubes were also used as nanopores. Ito et al. (2004) cast epoxy resin over a nanotube immobilized on TEM grids. The epoxy blocks were microtomed resulting in membranes with pores of 132 *nm* in diameter and around 1000 *nm* in length.

1.1.1.2
Nanopipettes

Nanopipettes, conical devices often made of glass or fused quartz (TERE-JÁNSZKY et al., 2014), present good electrical properties such as low capacitance and excellent chemical resistance. The diameters of the apertures are typically on the higher end of the spectrum of values found in the literature. For example, Holden et al. (2011) used nanopipets 750 to 1830 nm in diameter to investigate the deformation of poly(N-isopropylacrylamide-co-acrylic acid) (pNIPAm-AAc) microgels with diameter of 1140 nm. Lan et al. (2011c) used similar apparatus with an aperture diameter of 500 nm to sort a mixture of polystyrene beads with diameters of 160 nm and 320 nm.

1.1.1.3
Biological

Many biological protein pores are used in nanopore sensing, such as the Staphylococcal alpha hemolysin (α-HL), Mycobacterium smegmatis porin A (MspA), Aerolysin (AeL), bacteriophage phi29 motor, Cytolysin A (ClyA) and Outer membrane protein G (OmpG) (SHI; FRIEDMAN; BAKER, 2016). Although biological pores have a well-defined size and geometry, and have been extensively characterized, they have stability issues and the diameter of the constriction is too small (1 to 4 nm) for most nanoparticles of interest. Such pores are more commonly explored for sensing DNA and other macromolecules.

Research of nanoparticle sensing with biological nanopores usually uses the nanoparticle as a carrier for a macromolecule of interest. Campos et al. (2013), however, analysed 3-mercapto-1-propanesulfonate (MPSA)-modified-gold nanoparticles using the α-HL pore. Although the particles cannot fully translocate the pore, it is believed that the particles could enter the vestibule of the pore and alter the current values. They found four distinct levels of the current drop, credited to variations in size and surface charge of the particle population, however, not being able to define the characteristics of these sub-populations.

1.1.1.4
Miscellaneous Nanopores

Alternative methods for fabricating nanopores are being studied. Chantiwas et al. (2011) reviewed the fabrication of polymer-based nanofluidic using both elastomeric and thermoplastic materials, whereas (MENARD; RAMSEY, 2011) reported the fabrication of Sub-5 nm nanochannels using focused ion

beam milling. Peng e Li (2016) created nanochannels by replicating nanoc-racks generated on the surface of a polystyrene sheet.

1.1.1.5
Surface Modification

Coating of silicon nitride chips with poly(dimethyl siloxane) (PDMS) (TABARD-COSSA et al., 2007) or polyimide (TSUTSUI et al., 2018a) has been done previously to lower the electrical noise of the system. In this case, an access region of few micrometers around the pore is left without coating to avoid clogging the pore with the coating. Surface modification of the pore itself, such as silanization (PRABHU et al., 2010; LAN et al., 2011c; TAN et al., 2016) and with other coated species (EGGENBERGER; MAYER, 2019; YUSKO et al., 2011) has been explored as a tool to prevent adhesion and minimize clogging by the nanoparticles, as well as a way to add to the pores the capacity of controllable gating as a function of a stimulus like pH (ZHANG et al., 2013) or temperature (GROOT et al., 2013).

1.1.2
Cells

Nanopore sensing membranes are often tiny fragile structures that need to be supported by a body that contains the electrolyte solution and the electrodes. Nanopipettes are usually connected to specialized holders, while planar membranes are assembled to so-called "flow cells" or "solution cells".

The most common design of a solution cell is composed of two blocks (halves) containing the solution chambers, with the membrane sandwiched between them with the aid of sealing components such as O-rings or gaskets. Some groups use poly(tetrafluoroethylene) (PTFE) (BEAMISH et al., 2012; LENART et al., 2019; TAN et al., 2016) cells, while others advocate to transparent materials as poly(methyl methacrylate) (PMMA) (GRAF et al., 2019) and polycarbonate (PC) (PRABHU et al., 2010; DARVISH; GOYAL; KIM, 2015; LEE et al., 2018), as such choices allow the experimenter to observe of the presence of bubbles and any misalignments. PDMS rubber is also used as a cell using the two-halves-design similar to the PMMA and PC ones (HE et al., 2017), or using an integrated microfluidic approach (ROMAN et al., 2017; ARIMA et al., 2018; TANAKA et al., 2016).

1.1.3
Electrolyte Solution

An aqueous solution of potassium chloride (KCl) is the standard electrolyte solution in nanopore sensing of nanoparticles. The concentration of the salt varies from 10 to 1000 $mmol/L$. There are a few exceptions, as Tsutsui et al. (2015) that used phosphate-buffered saline (PBS) solutions to investigate the nanopore sensing of viruses. Ethylenediamine tetraacetic acid (EDTA) and Triton-X®are also often used to improve the stability of the suspensions. The concentration of the dispersed particles varies wildly, from 10^{-15} to 10^{-9} mol/L (i.e., fM to nM).

1.1.4
Electrodes

In order to measure the ionic current, Ag/AgCl electrodes on each side of the cell are used. With the applied voltage, oxidation occurs in one electrode and reduction in the other, so the system acts as a reversible redox reaction. To produce the electrodes, silver wires are chlorinated by submersion in bleach (sodium hypochlorite) solution or by applying a voltage to the wires in KCl solution. One exception to the commonly used Ag/AgCl system is the device from Fraikin et al. (2011), where a voltage divider is used and gold electrodes measure the voltage changes across the nanopore.

1.1.5
Electronics

It is a challenging task to record the translocation pulses with a high signal-to-noise ratio, since the ionic currents are in order of picoamperes (pA). Many authors use patch-clamp devices, such as the commonly used Axopatch 200B (Axon Instruments). Other options include the Chimera VC100 (Chimera Instruments) which provides higher bandwidth (up to 1MHz, compared to 100kHz limit from Axopatch). Other integrated solutions (see section 1.1.6) such as qNano and eNPR are also used. It is common practice to perform the experiments in a Faraday cage on an anti-vibration table to minimize electronic and mechanical noise.

1.1.6
Commercial Solutions

The advances in the nanopore sensing field are bringing commercial solutions that promise to expand the utilization of nanopore sensing. Most of the experiments reported in the literature were done with expensive electronics

and handmade cells whose cleaning and assembly are difficult, laborious, and prone to error. It is expected that with the advancement of integrated commercial systems, although with the risk of losing openness of the data treatment, the experiments will become cheaper, more reliable, and repeatable. In DNA translocation there are now commercial systems such as the ones from Oxford Nanopore Technologies (<https://nanoporetech.com>) with a great level of maturity. For particle translocation, Izon qNano (<https://izon.com/>) has been used in several works using its tunable pores. Bacri et al. (2011) used Nainon Port-a-patch (https://www.nanion.de) to analyse polystyrene nanoparticles. Recently, Niedzwiecki et al. (2020) used eNPR Nanopore Reader (<https://elements-ic.com>), a portable integrated system to analyse antarctic dirt particulates. These devices offer an integrated solution with higher portability.

1.1.7
Data Analysis

Analog gain, typically 10x, and filtering, such as a 10 kHz low-pass Bessel filter, are often applied to the signal before digitization and recording. Robinson et al. (2018) discussed the effect of filtering on translocation pulses, such as attenuation of the signal strength and loss of temporal resolution. Additional (digital) low-pass filtering and smoothing using a moving average (MCMULLEN et al., 2014) are also commonly applied.

For identification of the events and extraction of event features like duration and magnitude, several groups developed in-house code, while open software such OpenNanopore (RAILLON et al., 2012), MOSAIC (FORSTATER et al., 2016), eventPro (BANDARA et al., 2021) and easyNanopore (TU et al., 2021) are helping to improve and standardize the analysis. Wen, Dematties e Zhang (2021) recently discussed the different signal processing algorithms for nanopore sensors.

1.2
Motion in Nanopores

Nanoparticle movement in confined spaces depends on several factors. The combination of these factors in distinct phenomena is described below.

1.2.1
Brownian Motion

Nanoparticles in suspension suffer random motion as a result of the collisions of solvent molecules. Even without any external electric field, translo-

cation can occur with the dynamics dictated by the diffusion coefficient of the particle in the suspension.

Einstein showed that a particle in Brownian motion follows a Gaussian distribution with zero mean and variance of:

$$\overline{x}^2 = 2Dt \tag{1-1}$$

where D is the translational diffusion coefficient of the particle and t the time elapsed. The diffusion coefficient is commonly related to the particle and solvent properties by the Stokes–Einstein equation:

$$D = \frac{K_b T}{2n\,\pi\,\eta\,R_h} \tag{1-2}$$

where k_B is Boltzmann's constant, n the dimensionality of the diffusive process (*e.g.*, $n = 3$ in 3 dimensions), T the temperature, η the solvent viscosity, and R_h the hydrodynamic radius of the particle. It is important to note that the DLS measurements use the same expression to estimate the hydrodynamic radius of a particle due to Brownian motion, estimating the diffusion coefficient from the autocorrelation curve of the measured scattering intensity.

1.2.2
Electrophoresis

1.2.2.1
Electrical Double Layer

Surfaces in contact with an electrolyte solution can be charged, due to the dissociation of surface groups or adsorption of ions, for example. Charged surfaces give rise to an electrostatic potential (Ψ) and an associated profile of ion concentration near the surface, as the simplified representation in Figure 1.3 shows. Near the surface, there is a net enrichment of the counterions in the region known as the Electrical Double Layer (EDL). Counterions closely attached to the surface form an immobile region called the Stern layer. In absence of other charged surfaces, going far from the surface the concentration of both ionic species converges to the bulk concentration. In this region, the "diffuse layer," the ions are more loosely attached to the solid surface and more affected by the thermal motion. When there is a relative motion of the fluid and the charged surface, a region formed by the Stern layer and some portion of the diffuse layer remains attached to the surface, whereas the remaining portion of the diffuse layer can be displaced. The location of the transition from the fixed to the movable region is called the "shear plane" or "slipping plane".
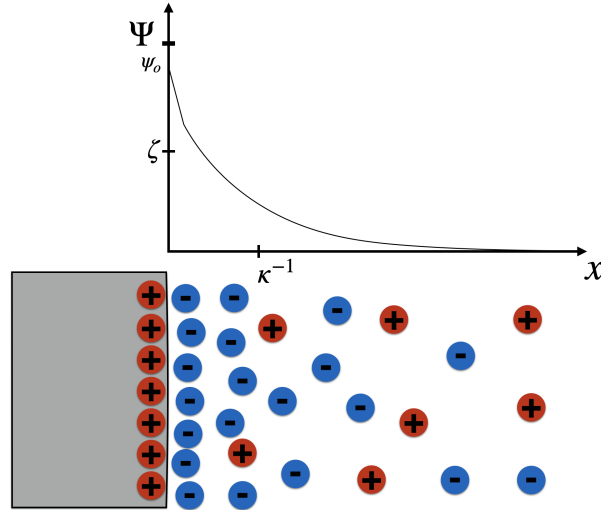
Figure 1.3: Simplified representation of the ionic distribution near a charged surface immersed in an electrolyte solution. The plot shows the corresponding electrostatic potential, highlighting the potential at the surface (Ψ_o), the zeta potential (ζ) and the Debye length (κ^{-1}).

The electrostatic potential decays exponentially to zero, with a characteristic length κ^{-1}, the Debye length, in order of few nanometers. Its reciprocal, the Debye–Hückel parameter κ is defined as:

$$\kappa = \sqrt{\frac{2N_A e^2 I}{\epsilon_o \epsilon_r k_b T}} \tag{1-3}$$

where e is the elementary charge, N_A the Avogadro's number, k_b the Boltzmann constant, T the absolute temperature and $\epsilon_o \epsilon_r$ the solution permittivity. The ionic strength of the solution, I, is given by

$$I = \frac{1}{2} \sum c_i z_i^2 \tag{1-4}$$

where c_i and, z_i are the molar concentration and valence of ion i, summed over all ions species of the solution. For monovalent 1:1 electrolytes, such as KCl, the ionic strength is equal to the molar concentration of salt.

The potential at the shear plane is defined as the zeta potential (ζ). The zeta potential is very important in the characterization of charge in nanoparticles, since it is correlated with the particle mobility.

1.2.2.2
Nanoparticle Mobility

Charged nanoparticles experience an electrostatic Coulomb force in the presence of an external electric field. The particles encounter viscous drag from the fluid molecules, causing them to reach a steady velocity. Additionally, the osmotic flow of the counterions on the EDL travel in the opposite direction

of the particle, retarding its velocity. The particle electrical mobility μ_e is the ratio between the electrophoretic velocity v_e and the field strength (E):

$$\mu_e = \frac{v_e}{E} \tag{1-5}$$

Electrophoretic theory relates the electrophoretic motion with the properties of the particle, the solution, and the field. For a non-conductive spherical particle, relations such as those from Smoluchowski, Hückel, and Henry, are widely used and are valid under the assumption of low potential ($\zeta < k_B T/e \approx$ 25 mV). For higher potential values, numerical schemes such as those from O'Brien e White (1978) and analytical equations are also available. Henry's equation (Equation 1-6) describes the mobility as a function of particle permitivity $\epsilon\epsilon_o$, zeta potential ζ and solvent viscosity η:

$$\mu_e = \frac{\epsilon\epsilon_0 \, \zeta}{\eta} f(\kappa a) \tag{1-6}$$

where $f(\kappa a)$ is a function of the Debye–Hückel parameter k and particle radius a that can be approximated by(OHSHIMA, 1994):

$$f(\kappa a) = \frac{2}{3}\left[1 + \frac{1}{2\left(1 + \frac{2.5}{\kappa a\{1+2\exp(-\kappa a)\}}\right)^3} \right] \tag{1-7}$$

Swan e Furst (2012) proposed an even simpler approximation as:

$$f(\kappa a) = \frac{16 + 18\kappa a + 3(\kappa a)^2}{16 + 18\kappa a + 2(\kappa a)^2} \tag{1-8}$$

Grahame's equation relates the surface charge density σ with the potential at the surface of the particle. In low potential, and approximating the potential at the surface as the value of zeta potential, a very simple expression can be obtained:

$$\sigma = \epsilon_0 \epsilon_r \kappa \zeta \tag{1-9}$$

A more accurate expression valid in low potentials and $\kappa a > 0.5$ (DOANE et al., 2011):

$$\sigma_{NP} = \epsilon\epsilon_o \frac{k_b T}{ze} kT/(z*e)\kappa 2\sinh(\frac{\zeta ze}{2k_b T}) + \frac{4}{\kappa r_{NP}} 2\tanh\frac{\zeta ze}{4k_b T} \tag{1-10}$$

The total charge is the product of surface charge density and surface area A:

$$q = \sigma A \tag{1-11}$$

These expressions are used for the estimation of zeta potential and surface charge from the measurement of electrical mobility of particles by Phase Analysis Light Scattering (PALS).

In case of cylindrical particles, the mobility averaged over a random distribution of orientation can be calculated by (OHSHIMA, 2016):

$$\mu = \frac{\epsilon \epsilon_0 \, \zeta}{\eta} \left(\frac{1 + 2 f(\kappa a)^{cyl}}{3} \right) \tag{1-12}$$

where

$$f(\kappa a)^{cyl} = \frac{1}{2} \left[1 + \frac{1}{\left(1 + \frac{2.55}{\kappa a \{ 1 + \exp(-\kappa a) \}} \right)^2} \right] \tag{1-13}$$

1.2.3
Electroosmotic Flow

When a tangential electrical field is applied to a charged surface, as it is to the nanochannel wall in a translocation measurement, the ions on the diffuse part of the double layer can move towards the electrode of opposite charge and drag the fluid with them. The result is a net movement of the fluid referred to as electroosmotic flow (EOF). The strength of EOF will depend on the pore diameter and surface charge, the electric field, as well as on the ionic strength and viscosity of the electrolyte solution. The direction of the flow can be the same or the opposite of the expected translocation direction depending on the charge of the nanoparticle.

In low potential ($|\zeta| < k_B T / e$), using the Debye–Hückle approximation, the velocity profile of a fluid near a plane charged wall can be described as:

$$v_x(y) = \mu_{eo} E (1 - e^{-\kappa y}) \tag{1-14}$$

where y is the direction orthogonal to the wall surface, x is the direction of the applied field and perpendicular to the wall surface, E is the field strength in the x direction, and the term μ_{eo} is referred to as the electroosmotic mobility, $\mu_{eo} = \epsilon \epsilon_o \zeta / \eta$. The velocity profile is very flat in the regions far from the wall, with a sharp decay in the EDL to zero (non-slip condition) at the wall surface.

If the EDL is small and the velocity decay near the wall can be neglected (treating the profile as an ideal plug flow), a further approximation can be made, leading to the Helmholtz–Smoluchowski equation:

$$v_x = \mu_{eo} E \tag{1-15}$$

1.2.4
Pressure-Driven Flow

Instead of an electrostatic potential, the application of a pressure field can be used to create a fluid flow through the nanopore that can drag a nanoparticle to a translocation event.

From the Hagen–Poiseuille equation, the velocity profile in a cylindrical channel of length L and radius R, arising from a pressure difference ΔP is

$$v(r) = \frac{1}{4\eta}\frac{\Delta P}{L}(R^2 - r^2) \qquad (1\text{-}16)$$

with the mean velocity $\bar{v}$ being

$$\bar{v} = \frac{d_P^2}{32\eta L_P}\Delta P \qquad (1\text{-}17)$$

Several research works used the pressure difference as the main drive of the translocation, while other groups use the combined or sole effect of the applied external electrical potential difference.

1.2.5
Other (frequently negligible) Factors

Several other factors can be frequently and safely neglected. In the submicrometer range, the effect of gravity usually is not relevant. Additionally, the Reynolds's number of the flow in the experiments is very low, so the effect of inertia is also negligible. Finally, van der Waals interactions between the particle and pore wall are usually restricted to very small distances and often disregarded. Depending on the surface chemistry of the particle and channel, however, other interactions can be important to consider.

1.2.6
Timescales

Observing the current signal from the experiments, three main timescales are observed (MUTHUKUMAR, 2011). Figure 1.4 shows typical features found on the current signal and associated time scales.

The first (longest) time scale (t_1), the time between events, is the inverse of the capture rate. This information can be related to particle concentration. Next, the duration of the pulse, "dwell time", is often defined as the width of the pulse at half height (t_2). Associated with the dynamic of the particles, it can be used to determine the size and charge of the particles. Finally, characteristic features in the pulse signal can define a shorter time scale (*e.g.*, t_3) that can be related, for example, to multi-particle events (LENART et al., 2019) or geometric features of the particle (RYU et al., 2019; TANAKA et al., 2016).

1.3
Characterization of Nanoparticles by Nanopore Sensing

Experimental translocation measurements have successfully studied polymeric and inorganic spheres (MAUGI et al., 2020; KISHIMOTO et al., 2020;
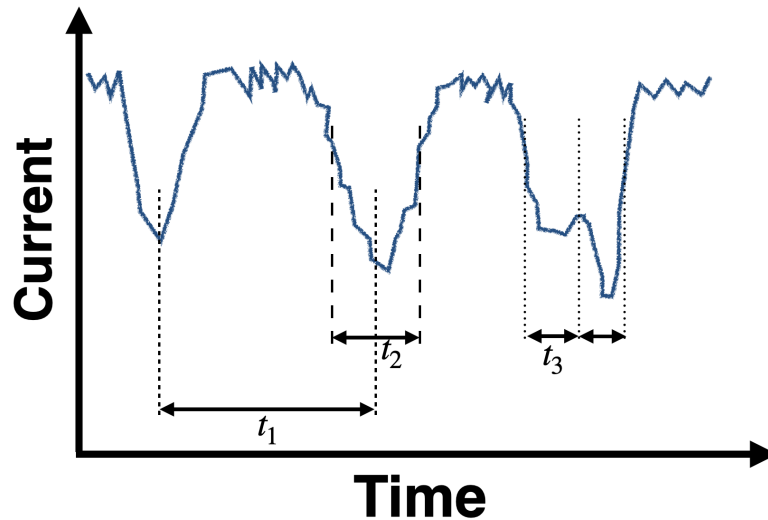
Figure 1.4: Hypothetical current trace with signal features and associated time-scales: time between events (t_1), dwell time (t_2) and duration of features intra-event (t_3).

NIE et al., 2019; LEE et al., 2019; GRABAREK et al., 2019; LIOT et al., 2018; TSUTSUI et al., 2018b; LEE et al., 2018; RYUZAKI et al., 2017; BLUNDELL; VOGEL; PLATT, 2016; TSUTSUI et al., 2015; TAN et al., 2016; EDWARDS et al., 2015; LAN et al., 2014; TEREJÁNSZKY et al., 2014; KOZAK et al., 2012; ROBERTS et al., 2012; PEVARNIK et al., 2012; ARJMANDI et al., 2012; LAN; WHITE, 2012; VOGEL et al., 2012; JUBERY et al., 2012; LAN et al., 2011a; VOGEL et al., 2011; LAN et al., 2011b; PRABHU et al., 2010; WILLMOTT; YU; VOGEL, 2010; WILLMOTT et al., 2010; ITO et al., 2004; BACRI et al., 2011; SIKORA; SHARD; MINELLI, 2016; AKAHORI et al., 2020; COGLITORE et al., 2019; HE et al., 2017; KIM et al., 2014; VENTA et al., 2014a; WANG; BENICEWICZ, 2013; PLATT; WILLMOTT; LEE, 2012; COLBY; COLSON; GRINSTAFF, 2013), rods (PLATT; WILLMOTT; LEE, 2012; VENTA et al., 2014a; ZHANG et al., 2016), carbon nanotubes (HALL et al., 2011), cuboids (SI et al., 2020), vesicles (LEE et al., 2019; LANE et al., 2015; GRABAREK et al., 2019; LIOT et al., 2018; DARVISH et al., 2016; COUMANS et al., 2014; HOLDEN; WATKINS; WHITE, 2012) and virus-like particles (VOGEL et al., 2011; ARIMA et al., 2018; DEBLOIS; BEAN; WESLEY, 1977; HARMS et al., 2011; WU et al., 2016; FRAIKIN et al., 2011; URAM et al., 2006; TEREJÁNSZKY et al., 2014; DARVISH; GOYAL; KIM, 2015; MCMULLEN et al., 2014; MCMULLEN; TANG; STEIN, 2017). Figure 1.5 shows some parameters and properties of particles and membranes used in nanopore sensing experiments gathered from the literature. The review was limited to work that used particles with diameters in the submicrometer range,
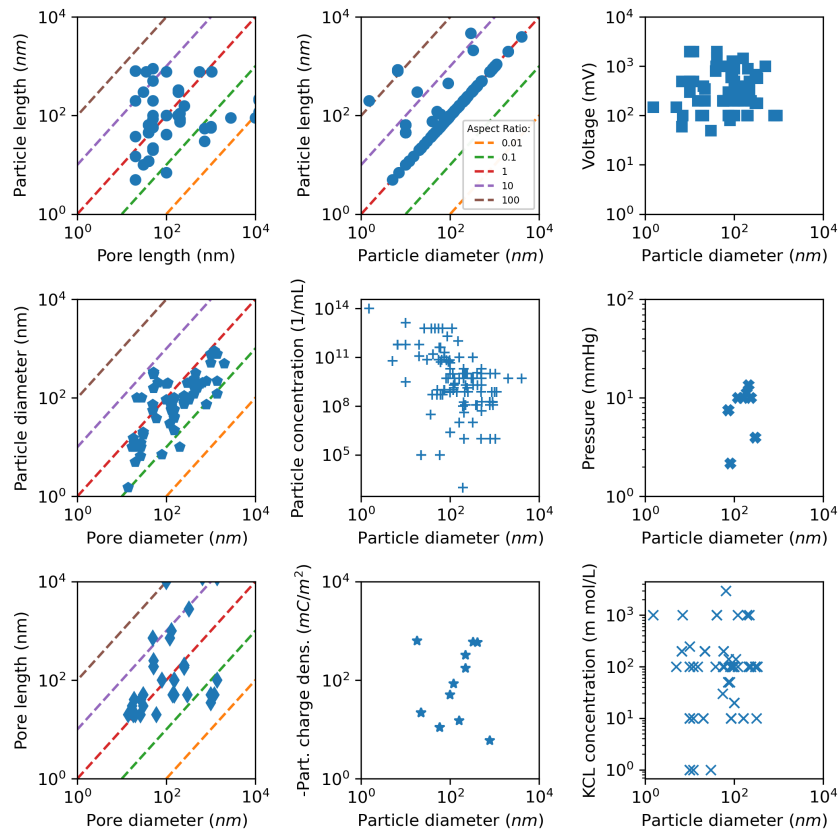
Figure 1.5: Properties of nanopore sensing used in the literature.

with a minimum diameter of a few tens of nanometers. Most of the experiments used spherical particles, although some virus particles with aspect ratios up to 100 were also found in the literature. Particle concentration varies widely across 10 orders of magnitude. Most of the pores have aspect ratio close to one, even though deep and shallow pores (with respect to their diameters) are also being studied.

Nanopore sensing has been successful in characterizing the size (MAUGI et al., 2020; LENART et al., 2019; LEE et al., 2019; LEE et al., 2018; MCMULLEN; TANG; STEIN, 2017; BLUNDELL; VOGEL; PLATT, 2016; SIKORA; SHARD; MINELLI, 2016; SOUZA; CIMINELLI; MOHALLEM, 2016; COUMANS et al., 2014; MCMULLEN et al., 2014; TEREJÁNSZKY et al., 2014; SOMERVILLE et al., 2013; JUBERY et al., 2012; KOZAK et al., 2012; VOGEL et al., 2012; BACRI et al., 2011; VOGEL et al., 2011; FRAIKIN et al., 2011; WILLMOTT; YU; VOGEL, 2010; ITO et al., 2004), surface charge (MAUGI et al., 2020; LEE et al., 2018; MCMULLEN; TANG; STEIN, 2017; BLUNDELL; VOGEL; PLATT, 2016; SIKORA; SHARD; MINELLI, 2016; MCMULLEN et al., 2014; VENTA et al., 2014a; VENTA et al., 2014b; SOMERVILLE et al., 2013; KOZAK et al., 2012; VOGEL et al., 2012; WILLMOTT; YU; VOGEL, 2010) and concentration (BACRI et al., 2011;

FRAIKIN et al., 2011; WILLMOTT; YU; VOGEL, 2010; WILLMOTT et al., 2010) of particles in the submicrometer range. The stiffness of soft particles has also been studied (PEVARNIK et al., 2013; HOLDEN et al., 2011; HOLDEN; WATKINS; WHITE, 2012). Wen et al. (2018) and Tsutsui et al. (2019) performed experiments with multipore membranes, analyzing the effect of the number of pores on the capture rate and signal/noise ratio.

1.3.1
Measurement of Size

The size of nanoparticles is mainly associated with the magnitude of the electrical pulses. We can use Ohm's law to relate the current i with the voltage V. In a first simplified approximation, the equivalent circuit is formed by a single resistor, the nanopore:

$$i = \frac{V}{R} = GV \tag{1-18}$$

with the pore resistance R (reciprocal of the pore conductivity, G) as:

$$R_o = \rho_e \frac{L}{A} \tag{1-19}$$

where L is the pore length, A the cross-sectional area, and ρ_e is the solution resistivity.

The presence of a particle inside the pore affects the resistivity. Models relating the properties of the particles and pores with the expected change in resistivity will be revisited and derived in 3. Further improvement of modeling includes the resistance of the access and exit regions. By symmetry, access and exit resistances can be replaced by twice the access resistance:

$$R = R_{access} + R_{pore} + R_{exit} = R_{pore} + 2\,R_{access} \tag{1-20}$$

For a cylindrical pore with diameter d_P, classic expression for the access resistance is provided by Hall (1975):

$$R_{access} = \frac{\rho_e}{2d_P} \tag{1-21}$$

Another approach to include the effecto of access resistance is to consider an effective pore length L_c that is greater than the geometrical length (DEBLOIS; BEAN, 1970):

$$L_c = L + 0.785\,d_P \tag{1-22}$$

1.3.2
Measurement of Surface Charge

The surface charge can be related with the velocity of the particle translocating the pore, and therefore, with the translocation time τ:

$$\overline{v} = \frac{L}{\tau} \tag{1-23}$$

As was shown in the section 1.2, several factors can affect the velocity of the particle:

$$\overline{v} = v_{\text{pressure}} + v_{\text{electrophoresis}} + v_{\text{EOF}} + v_{\text{diffusion}} \tag{1-24}$$

Different equations can be proposed depending on the degree of simplification of each phenomenon. Sun e Crooks (2000) proposed the following equation, where negative term indicated that EOF occurs in inverse direction of the field for a negatively charged surface:

$$\overline{v} = \frac{d_P^2}{32\eta L_P}\Delta P + \mu\frac{\Delta V}{L_p} - \frac{\epsilon\zeta_P}{4\pi L_p}\Delta V + \frac{D_s}{c_s L_P}\Delta c_s \tag{1-25}$$

As discussed earlier (section 1.2), knowing the velocity and the electrical field, the mobility is found, which can be used to estimate the zeta potential and finally the surface charge.

1.3.3
Measurement of Concentration

Considering that the particle concentration c_{NP} remains the same in bulk and in the pore, the concentration can be estimated by measuring the velocity and the particle flux J_{NP}.

$$c_{NP} = \frac{\text{Particle flow}}{\text{Fluid flow}} = \frac{J_{NP}}{Q} = \frac{J_{NP}}{\overline{v}A} = \frac{4J_{NP}}{\overline{v}\pi d_P^2} \tag{1-26}$$

1.3.4
Intra-Event Time Scales and Single/Multiparticle Translocation

Multiparticle translocation can result in pulses with distorted shapes and in the reduction of the number of pulses counted, affecting all aspects of the measurements. Considering particles without interactions with each other and the pore, it is possible to use Poisson statistics to estimate the fraction of singlets as e^γ, where γ is the concentration in terms of the average number of particles per pore volume (DEBLOIS; BEAN; WESLEY, 1977).

1.4
Modeling and Simulation of Nanoparticle Translocation

Despite advances in hardware (NIEDZWIECKI et al., 2020) and data treatment (MAUGI et al., 2020; ARIMA et al., 2018; TANIGUCHI, 2020), it can be challenging to establish unequivocal relations between the current pulses that are measured and the properties of interest. Modeling and simulation techniques are very important tools to help unveil the complex phenomena present during translocation. To this end, several simulation methods have been used successfully to understand aspects of particle translocation. Langevin Dynamics simulations were utilized to study the capture (QIAO; SLATER, 2020), entrance and translocation (WU et al., 2016; MCMULLEN et al., 2018; MCMULLEN et al., 2014) of slightly flexible, anisotropic particles, such as the Tobacco Mosaic Virus (TMV) viral capsid. Additionally, Monte Carlo simulation schemes were also used to explore the capture radius (QIAO; IGNACIO; SLATER, 2019) and diffusivity of a particle under confinement (MICHAELIDES, 2017). Finally, Lattice Boltzmann simulations were developed to deal with the electrokinetic problem (KURON et al., 2016) and were used to study the translocation of a double helix of DNA (REBOUX et al., 2006). The majority of the literature on this topic, however, has relied on simulations using the Finite Element Method (FEM) (MAUGI et al., 2020; LAN; WHITE, 2012; LAN et al., 2014; QIN; ZHE; WANG, 2011; LIU; PEN-NATHUR; MEINHART, 2014; QIAN; WANG; AFONIEN, 2006; VENTA et al., 2014b; JUBERY et al., 2012; ZHANG et al., 2016; DARVISH et al., 2016; LAN et al., 2011b; LAN et al., 2011c; PEVARNIK et al., 2013; TSUTSUI et al., 2015; LAN et al., 2011a; RYUZAKI et al., 2017).

When trying to relate particle properties with the current signal, each particle position in its trajectory usually represents a single simulation run. Most of the studies consider either a single, unique simulation with the particle at the center of the pore or a collection of runs with particles placed within a straight-line trajectory. For example, (ZHANG et al., 2016) observed features in the electrical pulse related to the rotational tumbling of individual nanorods. Their FEM simulation could replicate qualitatively the signal shape, but the position orientation of the rods was set manually at each run. Tsutsui et al. (2015) observed distinct populations of current signals investigating polystyrene latex particles translocating through low aspect ratio pores. FEM simulations of particles in different positions along the pore indicate trajectory-dependent currents, notably due to the off-axis displacement of the particles. The authors performed cross-sectional (2D) Brownian Dynamics simulations to investigate the degree of temporal fluctuations in the particle center position

due to Brownian motion. They state, however, that "*simultaneous simulation of the particle dynamics and the ion transport would shed further light on this intriguing phenomenon*" (TSUTSUI et al., 2015).

1.5
Dissertation Proposition and Outline

Motivated by this body of prior work, this work proposes a procedure to simulate simultaneously the drift-diffusion trajectories and the current response to these trajectories. The approach is to use Dynamic Monte Carlo (DMC) simulations that are coupled to pre-calculated potentials. First, the electrostatic potential and ionic current are computed for several configurations of pore/particle properties and particle position, by solving Poisson–Nernst–Planck (PNP) equations. These results were used either to perform a linear interpolation of the tabulated values or to train neural networks that captured the input-output relationship. Finally, Dynamic Monte Carlo is used to update the particle position and to compute time-resolved trajectories, mapping the ionic current related to each position for a large ensemble of particles. By simulating several configurations of particle diameter, particle mobility, and pore length, it is shown how the thermal fluctuations can affect the resolution and robustness of the measurements and how these results compare to experimental translocation measurements.

The dissertation is organized as the following:

Computational and experimental methods are presented in **Chapter 2**. **Chapter 3** presents simple models for current prediction in nanopores. **Chapter 4** presents the simulation of spherical particles in a uniform electrostatic field. First, an analytical expression for the expected mobility is derived based on the arguments of the metropolis algorithm and the time scaling of the DMC simulation. Those values are confronted with values obtained from the simulations, and a charge re-scaling is proposed. **Chapter 5** proceeds with the spherical particles, simulating translocation phenomena. Using the potential described by a neural network, different configurations are discussed and it is shown how the time-resolved simulations can help to address challenges in translocation interpretation. **Chapter 6** expands the simulation tool here developed to study the translocation of an anisotropic particle in a uniform electrostatic field. **Chapter 7** then shows the simulation of nanorods, comparing the process with spheres. Finally, **Chapter 8** summarizes the results and conclusions, and gives directions for future studies.

2
Methods

2.1
Poisson–Nernst–Planck by Successive Over-Relaxation (SOR)

2.1.1
Poisson-Nernst-Planck (PNP) Framework

The electrostatic potential and ionic current through the nanopore were calculated using the Poisson-Nernst-Planck (PNP) formalism. In this approach, the electrostatic potential is obtained by solving the Poisson equation, and the solution is then used to solve the Nernst-Planck equation for the ion concentrations and fluxes throughout the system. The process is performed self-consistently until the error falls below a desired threshold. For our calculations, the process was repeated until the error in the electrostatic potential and ion concentrations fell below 10^{-7} V and 10^{-6} mol/L, respectively. The calculations were performed on a cubic system with $L_x = L_y = L_z = 500$ nm, with each dimension discretized into 128 grid points. This resulted in a spatial resolution of $\Delta x = \Delta y = \Delta z \approx 4$ nm. The PNP equations were solved using an in-house code written in C++ using the NVIDIA CUDA libraries, and the calculations performed on NVIDIA Tesla P100 and V100 GPUs.

Within the PNP framework, the electrostatic potential throughout the system, $\phi(\mathbf{r})$, is first calculated by solving the Poisson equation:

$$\nabla \cdot [\epsilon_r(\mathbf{r})\nabla\phi(\mathbf{r})] = -\frac{\rho_m(\mathbf{r})}{\epsilon_0} \tag{2-1}$$

where $\epsilon_r(\mathbf{r})$ is the relative permittivity at position $\mathbf{r}$ in the system, $\rho_m(\mathbf{r})$ is the mobile charge density at that position, and ϵ_0 is the permittivity of free space. Regions belonging to the solution have $\epsilon_r(\mathbf{r}) = 80$ while regions inside the membrane or nanoparticle have $\epsilon_r(\mathbf{r}) = 2$. The Poisson equation was solved using a successive over-relaxation (SOR) algorithm with the boundary conditions that $\phi(\mathbf{r}) = V_b = 100$ mV at $z = 500$ nm, and $\phi(\mathbf{r}) = 0$ mV at $z = 0$ nm. The initial condition for $\phi(\mathbf{r})$ was $\phi(\mathbf{r}) = 0$ throughout the system, except at the boundaries. We simulated a single membrane with thickness L_p, containing a cylindrical nanopore with diameter $d_P = 60$ nm, centered in the system, and oriented perpendicular to the xy-plane of the system.

For simplicity, the nanoparticle and membrane were modeled as uncharged surfaces.

The electrostatic potential was then used to solve the Nernst-Planck equation:

$$\nabla . \left[D_i \nabla c_i(\mathbf{r}) + \frac{D_i Z_i}{k_B T} c_i(\mathbf{r}) \nabla \phi \right] = 0 \tag{2-2}$$

where D_i and $c_i(\mathbf{r})$ are the diffusion coefficients and concentrations, respectively, of ion i, and Z_i is the charge carried by the ion. The Nernst-Planck equation was solved using SOR after being cast into a more convenient form with a Slotboom transformation(SLOTBOOM; de Graaff, 1976). To mimic our experimental system which uses a KCl electrolyte solution, we used $D_{K^+} = 1.96 \times 10^5$ $cm^2 s^{-1}$ and $D_{Cl^-} = 2.03 \times 10^5$ $cm^2 s^{-1}$, and the equilibrium concentrations of both ions were set to 0.1 mol/L. The concentrations calculated from the Nernst-Planck equation were used to construct refined values of $\rho_m(\mathbf{r})$, which were used to refine the electrostatic potential.

Finally, the ionic current for both species was calculated from their flux $\mathbf{j}_i(\mathbf{r})$, where

$$\mathbf{j}_i(\mathbf{r}) = -D_i \left[\nabla c_i(\mathbf{r}) + \frac{Z_i c_i(\mathbf{r})}{k_B T} \nabla \phi(\mathbf{r}) \right] \tag{2-3}$$

and the current in the z-direction, through the nanopore is calculated as

$$i(z) = \frac{2F}{L_z} \int_{\frac{L_z}{2} - \frac{L_p}{2}}^{\frac{L_z}{2}} \int_0^{L_x} \int_0^{L_y} [\mathbf{j}_{K^+}(\mathbf{r}) + \mathbf{j}_{Cl^-}(\mathbf{r})] \cdot \hat{\mathbf{z}} \; dx dy dz \tag{2-4}$$

where F is Faraday's constant. We arbitrarily chose to calculate the current as the mean in the bottom half of the pore to mitigate oscillations due the entrance of the particle in the pore.

2.2
Machine Learning

Even with the enhancements in computational performance achieved by using GPUs, PNP calculations take several minutes to converge, effectively making them incompatible with Monte Carlo simulations that would require a PNP calculation for each trial move. To address this challenge, one approach was to use a neural network to model the results from a representative training set of PNP calculations. A multilayer percepton (MLP) neural network was used, due its simplicity of implementation and due to the fact of being universal function approximators, although other neural networks could be implemented for the this task. Figure 2.1 show a representation of a generic MLP.

The MLP is composed MLP are feedforward networks, the first (input) layer uses the particle position as input and the the next each layer uses the
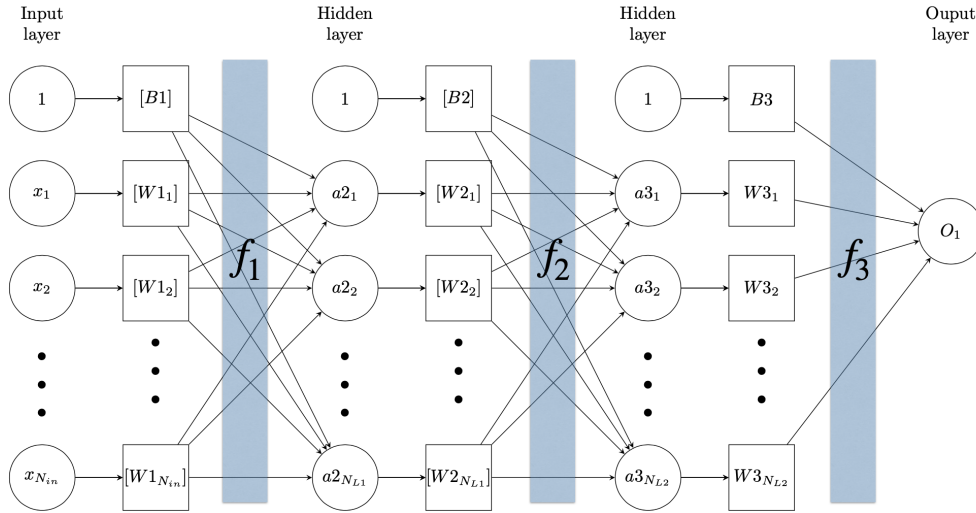
Figure 2.1: Generic structure of a Multilayer Percepton neural network.

previous layer as input, modified by the activation function. Rectified Linear Units (ReLU) were used as activation functions for all layers except the output layer which used a unit linear function. Therefore, the values in the neurons of each layer a_n were calculated as:

$$a_n = f_n W_n a_{n-1} \tag{2-5}$$

where f_n is the activation function for layer n, W_n is the neurons (matrix with weights and bias) for layer n, and a_{n-1} is the layer input.

The final neutral network architecture was composed of 5 hidden layers, with 50 units (neurons) in each layer. These layers were connected to an additional output layer containing a single unit that carries the value of the predicted electrostatic potential. The justification for this choice of this particular architecture is presented in a later chapter, but was the result of choosing the smallest number of layers and neutrons which can reliably reproduce the PNP results.

The MLP was trained in python using Tensorflow/keras, using the Adam optimizer algorithm, mean squared error as loss metric validation split of 0.1, number of epochs of 1000 and batch size of 256. Also, a variable learning rate was used, with initial value of 0.01 and 50% decay at each 100 epochs.

The weights and biases from training the network with the PNP results were recorded in a text file that was read by the Dynamic Monte Carlo simulation code.

2.3
Dynamic Monte Carlo (DMC)

Colloidal particles in suspension have stochastic trajectories due to the influence of thermal fluctuations. We used Metropolis Monte Carlo (MC) to mimic these fluctuations and simulate the trajectories of nanoparticles as they translocated through a nanopore.

For each Monte Carlo step, a random translation of a nanoparticle is attempted and either rejected or accepted. Using the Metropolis algorithm, the energy of old and new configurations are calculated and compared: if there is a decrease in energy, the trial is always accepted. Otherwise, if the energy increases the new configuration is accepted with a probability depending on the Boltzmann factor of the increase in energy. The probability is given by:

$$p(\Delta U) = \begin{cases} 1 & \Delta U \leq 0 \\ e^{-\beta \Delta U} & \Delta U > 0 \end{cases} \qquad (2\text{-}6)$$

If a trial move results in the overlap between the particle and the membrane, then $\Delta U = \infty$ and the move is rejected. To calculate the potential energy U, we used the product of the electrostatic potential and an effective charge to ensure the desired particle mobility.

2.3.0.1
DMC of Nanospheres

Due to the symmetry of spherical nanoparticles, the local field inhomogeneities were neglected and the potential was modeled as the product of the effective charge and the voltage at the position.

Although the use of Metropolis Monte Carlo to mimic Brownian motion is not new (KIKUCHI et al., 1991), Cuetos and Pati (PATTI; CUETOS, 2012; CUETOS; PATTI, 2015) recently developed an alternative DMC algorithm that directly links the Monte Carlo steps to a unique time-scale that depends on diffusion coefficient of the particles. The intrinsic MC time step is given by:

$$\delta t_{MC} = \frac{(\delta_{\mathbf{x}}^{max})^2}{2\,D} \qquad (2\text{-}7)$$

where D is the diffusion coefficient obtained from the Stokes-Einstein relation (Equation 1-2):

$$D = \frac{k_B T}{3\pi \eta d_{NP}}$$

A time step that is equivalent to a Brownian dynamics simulation is calculated from the intrinsic (MC) time step corrected by the acceptance rate:

$$\delta t = \frac{\overline{\mathcal{A}}}{3} * \delta t_{MC} \tag{2-8}$$

where $\overline{\mathcal{A}}$ is defined as:

$$\overline{\mathcal{A}} = \frac{\text{Accepted trials}}{\text{Total steps}} \tag{2-9}$$

The electrostatic potential was calculated by running the trained neural network implemented within the DMC code. For the simulations of the rod particles, a multilinear interpolation from the PNP results using the code of Lignell (2020). The current through the pore relative to each nanoparticle position was calculated by linear interpolation of the tabulated values calculated by PNP.

2.3.0.2
DMC of Nanorods

In each DMC cycle, a trial displacement δr is attempted with size

$$\delta r = \delta r_{\parallel} \mathbf{u}_{\parallel} + \delta r_{\perp,1} \mathbf{u}_{\perp,1} + \delta r_{\perp,2} \mathbf{u}_{\perp,2} \tag{2-10}$$

where $\mathbf{u}_{\parallel}$, $\mathbf{u}_{\perp,i}$ in axial and perpendicular directions of the rod and δr_i uniform random variables. The rod orientation $\mathbf{u}$ is also changed in each trial:

$$\mathbf{u}_{parallel,\text{new}} = \mathbf{u}_{\mathbf{parallel}} + \delta \mathbf{u} \tag{2-11}$$

$$\delta \mathbf{u} = \delta \vartheta_1 \, \mathbf{w_1} + \delta \vartheta_2 \, \mathbf{w_2} \tag{2-12}$$

where $\mathbf{w_1}$ and $\mathbf{w_2}$ are two randomly chosen vectors perpendicular to each other and to $\mathbf{u}$. The terms $\delta \vartheta_i \, \delta \vartheta_2$ are uniform random variables. The random variables are chosen respecting the following conditions:

$$|\delta r_{\parallel}| < \delta r_{\parallel,max} \tag{2-13}$$

$$|\delta r_{\perp,i}| < \delta r_{\perp,max} \tag{2-14}$$

$$|\delta \vartheta_i| < \delta \vartheta_{max} \tag{2-15}$$

$$\delta r_{\parallel,max} = \sqrt{2 D_{\parallel} \delta t_{MC}} \tag{2-16}$$

$$\delta r_{\perp,max} = \sqrt{2 D_{\perp} \delta t_{MC}} \tag{2-17}$$

$$\delta \vartheta_{max} = \sqrt{2 D_{\vartheta} \delta t_{MC}} \tag{2-18}$$

where the parallel ($D_{\parallel}$), perpendicular ($D_{\perp}$) and rotational (D_{ϑ}) diffusion coefficients are calculated by:

$$D_{\parallel} = \frac{k_B T}{2\pi\eta L_{rod}}(\log(p) + v_{\parallel}) \qquad (2\text{-}19)$$

$$D_{\perp} = \frac{k_B T}{4\pi\eta L_{rod}}(\log(p) + v_{\perp}) \qquad (2\text{-}20)$$

$$D_{\vartheta} = \frac{3k_B T}{\pi\eta L_{rod}^3}(\log(p) + v_{\vartheta}) \qquad (2\text{-}21)$$

End-point corrections v_i are defined depending on the aspect ratio p (L_{rod}/d_{rod}) of the rod (TIRADO; MARTÍNEZ; TORRE, 1984):

$$v_{\parallel} = -0.207 + 0.980/p - 0.133/p^2 \qquad (2\text{-}22)$$

$$v_{\perp} = 0.839 + 0.185/p + 0.233/p^2 \qquad (2\text{-}23)$$

$$v_{\vartheta} = -0.662 + 0.917/p - 0.050/p^2 \qquad (2\text{-}24)$$

The value of δt can be chosen directly or based on a mean translational step

$$\delta t = \delta x_{max}^2/2D \qquad (2\text{-}25)$$

$$D = \frac{k_B T}{3\pi\eta L_{rod}}(log(p) + v) \qquad (2\text{-}26)$$

with $v = (v_{\parallel} + v_{\perp})/2$. At this point, the time step can be calculated as the Equation 2-8.

For nanorods, as the voltage differences along the particle surface can cause an observable rotation in the particle, the potential was calculated as the result of the integration of the Taylor expanded voltage function:

$$U = q_{eff}\left\{V_o + \frac{L^2}{24}\frac{\partial^2 V}{\partial z_c^2} + \left[\frac{R^2}{4}\left(\frac{\partial^2 V}{\partial r_1^2} + \frac{\partial^2 V}{\partial r_2^2}\right)\right]\right\} \qquad (2\text{-}27)$$

The second-order derivatives were calculated by finite difference:

$$\frac{\partial^2 V}{\partial x_i^2} \approx \frac{V_{(0+dx_i)} - 2\,V_0 + V_{(0-dx_i)}}{dx_i^2} \qquad (2\text{-}28)$$

Each point in the finite-difference was obtained by linear interpolation from the tabulated values on xz-plane calculated by an open pore (no particle) calculation. The derivation of Equation 2-27 and analysis of the is shown in the section 6.1.
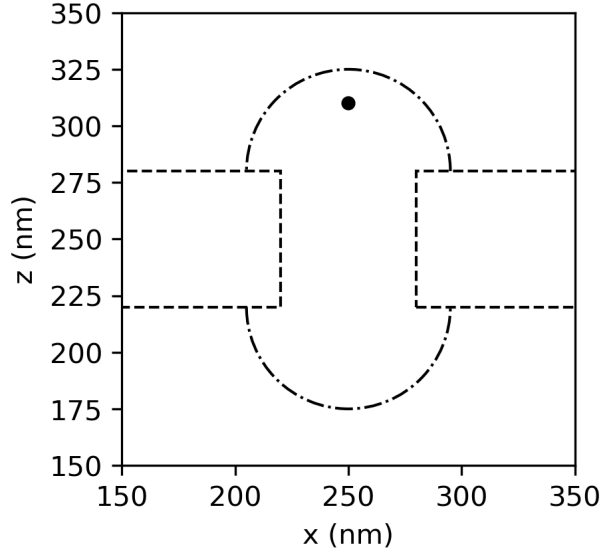
Figure 2.2: Schematic of the boundary conditions used in the DMC simulation. Dotted lines represent the membrane/pore location, whereas the dash-dotted lines indicate the boundaries where the trajectories are terminated. The black dot indicates the initial position of the particle.

2.3.0.3
Boundaries

To improve computational efficiency, when simulating translocation processes we implemented the boundary condition depicted in the Figure 2.2. The dash-dotted lines denote the boundary of an access region where most of the field is decayed to very low values and the relative blockade is negligible. The particle is initiated in the upper half of the (3D) box aligned with the main axis of the pore, at a distance $r_P \geq d_P/2$. When a particle reaches one of the two "caps", the event is terminated, the particle is re-initiated in the central axis and a new trajectory of a new event is recorded.

For translocation simulations of spherical particles, the pore diameter was fixed in $d_p = 60$ nm, and the pore length L_p, particle diameter d_{NP} and particle mobility μ were varied.

2.4
Experimental Translocation Measurements

Experimental translocation measurements were performed on cetyltrimethyl ammonium bromide (CTAB)-coated Au nanospheres (Nanopartz Inc., Loveland, CO), with average diameters of $d_{rod} = 30$ nm. The particles were dispersed in a 0.500 mol L^{-1} KCl electrolyte solution at a concentration of $\phi_{NP} = 9.2 \times 10^{10}$ NPs/mL. Low-noise SiO_2-supported SiN$_x$ membranes ($L_p = 100$ nm), containing a single $d_p = 80$ nm nanopore,

were purchased from Goeppert, Inc. (Philadelphia, PA). The membranes were cleaned in hot Piranha solution (3:1 mixture by volume of H_2SO_4 to 30% H_2O_2, $T = 80$ °C) for 10 minutes, rinsed with Milli-Q water, and stored in isopropyl alcohol prior to use.

Ionic current measurements were performed using an eNPR amplifier (Elements srl, Cesena, Italy) equipped with a 2nd generation Elements flow cell and Ag/AgCl electrodes. The ionic current through the nanopore was sampled at a frequency of 200 kHz, resulting in a final bandwidth of 20 kHz after applying a low-pass filter to remove high-frequency noise, limiting temporal resolution to approximately 50 μs. Ag/AgCl electrodes were fabricated by exposing Ag wire to a 7.4% sodium hypochlorite solution for 10 minutes. Prior to measuring nanoparticle translocations, proper wetting of the nanopore by the electrolyte was verified by measuring the resistance and capacitance of the membrane. Afterward, the nanoparticle solution was loaded into the *cis*-chamber of the flow cell, and electrolyte solution into the *trans*-chamber. A potential difference of 200 mV was applied across the chamber and the ionic current was monitored for approximately 10 minutes. Translocation events were extracted and analyzed with the Pypore software package (<https://github.com/parkin/pypore>).

3
Simple Analytical Models for Current Prediction in Nanopores

Simulations that accurately reflect the current response in nanopores are important tools for developing nanopore sensing, being the main goal of this research. However, simple approximate models that can provide estimates of nanopore behavior can be of great importance as well, allowing one to quickly check the correct operation of experimental results and the overall suitability of the simulations. In this section, analytical models for the maximum current response in cylindrical pores will be derived, revisiting the models already present in the literature and expanding to cases where studies in the literature are missing. Finally, some models will be contrasted with our experimental results, leading directions for the development of a more complex simulation tool.

As stated in Chapter 1, the current in response to an applied electrostatic potential can be in a first approximation be estimated by Ohm's law, modeling the system as a circuit with one single resistor (Equation 1-18):

$$i = \frac{V}{R} = GV$$

where i is the ionic current the current, V the voltage, R the pore resistance and its reciprocal, G the pore conductance. As depicted in Figure 3.1, a better estimate would be to treat the pore resistance as the sum of infinitesimal resistors in series over the pore length L_P:

$$R = \int_{L_P} R(z)dz \tag{3-1}$$

Under such an approximation, the "layer" resistance $R(z)$ can be computed by the inverse of the local fluid conductivity γ integrated over the cross-sectional area $A(z)$:

$$R(z) = \frac{1}{\int_{A(z)} \gamma} \tag{3-2}$$

with

$$\gamma = \sum \mu_i n_i z_i e \tag{3-3}$$

In the above equations, e is the elementary charge, μ_i the mobility of ion species i, n_i the concentration (number per volume) of species i, and z_i
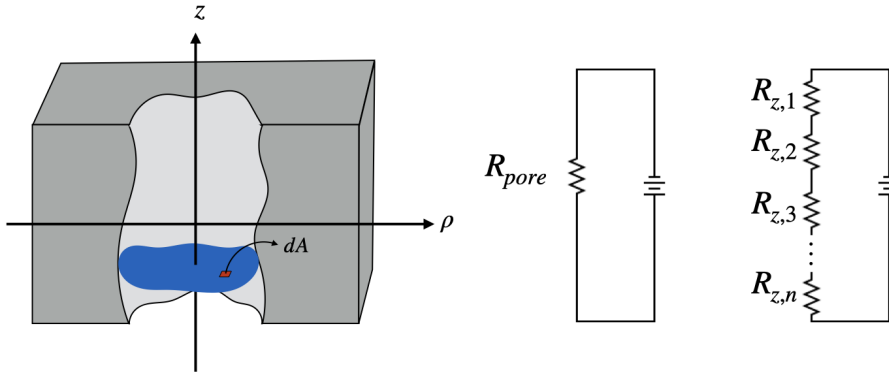
Figure 3.1: Representation of a generic pore, with an infinitesimal area of a cross-section highlighted. On the right, are the simplified equivalent circuits.

the valency of ion i. Using cylindrical coordinates (ρ, ϕ, z), the pore resistance becomes:

$$R = \int_{L_P} \frac{1}{\int_{A(z)} \gamma(\rho, \phi, z) \, d\rho d\phi} dz \tag{3-4}$$

For pores and particles of geometries with axial symmetry such as cylinders and spheres, the integration in ϕ can be replaced by a change in variables:

$$R = \int_0^{L_P} \frac{1}{2\pi \int_\rho \gamma(\rho, z) \, \rho \, d\rho} dz \tag{3-5}$$

For a cylindrical pore with diameter d_P and radius $r_P = d_P/2$ and the particle in the center of the pore, it is possible to choose the origin appropriately and consider plane symmetry, and perform the integration in only half of the length.

$$
\begin{aligned}
R &= 2\int_0^{L_P/2} \frac{1}{2\pi \int_\rho \gamma(\rho, z) \, \rho \, d\rho} dz \\
&= \frac{1}{\pi} \int_0^{L_P/2} \frac{1}{\int_\rho \gamma(\rho, z) \, \rho \, d\rho} dz
\end{aligned}
\tag{3-6}
$$

Next, this approach will be used to build analytical models for pores without particles ("open pores") and with cylindrical ("rods") and spherical particles, both with uncharged and charged surfaces. In the case of fixed charges on the surface of the pore, the electric double layer is formed. Compared to the bulk concentration n_o, the local concentration n_i is varies according to an exponential form:

$$n_i \sim n_o \exp\left\{a \exp\left[-\kappa(r_P - \rho)\right]\right\} \tag{3-7}$$
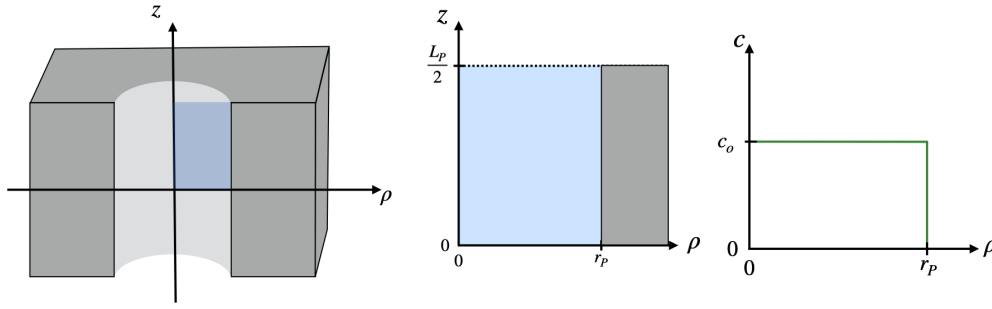
Figure 3.2: Representation of a cylindrical pore cut in ρz-plane. Colormap (middle) and plot (right) show constant concentration of ions in the whole volume of the pore.

where κ is the inverse of the Debye length and a a prefactor that depends on the surface geometry, charge, and solution.

To solve the nanopore resistance analytically, simplifications of these concentrations profiles will be made based on the assumption of electroneutrality. To test our derivations, a simplified numeric scheme was devised with the use of numeric integration following the Equation 3-8.

$$R \approx \sum_{i=0}^{n_z} \left(\frac{i}{n_z} \frac{L_P}{2\pi} \right) \frac{1}{\sum_{j=0}^{n_\rho} \left(\frac{j}{n_\rho} r_p \right) \gamma(\rho, z) \, \rho} \tag{3-8}$$

After some convergence tests, the number of points in both directions (n_z and n_ρ) were set to 300. Differently from the analytical models were the domain of integration, the numerical procedure summed the conductivity along all the pore lengths and radius, being the conductivity taken as zero when inside occluded areas. Also, for the numeric procedure, the expressions for the concentration in the form of the Equation 3-8 for the charged surfaces were used directly.

3.1
Uncharged, Open Pore

For an open pore without the effect of surface charges, the fluid conductivity can be taken as a constant across the pore volume, as is shown in Figure 3.2.

For KCl electrolyte solution:

$$\gamma(\rho, \phi, z) = \gamma_o = (\mu_K + \mu_{CL}) n_{KCl} e \tag{3-9}$$
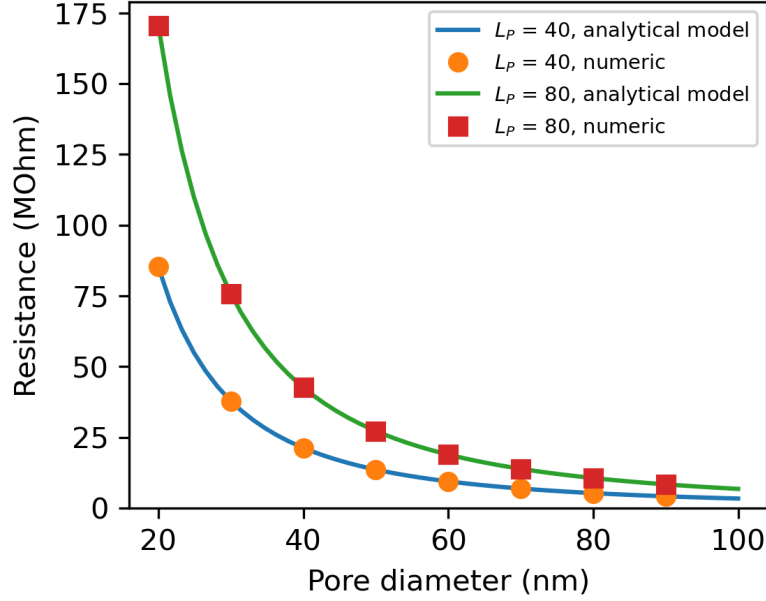
Figure 3.3: Open pore resistance of two pores with distinct length, both with $d_P = 100\,nm$ and $[KCl] = 0.100\,mol/L$.

From the expression of γ_o, the total resistance R_o of a uncharged open pore can be computed as:

$$
\begin{aligned}
R_o &= \frac{1}{\pi} \int_0^{L_P/2} \frac{1}{\int_0^{r_P} \gamma_o\, \rho\, d\rho}\, dz \\
&= \frac{L_P}{2\pi\gamma_o} \frac{1}{(1/2)[r_P^2 - 0]} \\
&= \frac{L_P}{\pi} \frac{1}{r_P^2} \frac{1}{\gamma_o} \\
&= \frac{4\,L_P}{\pi} \frac{1}{d_P^2} \frac{1}{(\mu_K + \mu_{CL})n_{KCl}e}
\end{aligned}
\tag{3-10}
$$

Figure 3.3 shows Equation 3-10 and the results of the simple numeric scheme, with excellent quantitative agreement between them. As expected, pores that are longer and with smaller aperture result in higher resistances, therefore in lower current for some specific applied voltage.

3.2
Uncharged Pore with an Uncharged Nanorod

Figure 3.4 shows an uncharged nanorod of length $L_{rod} < L_P$ and diameter d_{rod} and radius $r_{rod} = d_{rod}/2$ inside a cylindrical pore.

The pore resistance in the presence of the nanorod can be calculated by the sum of the resistances from the length not occluded by the rod and the occluded part:
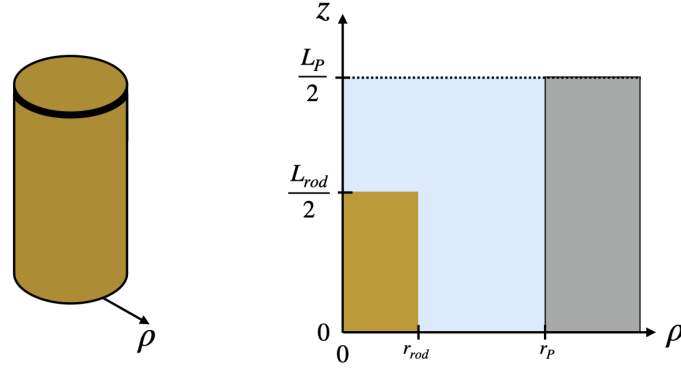
Figure 3.4: Representation of a cylindrical pore partially occluded by a rod particle.

$$R_{rod} = \frac{1}{\pi} \int_0^{(L_P - L_{rod})/2} \frac{1}{\int_0^{r_P} \gamma_o \, \rho \, d\rho} dz + \frac{1}{\pi} \int_0^{L_{rod}/2} \frac{1}{\int_{r_{rod}}^{r_P} \gamma_o \, \rho \, d\rho} dz$$

$$= \frac{(L_P - L_{rod})}{\pi \gamma_o} \frac{1}{r_P^2} + \frac{L_{rod}}{\pi \gamma_o} \frac{1}{(r_P^2 - r_{rod}^2)}$$

$$R_{rod} = \frac{4\,L_P}{\pi} \left[\left(1 - \frac{L_{rod}}{L_P} \right) \frac{1}{d_p^2} + L_{rod} \frac{1}{(d_P^2 - d_{rod}^2)} \right] \frac{1}{(\mu_K + \mu_{CL}) n_{KCl} e} \tag{3-11}$$

For the case of a nanorod long enough to occlude all the length of the pore, Equation 3-11 reduces to the equation presented by Smeets et al. (2006):

$$R_{rod} = \frac{4\,L_P}{\pi} \frac{1}{(d_P^2 - d_{rod}^2)} \frac{1}{(\mu_K + \mu_{Cl}) n_{KCl} e} \tag{3-12}$$

Figure 3.5 shows the pore resistance in the presence of a rod of length equals to ($L_R/L_P = 1$) and half of ($L_R/L_P = 0.5$) the pore length. To the length of the pore, a longer rod occludes a bigger part of the volume, therefore, resulting in higher resistance. The values of resistance correctly converge to the open pore resistance as the diameter of the particle approaches zero and diverge to infinity when approaching the diameter of the pore.

3.3
Uncharged Pore with an Uncharged Nanosphere

In all the examples shown earlier, the domain of integration in ρ remained constant over the integration along the length of the pore (or pore section). With a sphere inside the pore, the area occupied by the particle in each cross-
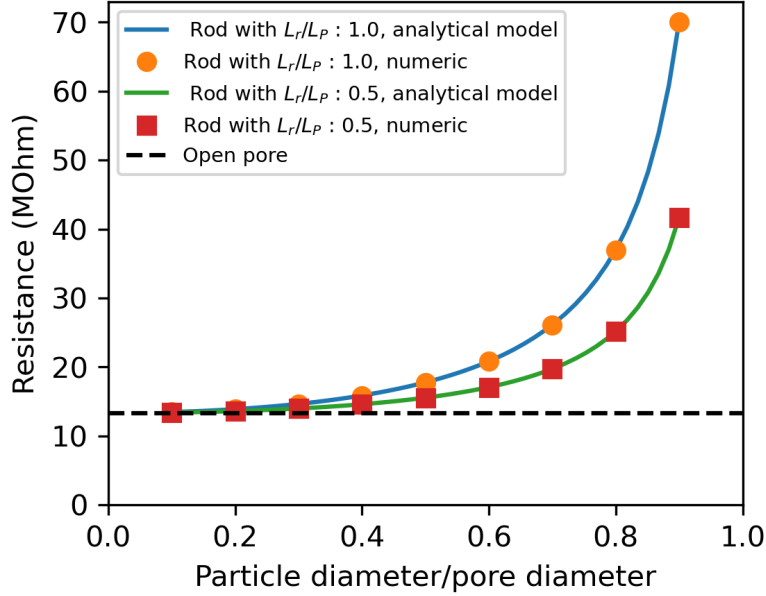
Figure 3.5: Pore resistance in the presence of a rod same length $(L_R/L_P = 1)$ and half $(L_R/L_P = 0.5)$ of the length of the pore. $d_P = 100\,nm$ and $[KCl] = 0.100\,mol/L$.

section changes with the height, as is shown in Figure 3.6.

Considering a spherical particle with diameter $d_{NP} < L_P$,

$$R_{sphere} = R_{unoccluded} + R_{occluded} \tag{3-13}$$

$$
\begin{aligned}
R_{unoccluded} &= \frac{1}{\pi} \int_0^{(L_P/2)-r_{NP}} \frac{1}{\int_0^{r_P} \gamma_o\,\rho\,d\rho} dz \\
&= \frac{L_P - 2r_{NP}}{\pi\,\gamma_o} \frac{1}{r_P^2} \\
&= \frac{4L_P}{\pi} \frac{1}{d_P^2}\left(1 - \frac{d_{NP}}{L_P}\right)\frac{1}{\gamma_o}
\end{aligned}
\tag{3-14}
$$

$$
\begin{aligned}
R_{occluded} &= \frac{1}{\pi} \int_0^{r_{NP}} \frac{1}{\int_{\sqrt{r_{NP}^2-z^2}}^{r_P} \gamma_o\,\rho\,d\rho} dz \\
&= \frac{1}{\pi} \int_0^{r_{NP}} \frac{1}{(1/2)[r_P^2 - (r_{NP}^2 - z^2)]} dz \\
&= \frac{1}{\pi} \int_0^{r_{NP}} \frac{1}{r_P^2 - r_{NP}^2 + z^2} dz
\end{aligned}
\tag{3-15}
$$
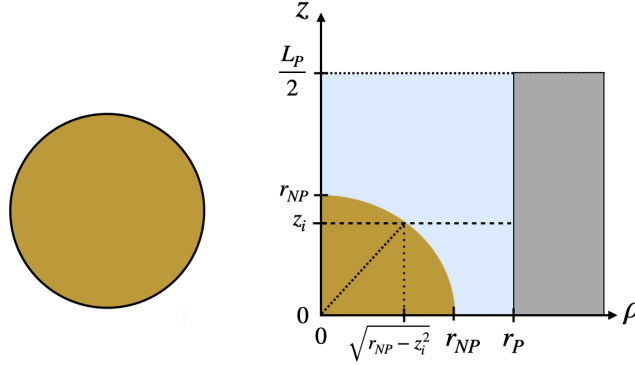
Figure 3.6: Representation in the ρz-plane of a cylindrical pore partially occluded by a spherical particle. The lines show the geometries of consideration in calculating the radial position of the particle surface in a generic height z_i.

$$
\begin{aligned}
R_{occluded} &= \frac{2}{\pi} \frac{1}{\gamma_o} \int_0^b \frac{1}{p+z^2} dz, \quad p = (r_P^2 - r_{NP}^2) \\
&= \frac{2}{\pi} \left(\frac{1}{\sqrt{p}} \arctan \frac{b}{\sqrt{p}} \right) \frac{1}{\gamma_o} \\
&= \frac{2}{\pi} \left(\frac{1}{\sqrt{r_P^2 - r_{NP}^2}} \arctan \frac{r_{NP}}{\sqrt{r_P^2 - r_{NP}^2}} \right) \frac{1}{\gamma_o} \\
&= \frac{4L_P}{\pi} \frac{1}{L_P} \left(\frac{1}{\sqrt{d_P^2 - d_{NP}^2}} \arctan \frac{d_{NP}}{\sqrt{d_P^2 - d_{NP}^2}} \right) \frac{1}{\gamma_o}
\end{aligned}
\tag{3-16}
$$

$$
R_{sphere} = \frac{4L_P}{\pi} \left[\frac{1}{d_P^2} \left(1 - \frac{d_{NP}}{L_P} \right) + \frac{1}{L_P} \left(\frac{1}{\sqrt{d_P^2 - d_{NP}^2}} \arctan \frac{d_{NP}}{\sqrt{d_P^2 - d_{NP}^2}} \right) \right] \frac{1}{\gamma_o}
\tag{3-17}
$$

Bacri et al. (2011) with a different approach used cartesian coordinates and an expression for the free area of the cross-section $A(z)$ as

$$
A(z) = \frac{\pi}{4} (d_P^2 - d_{NP}^2) \left[1 + \frac{4z^2}{d_P^2 - d_{NP}^2} \right]
\tag{3-18}
$$

$$
R_{sphere} = \int_{-L_P/2}^{L_P/2} \frac{1}{\gamma A(z)} dz
\tag{3-19}
$$
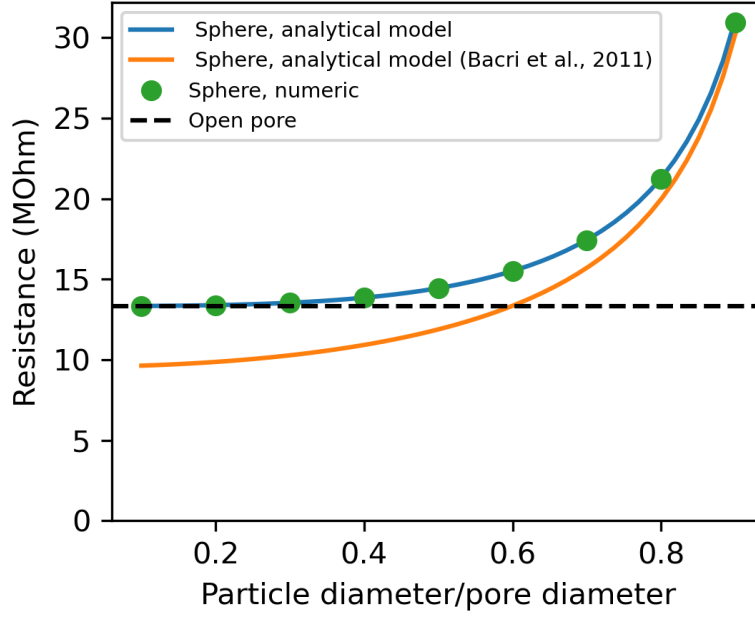
Figure 3.7: Pore resistance in the presence of a sphere, confronted to the model from Bacri et al. (2011). $d_P = 100\,nm$ and $[KCl] = 0.100\,mol/L$.

$$R_{sphere} = \frac{4}{\pi} \frac{1}{(d_P^2 - d_{NP}^2)} \frac{1}{\gamma_o} \int_{-L_P/2}^{L_P/2} \frac{dz}{1 + \frac{4z^2}{(d_P^2 - d_{NP}^2)}} \qquad (3\text{-}20)$$

$$R_{sphere} = \frac{4}{\pi} \frac{1}{d_{NP}^2} \frac{1}{\sqrt{1 - \left(\frac{d_{NP}}{d_P}\right)^2}} \arctan\left[\frac{L_P}{d_P} \frac{1}{\sqrt{1 - \left(\frac{d_{NP}}{d_P}\right)^2}}\right] \frac{1}{\gamma_o} \qquad (3\text{-}21)$$

Figure 3.7 shows the pore resistance in the presence of a sphere, calculated with the equation due to the model from Bacri et al. (2011) using $d_P = 100\,nm$ and $[KCl] = 0.100\,mol/L$. The new model derived here shows better agreement with the numeric scheme and correctly converges to open pore resistance for particles with vanishing size.

3.4
Charged, Open Pore

The equation 3-22 to describe the exceeding ion concentration near the surface(MUTHUKUMAR, 2011):

$$\psi_o = \frac{2k_bT}{e}\text{arcsinh}\sigma_P(8\epsilon\epsilon_o k_b T n_o)^{-1/2}$$

$$(3\text{-}22)$$

$$\delta n_i(\rho) = \exp\left[\frac{ze}{k_bT}\psi_o\frac{I_o(\kappa\,\rho)}{I_o(\kappa\,r_P)}\right]$$

where $I_n(x)$ is the nth-order modified Bessel function of the first kind. Even with a slight depletion of the co-ions near the surface, to bring electroneutrality there is an exceeding enrichment of the concentration of the counterions, resulting in a net increase of the total local concentration close to the surface. Therefore, the pore resistance is decreased with the surface charge density σ_P.

As depicted in Figure 3.8, one approach to simplifying the calculations is to replace the exponential local concentration with an evenly distributed concentration along a portion with a size equal to m times the Debye length κ^{-1} (equation 3-23).

$$r_{PEDL} = r_P - m\kappa^{-1} \tag{3-23}$$

To ensure electroneutrality, all the exceeding charge on the surface is computed to be balanced only by the exceeding counter-ion concentration $\delta n_{k,EDLP}$, where k represents the counter-ion depending on the sign of the surface charge.

$$\delta n_{k,EDLP} = \frac{(\sigma_P A_{LP})/e}{V_{PEDL}} = \frac{\sigma_P \pi d_P L_P/e}{\pi (r_P^2 - r_{PEDL}^2) L_P} = \frac{\sigma_P d_P}{e(r_P^2 - r_{PEDL}^2)} \tag{3-24}$$

Since the conductivity of the infinitesimal layer is calculated from the integration of a linear term on the local concentration (Equation 3-4), the profile does not affect the final result as long as the total charge remains unchanged.

The local conductivity in the region near the pore is then:

$$\gamma_{PEDL} = \sum \mu_i n_i z_i e = \gamma_o + \mu_i \frac{\sigma_P d_P}{e(r_{PEDL}^2 - r_{rod}^2)} \tag{3-25}$$

$$
\begin{aligned}
R_{o,EDL} &= \frac{1}{\pi} \int_0^{(L_P)/2} \frac{1}{\int_0^{r_{PEDL}} \gamma_o \, \rho \, d\rho + \int_{r_{PEDL}}^{r_P} \gamma_{PEDL} \, \rho \, d\rho} dz \\
&= \frac{L_P}{2\pi} \left(\frac{1}{\gamma_o(1/2)(r_{PEDL}^2) + \gamma_{PEDL}(1/2)(r_P^2 - r_{PEDL}^2)} \right) \\
&= \frac{L_P}{\pi} \left(\frac{1}{\gamma_o(r_{PEDL}^2) + \gamma_{PEDL}(r_P^2 - r_{PEDL}^2)} \right) \\
&= \frac{4L_P}{\pi} \left(\frac{1}{\frac{\gamma_{PEDL}}{\gamma_o}(d_P^2 - d_{PEDL}^2) + d_{PEDL}^2} \right) \frac{1}{\gamma_o}
\end{aligned}
\tag{3-26}
$$

Setting d_{PEDL} to zero means the dispersion of the exceeding ionic concentration throughout the pore volume (Figure 3.9). As the profile is constant in the length, this approach leads to an equivalent but simpler form
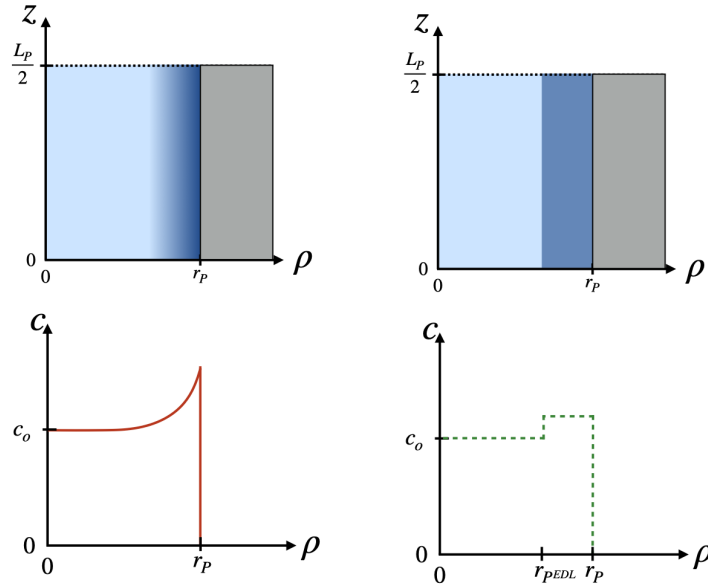
Figure 3.8: Representation of a charged cylindrical pore. Colormap in ρz-plane (up) and plot (down) show the concentration of ions along the radial direction: On the left, it shows the concentration of counterions increasing exponentially as closer to the pore surface; in the right, the simplified concentration profile used in the analytical model.

of Equation 3-26 by the Equation 3-27.

$$R_{o,EDL} = \frac{4\,L_P}{\pi}\left(\frac{1}{d_P^2\,(\mu_K + \mu_{CL})n_{KCl}e + d_P\mu_i\,4\,\sigma_P}\right) \qquad (3\text{-}27)$$

Figure 3.10 shows the open pore resistance of charged pores with two distinct lengths. The presence of charges results in lower resistance compared to the uncharged pores with the same geometries (Figure 3.3).

3.5
Charged Pore with a Charged Nanorod

When a charged particle is inside the pore, the actual electrical field between the surfaces needs to be self-consistently solved, for example using the PNP formalism. Here, as a tentative approximation, the ion concentration around the pore and particle surfaces were computed as separate systems and forcibly added to each other. As a further approximation, the charge from cylinder caps and other end-effects were not taken into account.

The equation 3-28 to describe the exceeding ion concentration near the rod surface(MUTHUKUMAR, 2011):
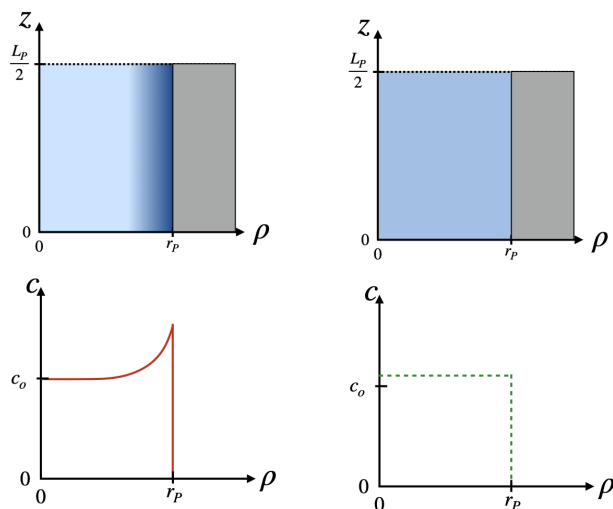
Figure 3.9: Representation of a charged cylindrical pore. Colormap in ρz-plane (up) and plot (down) show the concentration of ions along the radial direction: On the left, it shows the concentration of counterions increasing exponentially as closer to the pore surface; on the right, the concentration profile assuming the dispersing of the exceeding charge throughout the pore volume.
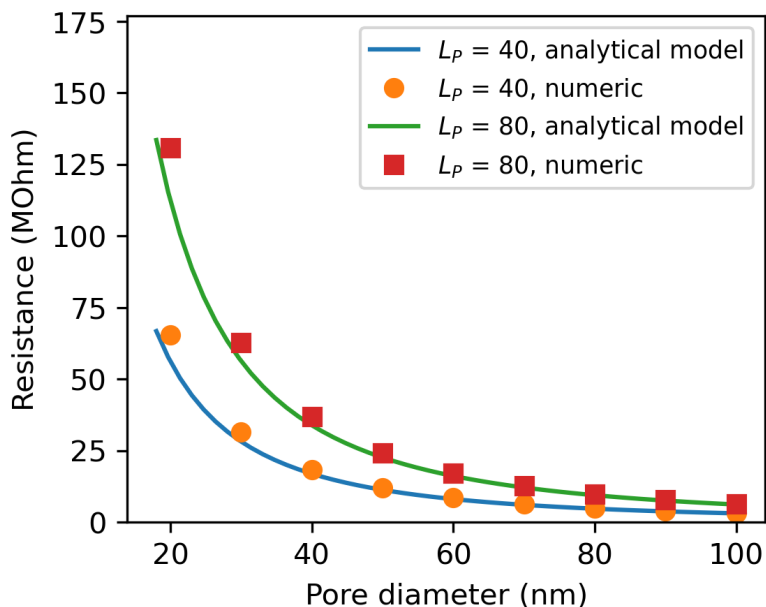
Figure 3.10: Open pore resistance of pores with two distinct length, both with $d_P = 100\,nm$, $[KCl] = 0.100\,mol/L$ and $\sigma_P = 50\,mC/m^2$.

Figure 3.11: Counterion concentration near a charged rod along the radial direction following the exponential decay (solid line) and the simplified profile (dashed line). On the right, the colormap in ρz-plane represents the simplified concentration for both a charged cylindrical pore and charged rod particle.

$$\ell = \frac{e z_P}{2\pi\sigma_P r_{rod}}$$

$$\Gamma = e^2/(4\pi\epsilon\epsilon_o k_b T \ell) \tag{3-28}$$

$$\delta n_i(\rho) = \exp\left[\frac{ze}{k_b T}\frac{2 z_p z_c \Gamma}{\kappa\, r_{rod}}\frac{K_o(\kappa\,\rho)}{K_1(\kappa\,r_{rod})}\right]$$

where $K_n(x)$ is the modified Bessel function of nth order.

Here we can take the same approach of considering only a finite region near the charged particle with stepwise concentration profile.

$$r_{rod^{EDL}} = r_{rod} + m\kappa^{-1} \tag{3-29}$$

Even the real concentration profile will no follow the simple superposition of the profiles from a free particle and an open pore, the excess concentration decays vary strongly within a distance of few Debye length. In a typical salt concentration of 100 mol/L, the Debye length is in order of one nanometer. Hence, considering two Debye length as a cut-off distance, if a particle has a radius 4 nanometer smaller than the pore, it is not expected to see a significant overlap of the double layer and the stepwise profile should be a fair approximation.

Therefore, we obtain:

$$\delta n_{i,EDL^{rod}} = \frac{(\sigma_{rod} A_{L^{rod}})/e}{V_{EDL^{rod}}} = \frac{\sigma_{rod} \pi \, d_{rod} \, L_{rod}/e}{\pi(r_{rod EDL}^2 - r_{rod}^2)L_{rod}} = \frac{\sigma_{rod} \, d_{rod}}{e(r_{rod EDL}^2 - r_{rod}^2)}$$

$$(3\text{-}30)$$

$$\gamma_{rod^{EDL}} = \sum \mu_i \, n_{i,EDL^{rod}} \, z_i e = \gamma_o + \mu_i \frac{\sigma_{rod} \, d_{rod}}{e(r_{rod EDL}^2 - r_{rod}^2)} \qquad (3\text{-}31)$$

$$R_{rod,EDL} = R_{unaffected} + R_{affected} \qquad (3\text{-}32)$$

$$
\begin{aligned}
R_{unaffected} &= \frac{1}{\pi} \int_0^{(L_P - L_{rod})/2} \frac{1}{\int_0^{r_{PEDL}} \gamma_o \, \rho \, d\rho + \int_{r_{PEDL}}^{r_P} \gamma_{PEDL} \, \rho \, d\rho} dz \\
&= \frac{L_P - L_{rod}}{2\pi} \left(\frac{1}{\gamma_o(1/2)(r_{PEDL}^2) + \gamma_{PEDL}(1/2)(r_P^2 - r_{PEDL}^2)} \right) \\
&= \frac{L_P - L_{rod}}{\pi} \left(\frac{1}{\gamma_o(r_{PEDL}^2) + \gamma_{PEDL}(r_P^2 - r_{PEDL}^2)} \right) \\
&= \frac{4L_P}{\pi} \left(1 - \frac{L_{rod}}{L_P} \right) \left(\frac{1}{\frac{\gamma_{PEDL}}{\gamma_o}(d_P^2 - d_{PEDL}^2) + r_{PEDL}^2} \right) \frac{1}{\gamma_o}
\end{aligned}
$$

$$(3\text{-}33)$$

$$
\begin{aligned}
R_{affected} &= \frac{1}{\pi} \int_0^{L_{rod}/2} \frac{1}{\int_{r_{rod}}^{r_{EDL,rod}} \gamma_{rod^{EDL}} \, \rho \, d\rho + \int_{r_{EDL,rod}}^{r_{PEDL}} \gamma_o \, \rho \, d\rho + \int_{r_{PEDL}}^{r_P} \gamma_{PEDL} \, \rho \, d\rho} dz \\
&= \frac{L_{rod}}{2\pi} \left(\frac{1}{\frac{\gamma_{rod^{EDL}}}{2}(r_{EDL,rod}^2 - r_{rod}^2) + \frac{\gamma_o}{2}(r_{EDL,rod}^2 - r_{PEDL}^2) + \frac{\gamma_{PEDL}}{2}(r_P^2 - r_{PEDL}^2)} \right) \\
&= \frac{L_{rod}}{\pi} \left(\frac{1}{\gamma_{rod^{EDL}}(r_{EDL,rod}^2 - r_{rod}^2) + \gamma_o(r_{EDL,rod}^2 - r_{PEDL}^2) + \gamma_{PEDL}(r_P^2 - r_{PEDL}^2)} \right) \\
&= \frac{4L_P}{\pi} \left(\frac{L_{rod}}{L_P} \right) \left(\frac{1}{\frac{\gamma_{PEDL}}{\gamma_o}(d_P^2 - d_{PEDL}^2) + r_{PEDL}^2 - r_{rod}^2} \right) \frac{1}{\gamma_o}
\end{aligned}
$$

$$(3\text{-}34)$$

As before, due to the uniform cross section in the occluded and in the unoccluded regions, the charges can be evenly distributed to all the unoccluded volume in each region, leading to an alternative expression for the sum of Equations 3-34 and 3-33:
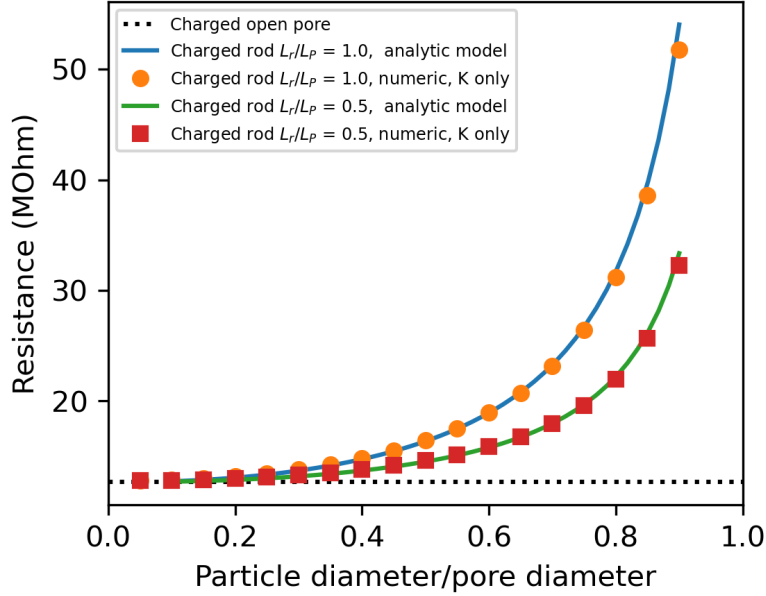
Figure 3.12: Pore resistance in the presence of a rod with the same length $(L_R/L_P = 1)$ and half $(L_R/L_P = 0.5)$ of the length of the pore. $d_P = 100\,nm$, $[KCl] = 0.100\,mol/L$ and $\sigma = 20mC/m^2$.

$$
\begin{aligned}
R_{rod,EDL} = {} & \frac{4L_P}{\pi}\left(1 - \frac{L_{rod}}{L_P}\right)\frac{1}{d_P^2}\left[\frac{1}{(\mu_K + \mu_{CL})n_{KCl}e + \mu_i\,4\,\sigma_P/d_P}\right] \\
& + \frac{4L_P}{\pi}\left(\frac{L_{rod}}{L_P}\right)\frac{1}{(d_P^2 - d_{rod}^2)}\left[\frac{1}{(\mu_K + \mu_{CL})n_{KCl}e + \mu_i\,4\,\sigma_P\frac{1}{d_P} + 4\sigma_{rod}\mu_i\frac{d_{rod}}{d_P^2 - d_{rod}^2}}\right]
\end{aligned}
\tag{3-35}
$$

if $L_{rod} = L_P$:

$$
R_{rod,EDL} = \frac{4L_P}{\pi}\frac{1}{(d_P^2 - d_{rod}^2)}\left[\frac{1}{(\mu_K + \mu_{CL})n_{KCl}e + \mu_i\,4\,\sigma_P\frac{1}{d_P} + 4\sigma_{rod}\mu_i\frac{d_{rod}}{d_P^2 - d_{rod}^2}}\right]
\tag{3-36}
$$

The pore resistance in the presence of a rod same length $(L_R/L_P = 1)$ and half $(L_R/L_P = 0.5)$ of the length of the pore are plotted in Figure 3.5. The curves follow the same trend as the uncharged case under similar conditions (Figure 3.5), but with lower resistances due to the enhanced ion concentration.

In lower salt concentrations, the size of the double layer is increased. If the increased concentration of ions can overcome the resistivity caused by the volume blocked by the particle, current enhancement can occur(GOYAL; FREEDMAN; KIM, 2013; VENTA et al., 2014b). This phenomenon, therefore, is more prevalent at lower salt concentration, where the size of the double layer is larger.
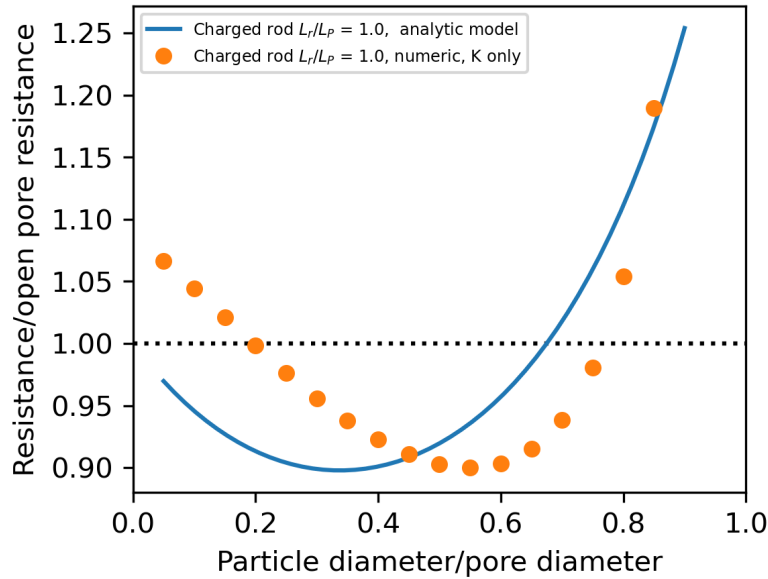
Figure 3.13: Relative resistance (to open pore) caused by a rod with the same length ($L_R/L_P = 1$) of the pore in a low salt concentration of $[KCl] = 0.010\,mol/L$. $L_P = 40\,nm$, $d_P = 20\,nm$, and $\sigma_P = \sigma_{rod} = 20mC/m^2$.

Figure 3.13 shows the relative resistance in relation to the open pore configuration caused by a rod same length of the pore, in a salt concentration of $0.010mol/L$. Relative resistances greater than one indicate predicted resistive pulses, whereas values lower than one show predicted conductive pulses due to the presence of the rod. The geometry of the pore and nanorod in this case is close to the used by Venta et al. (2014b), analyzing gold nanorods 10 nm in diameter translocating through silicon nitride pores with diameter range from 19 to 27 nm.

Venta et al. (2014b) related have found conductive spikes in the current for KCl concentrations up to 100 mM. Figure 3.14 shows the model prediction of a 10 nm diameter rod in a range of salt concentration, for three pore diameters. Contrary to the experimental results, only resistive pulses are predicted for concentration greater than $\sim 20\ mM$. Also, at the limited range where it is simultaneously predicted resistive pulses for the bigger pore and conductive for the small one, the relative are around 1%. Venta et al. (2014b), however, reported a crossover in relative resistance from $\sim +10\%$ (resistive) in a pore with diameter of 21 nm to $\sim -5\%$ (conductive) in a pore with diameter of 19 nm.
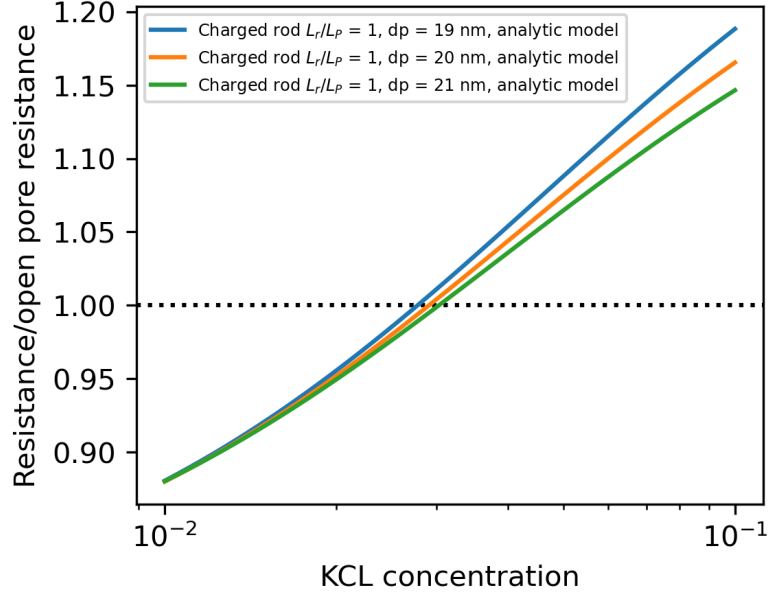
Figure 3.14: Relative resistance (to open pore) caused by a rod with the same length $(L_{rod}/L_P = 1)$ and half of the diameter of the pore $(d_{rod}/d_P = 0.5)$, for three values of pore diameters. $[KCl] = 0.010\,mol/L$, $L_P = 40\,nm$, and $\sigma_P = \sigma_{rod} = 20mC/m^2$.

3.6
Charged Pore with a Charged Nanosphere

In the case of a charged spherical particle, spherical coordinates $(\mathcal{R}, \phi, \theta)$ can be used in the equation 3-38 to describe the exceeding ion concentration near the surface(MUTHUKUMAR, 2011):

$$\mathcal{R} = \sqrt{\rho^2 + z^2} \tag{3-37}$$

$$\delta n_i(\mathcal{R}, \phi, \theta) = \delta n_i(\mathcal{R}) = \exp\left\{ \frac{\sigma_{NP}\pi d_{NP}^2}{4\pi\epsilon\epsilon_o} \frac{1}{r(1 + \kappa r_{NP})} \exp\left[-\kappa\left(\mathcal{R} - r_{NP}\right)\right] \right\} \tag{3-38}$$

Similar to the previous cases, a simplifying approach is to consider all the charges being neutralized evenly in a distance of m times the Debye length, as shown in Figure 3.15 and equations 3-39 and 3-38.

$$r_{NPEDL} = r_{NP} + m\kappa^{-1} \tag{3-39}$$

$$\delta n_{i,NPEDL} = \frac{(\sigma_{NP}A_{NP})/e}{V_{NPEDL} - V_{NP}} = \frac{(\sigma_{NP}\pi d_{NP}^2)/e}{\frac{4}{3}\pi(r_{NPEDL}^3 - r_{NP}^3)} = \frac{3\sigma_{NP}d_{NP}^2}{e4(r_{NPEDL}^3 - r_{NP}^3)} \tag{3-40}$$
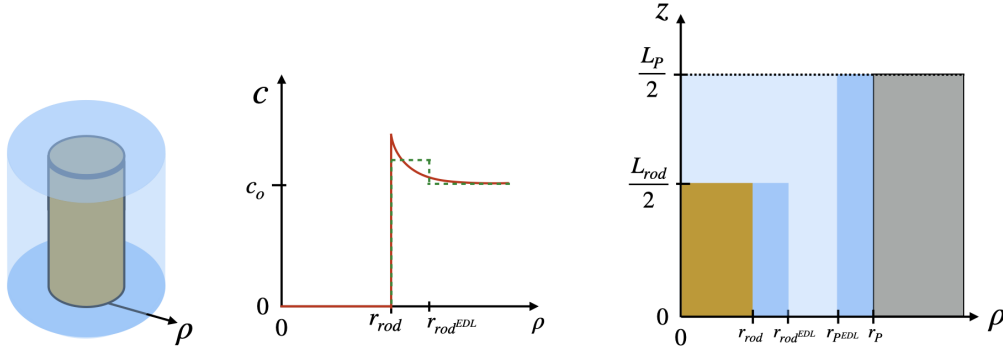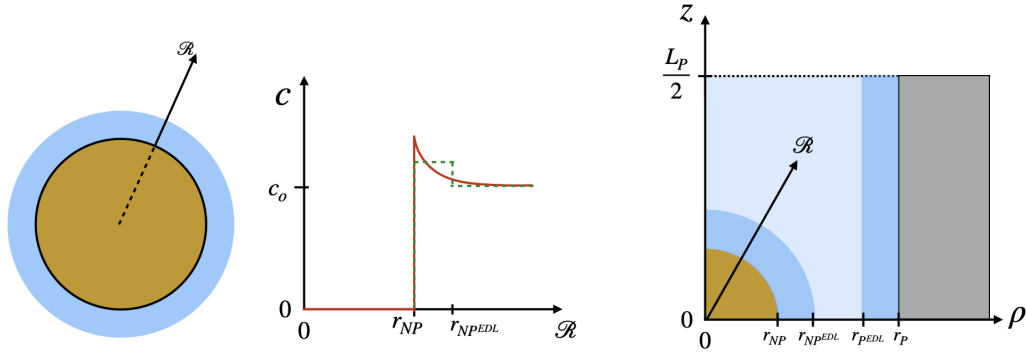
Figure 3.15: Counterion concentration along the radial direction following the exponential decay (solid line) and the simplified profile (dashed line). On the right, the colormap in ρz-plane represents the simplified concentration for both a charged cylindrical pore and charged spherical particle.

$$r_{PEDL} = r_P - m\kappa^{-1} \tag{3-41}$$

$$\delta n_{i,PEDL} = \frac{(\sigma_P A_P)/e}{V_{PEDL}} = \frac{(\sigma_P \pi d_P L_P)/e}{\pi(r_P^2 - r_{PEDL}^2)L_P} = \frac{\sigma_P\, d_P}{e(r_P^2 - r_{PEDL}^2)} \tag{3-42}$$

$$\gamma_{PEDL} = \sum \mu_i\, n_i\, z_i e = \gamma_o + \frac{\sigma_P\, d_P}{(r_P^2 - r_{PEDL}^2)} \tag{3-43}$$

$$R_{sphere,EDL} = R_{unaffected} + R_{affected} \tag{3-44}$$

$$
\begin{aligned}
R_{unaffected} &= \frac{1}{\pi}\int_0^{L_P/2 - r_{NPEDL}} \frac{1}{\int_0^{r_{PEDL}} \gamma_o\, \rho\, d\rho + \int_{r_{PEDL}}^{r_P} \gamma_{PEDL}\, \rho\, d\rho}\, dz \\
&= \frac{L_P/2 - r_{NPEDL}}{\pi}\left(\frac{1}{\gamma_o(1/2)r_{PEDL}^2 + \gamma_{PEDL}(1/2)(r_P^2 - r_{PEDL}^2)}\right) \\
&= \frac{L_P - 2\,r_{NPEDL}}{\pi}\left(\frac{1}{\gamma_o r_{PEDL}^2 + \gamma_{PEDL}(r_P^2 - r_{PEDL}^2)}\right) \\
&= \frac{4L_P}{\pi}\left(1 - \frac{2\,r_{NPEDL}}{L_P}\right)\left(\frac{1}{\gamma_o d_{PEDL}^2 + \gamma_{PEDL}(d_P^2 - d_{PEDL}^2)}\right)
\end{aligned}
\tag{3-45}
$$

$$R_{affected} = R_{affected,1} + R_{affected,2}$$

$$= \frac{1}{\pi} \int_0^{r_{NP}} \frac{1}{\int_\rho \gamma(\rho, z)\, \rho\, d\rho} dz + \frac{1}{\pi} \int_{r_{NP}}^{r_{EDL}} \frac{1}{\int_\rho \gamma(\rho, z)\, \rho\, d\rho} dz \tag{3-46}$$

$$R_{affected,1} = \frac{1}{\pi} \int_0^{r_{NP}} \frac{1}{\int_\rho \gamma(\rho, z)\, \rho\, d\rho} dz$$

$$= \frac{1}{\pi} \int_0^{r_{NP}} \frac{1}{\int_{\sqrt{r_{NP}^2 - z^2}}^{\sqrt{r_{NPEDL}^2 - z^2}} \gamma_{NPEDL}\, \rho\, d\rho + \int_{\sqrt{r_{NPEDL}^2 - z^2}}^{r_{PEDL}^2} \gamma_o\, \rho\, d\rho + \int_{r_{PEDL}^2}^{r_P} \gamma_{PEDL}\, \rho\, d\rho} dz$$

$$= \frac{1}{\pi} \int_0^{r_{NP}} \frac{1}{\frac{\gamma_{NPEDL}}{2}(r_{NPEDL}^2 - r_{NP}^2) + \frac{\gamma_o}{2}(r_{PEDL}^2 - r_{NPEDL}^2 + z^2) + \frac{\gamma_{PEDL}}{2}(r_P^2 - r_{PEDL}^2)} dz$$

$$= \frac{1}{\pi} \int_0^{r_{NP}} \frac{1}{\frac{\gamma_o}{2}\left[\frac{\gamma_{NPEDL}}{\gamma_o}(r_{NPEDL}^2 - r_{NP}^2) + \frac{\gamma_{PEDL}}{\gamma_o}(r_P^2 - r_{PEDL}^2) + \frac{\gamma_o}{\gamma_o}(r_{PEDL}^2 - r_{NPEDL}^2 + z^2)\right]} dz$$

$$= \frac{1}{\pi} \frac{2}{\gamma_o} \int_0^{r_{NP}} \frac{1}{\frac{\gamma_{NPEDL}}{\gamma_o}(r_{NPEDL}^2 - r_{NP}^2) + \frac{\gamma_{PEDL}}{\gamma_o}(r_P^2 - r_{PEDL}^2) + r_{PEDL}^2 - r_{NPEDL}^2 + z^2} dz \tag{3-47}$$

$$R_{affected,1} = \frac{1}{\pi} \frac{2}{\gamma_o} \int_0^b \frac{1}{p + z^2} dz = \frac{4L_P}{\pi} \frac{1}{2L_P} \left(\frac{1}{\sqrt{p}} \arctan \frac{b}{\sqrt{p}}\right) \frac{1}{\gamma_o}$$

$$b = r_{NP},$$

$$p = \frac{\gamma_{NPEDL}}{\gamma_o}(r_{NPEDL}^2 - r_{NP}^2) + \frac{\gamma_{PEDL}}{\gamma_o}(r_P^2 - r_{PEDL}^2) + r_{PEDL}^2 - r_{NPEDL}^2 \tag{3-48}$$

$$R_{affected,2} = \frac{1}{\pi} \int_{r_{NP}}^{r_{NPEDL}} \frac{1}{\int_\rho \gamma(\rho, z)\, \rho\, d\rho} dz$$

$$= \frac{1}{\pi} \int_{r_{NP}}^{r_{NPEDL}} \frac{1}{\int_0^{\sqrt{r_{NPEDL}^2 - z^2}} \gamma_{NPEDL}\, \rho\, d\rho + \int_{\sqrt{r_{NPEDL}^2 - z^2}}^{r_{PEDL}^2} \gamma_o\, \rho\, d\rho + \int_{r_{PEDL}^2}^{r_P} \gamma_{PEDL}\, \rho\, d\rho} dz$$

$$= \frac{1}{\pi} \frac{2}{\gamma_o} \int_{r_{NP}}^{r_{EDL}} \frac{1}{\frac{\gamma_{NPEDL}}{\gamma_o}(r_{NPEDL}^2) + \frac{\gamma_{PEDL}}{\gamma_o}(r_P^2 - r_{PEDL}^2) + r_{PEDL}^2 - r_{NPEDL}^2 + z^2} dz \tag{3-49}$$

$$R_{affected,2} = \frac{1}{\pi}\frac{2}{\gamma_o}\int_c^d \frac{1}{q+z^2}dz$$

$$= \frac{4L_P}{\pi}\frac{1}{2L_P}\frac{1}{\sqrt{q}}\left(\arctan\frac{d}{\sqrt{q}} - \arctan\frac{c}{\sqrt{q}}\right)\frac{1}{\gamma_o}$$

$$c = r_{NP},$$

$$d = r_{EDL},$$

$$q = \frac{\gamma_{NPEDL}}{\gamma_o}(r^2_{NPEDL}) + \frac{\gamma_{PEDL}}{\gamma_o}(r^2_P - r^2_{PEDL}) + r^2_{PEDL} - r^2_{NPEDL}$$

$$(3\text{-}50)$$

$$R_{sphere,EDL} = R_{unaffected} + R_{affected,1} + R_{affected,2}$$

$$= \frac{4L_P}{\pi}\left(1 - \frac{2\,r_{NPEDL}}{L_P}\right)\left(\frac{1}{\gamma_o d^2_{PEDL} + \gamma_{PEDL}(d^2_P - d^2_{PEDL})}\right)$$

$$+ \frac{4L_P}{\pi}\frac{1}{2L_P\gamma_o}\left[\frac{1}{\sqrt{p}}\arctan\frac{b}{\sqrt{p}} + \frac{1}{\sqrt{q}}\left(\arctan\frac{d}{\sqrt{q}} - \arctan\frac{c}{\sqrt{q}}\right)\right]$$

$$b = r_{NP},$$

$$p = \frac{\gamma_{NPEDL}}{\gamma_o}(r^2_{NPEDL} - r^2_{NP}) + \frac{\gamma_{PEDL}}{\gamma_o}(r^2_P - r^2_{PEDL}) + r^2_{PEDL} - r^2_{NPEDL}$$

$$c = r_{NP},$$

$$d = r_{EDL},$$

$$q = \frac{\gamma_{NPEDL}}{\gamma_o}(r^2_{NPEDL}) + \frac{\gamma_{PEDL}}{\gamma_o}(r^2_P - r^2_{PEDL}) + r^2_{PEDL} - r^2_{NPEDL}$$

$$(3\text{-}51)$$

The model predictions for charged nanospheres at $0.100\,mol/L$ are presented in Figure 3.16.

Figure 3.13 shows the predicted relative resistance in relation to open pore configuration, caused by the insertion of a charged nanosphere in a range 1 to 100 mM. In this case, instead of constant charged density, we assume a constant zeta potential of $7\,mV$. The charge density calculated by the Equation 1-10 (DOANE et al., 2011), giving values between 1 to 8 mC/m^2. The model predicts only resistive pulses for this range of concentration. Unfortunately, again the simplified model seems to not capture important aspects of the phenomenon to match the experimental results. Not only did Goyal, Freedman e Kim (2013) report conductive pulses for gold spheres in 20 mM KCl, but our experimental results with spherical particles shown a crossover from resistive to conductive pulses with the decrease of salt concentration, as Figures 3.18 and 3.19 show.

Due to the lingering questions regarding aspects of conductive pulses
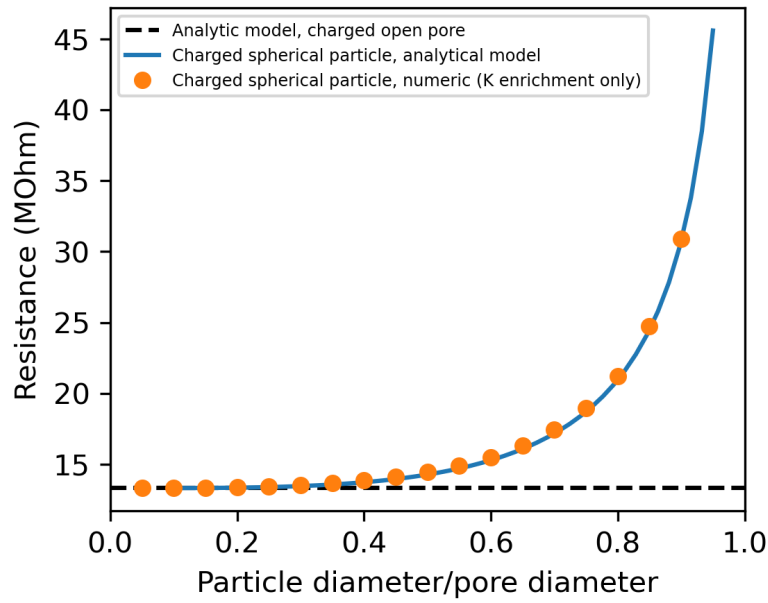
Figure 3.16: Pore resistance in the presence of spherical particles. $d_P = 100\,nm$, $[KCl] = 0.100\,mol/L$ and $\sigma = 20mC/m^2$.
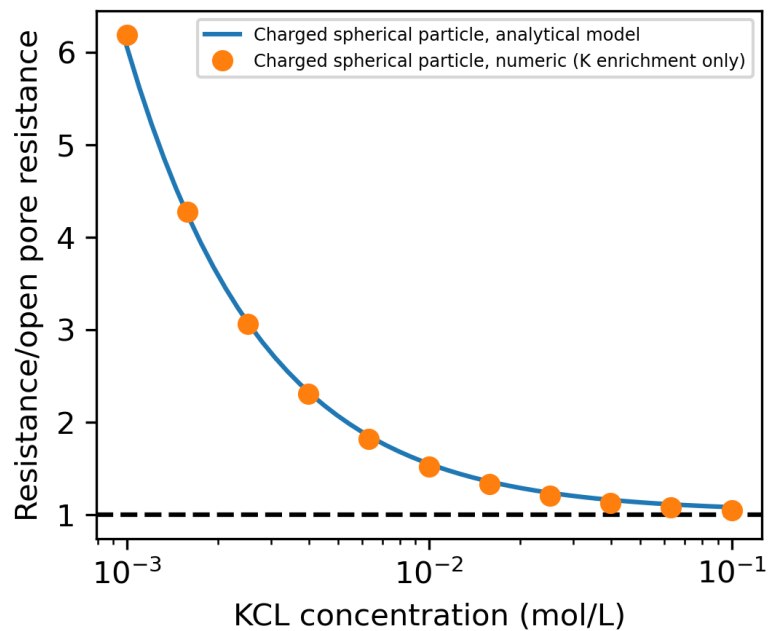
Figure 3.17: Relative resistance (to open pore) caused by charge spherical particle with $d_{NP} = 30nm$ and $\sigma_{rod} \approx 1 - 8\,mC/m^2$. $[KCl] = 0.010\,mol/L$, $L_P = 100\,nm$, $d_P = 80\,nm$ and $\sigma_P = 20mC/m^2$.
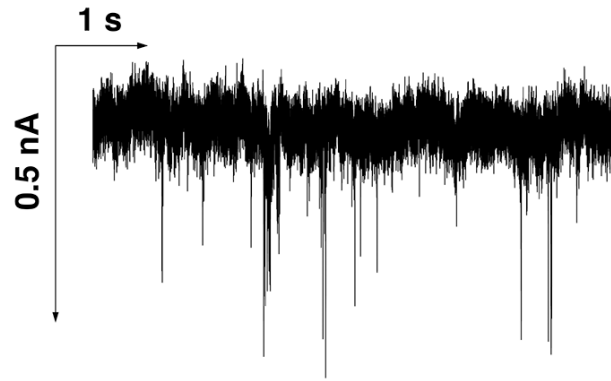
Figure 3.18: Experimental ionic current as a function of time over an interval of approximately 10s of $d_{NP} = 30$ nm CTAB-coated Au nanoparticle with [KCl] $= 500$ mM.
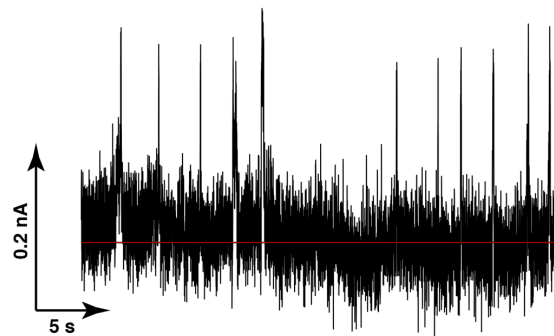
Figure 3.19: Experimental ionic current as a function of time for $d_{NP} = 30$ nm citrate-coated Au nanoparticle with [KCl] $= 50$ mM.

and current limitations on PNP simulations, the next few Chapters will focus on the study of translocation considering uncharged surfaces to calculate the potential, leading to resistive pulses.

3.7
Summary

In this chapter, analytical models for predicting the characteristic current in nanopores were proposed for open-pores and pores with a spherical or a rod particle inside, considering both uncharged and charged surfaces. Using the same framework (single-resistor circuit approximation), models already available in the literature were recovered and new models for spherical and rod particles were obtained. Even without a quantitative agreement with the experimental data, the model for a charged rod was able to predict the appearance of conductive pulses in low salt concentration.

4
Electrophoretic Motion of Unconfined, Spherical Nanoparticles

4.1
Electrophoresis of a Sphere in a Uniform Field

In a uniform field, analytical expressions of the mean behavior can be derived from the probability density function of the Metropolis scheme (Equation 2-6), which can be used to test the code implementation and compare the results with electrophoretic theory. In addition, these expressions can be used to check the sensibility of the results with the simulation parameters.

The total potential of the particle is the product of the charge q and the electrostatic potential V:

$$U = q\,V \tag{4-1}$$

The component of the electrostatic field in a given direction is given by the negative of the gradient of the electrostatic potential V:

$$\mathbf{E} = -\nabla V \tag{4-2}$$

The potential U of a particle with charge q under an electrostatic field $\mathbf{E}$ uniform along the x-direction (with the only non-zero component $E_x = E$) can be described by:

$$U = -q\,E\,x \tag{4-3}$$

The change in potential ΔU result from a displacement δx is then:

$$\Delta U = -q\,E\,\delta x \tag{4-4}$$

The mean velocity $\overline{v}$ is the ratio of the mean displacement $\overline{\delta x}$ and time-step δt

$$\overline{v} = \frac{\overline{\delta x}}{\delta t} \tag{4-5}$$

The (mean) electrophoretic mobility μ_e can be calculated as the ratio of the velocity and the field strength:

$$\mu_e = v/E \tag{4-6}$$

As stated in section 2.3, the time step is calculated from the intrinsic (MC) time-step corrected by the acceptance. To derive an analytical expression of the electrophoretic mobility, then, we must derive the expressions for the acceptance $\mathcal{A}$ and the mean displacement $\overline{\delta x}$.

4.1.1
Derivation of Acceptance

Acceptance can be derived from the probability distribution function of the trial acceptance (Equation 2-6) integrated over the interval I:

$$\mathcal{A} = \frac{\int_I p(\Delta U) \, d\Delta U}{\int_I 1 \, d\Delta U} \tag{4-7}$$

The interval I is defined by the maximum displacement allowed δx_{max}:

$$I = (\Delta U(-\delta x_{max}), \ \Delta U(\delta x_{max})) \tag{4-8}$$

From Equation 4-4:

$$\Delta U(\pm \delta x_{max}) = \mp \Delta U_{max} = \mp q \, E \, \delta x_{max} \tag{4-9}$$

$$\mathcal{A} = \frac{\int_{\Delta U_{max}}^{-\Delta U_{max}} p(\Delta U) \, d\Delta U}{\int_{-\Delta U_{max}}^{\Delta U_{max}} 1 \, d\Delta U} \tag{4-10}$$

$$\mathcal{A} = 0.5 + \frac{1 - exp(-\beta \Delta U_{max})}{2 \, \beta \Delta U_{max}} \tag{4-11}$$

4.1.2
Derivation of Mean Displacement

A schematic of the procedure for obtaining the mean displacement is shown in Figure 4.1. The upper left panel **A** represents the probability of accepting the trial move as a function of the change in potential, as defined by the Metropolis scheme.

For a positively charged particle in linearly decreasing potential the field points to the positive direction, so all the positive displacements in x are accepted and some of the negative displacements are not, as depicted in **B**. Also, the position of the rejected trials remains the same, so all the probability density of the rejections (red area in **B**) are transferred to zero.

Since the density of the spike in zero is known, it is possible to calculate the mean displacement by calculating the expected value of the distribution without considering the spike (δx^* in **C**) and weight averaging it with the spike in zero **D**:

$$\overline{\delta x} = \mathcal{A} \, \overline{\delta x}^* + (1 - \mathcal{A}) \, 0 \tag{4-12}$$
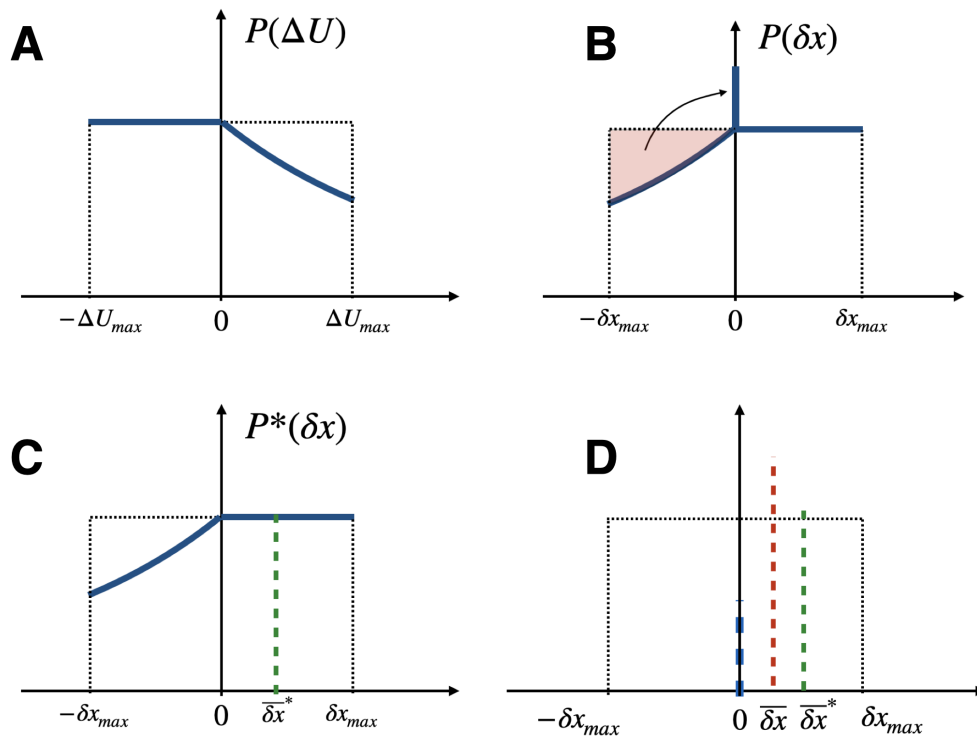
Figure 4.1: Scheme illustrating the expected value of a displacement

From Equation 4-4, the mean displacement $\overline{\delta x}$ can be computed from the Metropolis acceptance as:

$$\overline{\delta x} = \frac{\mathcal{A}}{-q\,E}\,\overline{\Delta U} \tag{4-13}$$

The normalized probability function of the potential U:

$$P(\Delta U) = \frac{p(\Delta U)}{\int_{-\Delta U_{max}}^{\Delta U_{max}} p(\Delta U)\,d\Delta U} \tag{4-14}$$

$$P(\Delta U) = \frac{p(\Delta U)}{\Delta U_{max} + \frac{1-exp(-\beta\Delta U_{max})}{\beta}} \tag{4-15}$$

From these considerations, the expected value of the potential change is:

$$\overline{\Delta U} = \int_{-\Delta U_{max}}^{\Delta U_{max}} \Delta U\,P(\Delta U)\,d\Delta U \tag{4-16}$$

$$\overline{\Delta U} = \frac{1-exp(-\beta\Delta U_{max})(\beta\Delta U_{max}+1)}{\beta^2\Delta U_{max}+\beta-\beta exp(-\beta\Delta U_{max})} - \frac{\Delta U_{max}^2}{2\Delta U_{max}+\frac{2-2exp(-\beta\Delta U_{max})}{\beta}} \tag{4-17}$$

The mean displacement then is calculated by substituting equations 4-10 and 4-17 in equation 4-13.
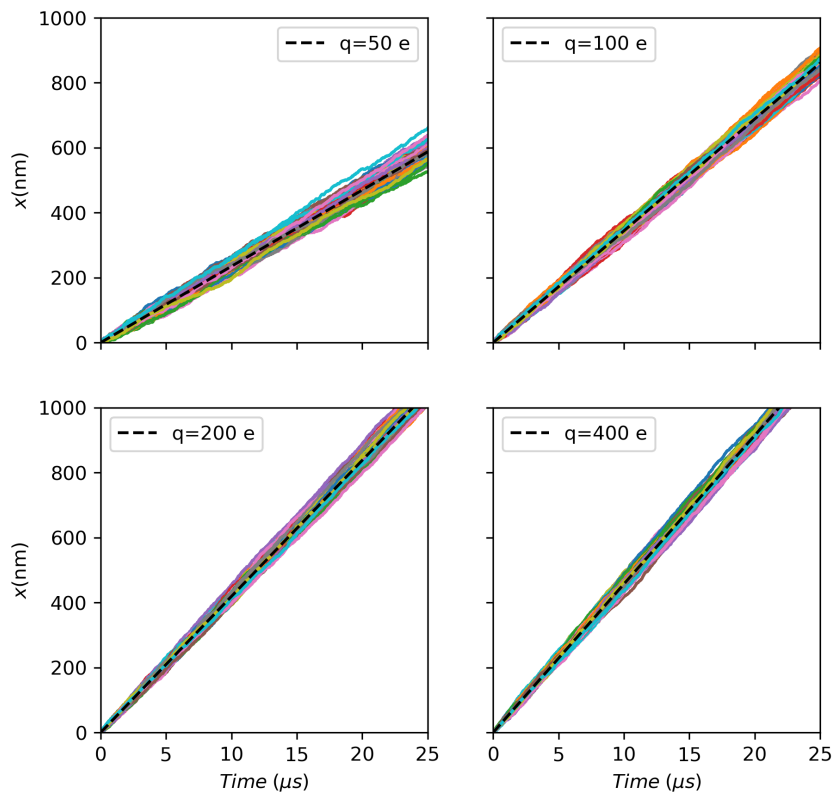
Figure 4.2: Position as a function of time for 100 trajectories at different values of charge. The dotted black line indicates the mean.

4.2
Comparison with Simulations: Effect of Charge

Figure 4.2 shows results from simulations with different values for charge. Each colored line represents one of 100 trajectories in the x-direction, using $d_{NP} = 30\,nm, E = 1.0\,mV/nm$ and $\delta x_{max} = 1\,nm$:

The results of acceptance, mean displacement, velocity, and mobility from those simulations are compared with the analytical expressions in Figure 4.3, showing an excellent agreement.

The simulations regarding the previous were done in three dimensions, imposing the field only the x-direction. Figure 4.4 shows the squared displacement in the directions not submitted to the field ($\rho^2 = y^2 + z^2$). The recovered diffusion coefficient from the mean squared displacement is very close to the Stokes-Einstein equation and insensitive to the field strength in the x-direction, varying only due to the inherent variance of the Brownian motion and the finite sampling.
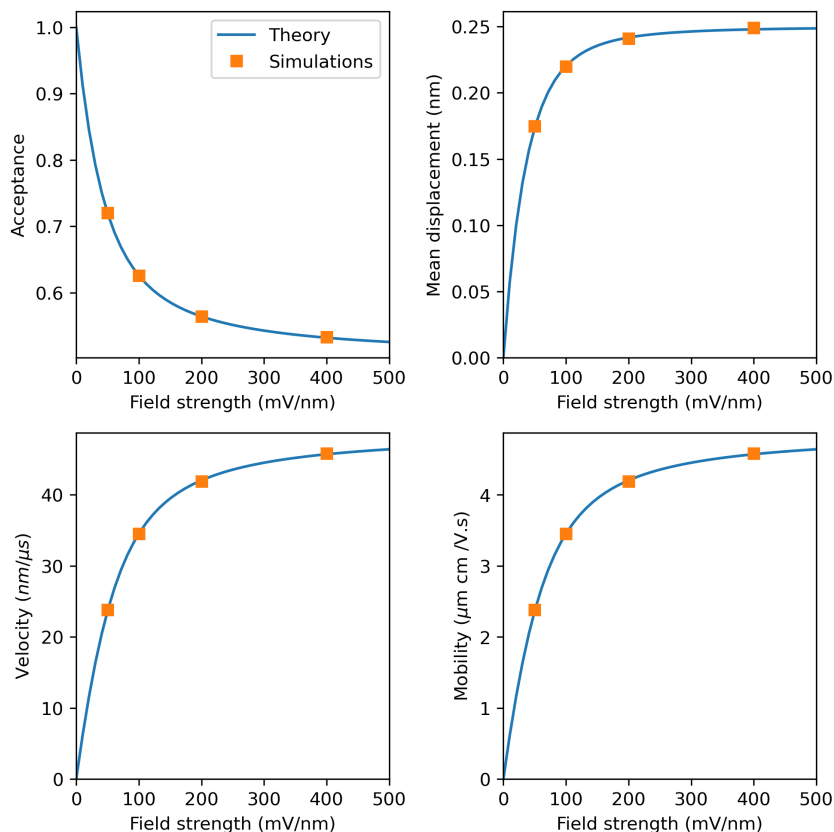
Figure 4.3:   Acceptance, mean displacement, velocity, and mobility as a function of charge.

4.3
Comparison with Electrophoretic Theory

Figure 4.5 **A** shows the total charge as a function of zeta potential for three values of particle diameter, with aqueous monovalent salt (e.g. KCl) solution at concentration of 0.1 mol/L int he low potential regime. Panel **B** shows the mobility as a function of charge in the low potential regime, with values around $1 \mu m.cm/(V.s)$, commonly measured experimentally. Figure 4.5 **C** shows the analytical solution of DMC under constant field using $E = 1.0\ mV/nm$ and $\delta x_{max} = 1\ nm$. Comparing panels **B** and **C** shows that for the same charge, the DMC approach results in mobilities more than 10 times the predicted by the electrophoresis equation. The simple potential expressed by Equation 4-1 does not take into consideration the drag from the solvent and the ionic cloud in the motion of the charged particle. It was chosen to keep the simple form of the potential (Equation 4-1) for the simulations and use nonphysical values of charge that result in desired mobility. It is emphasized that in other measurement technologies, such as Dynamic Light Scattering, mobility is also the fundamental property of measurement, being the charge back-calculated using electrophoretic theory.
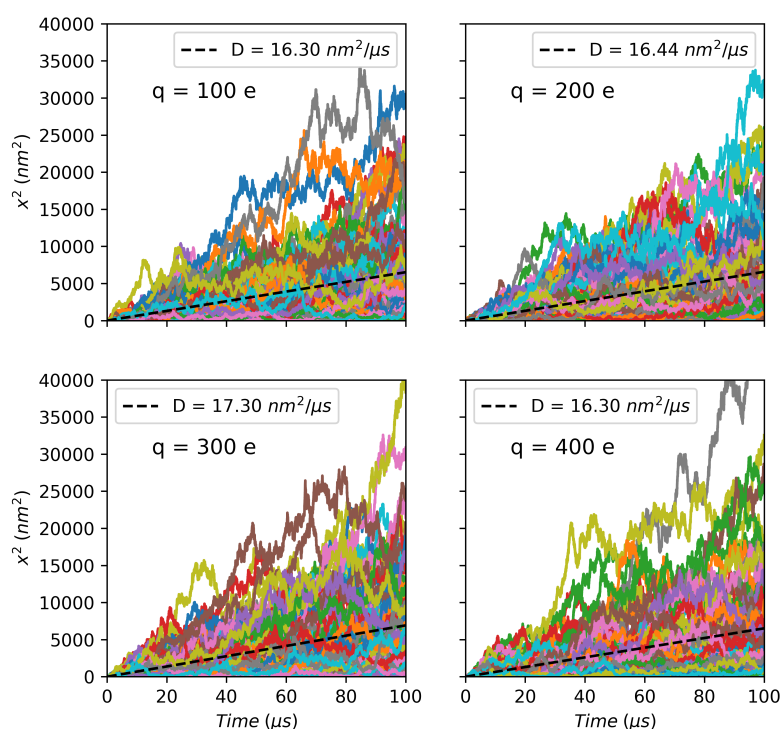
Figure 4.4: Squared displacement (in y and z directions) as a function of time for 100 particles trajectories. The dashed line indicates MSD, from which the diffusion constant D was calculated. Imposed $D = 16.34 \; nm^2/\mu s$.
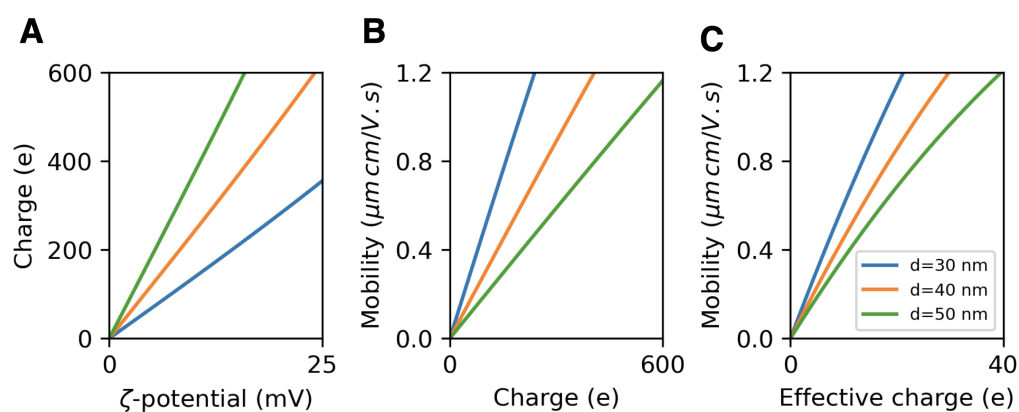
Figure 4.5: (**A**) Charge as a function of zeta potential and (**B**) Mobility as a function of charge, calculated by electrophoresis theory; (**C**) Mobility as a function of charge calculated analytical expression of DMC in a uniform field.
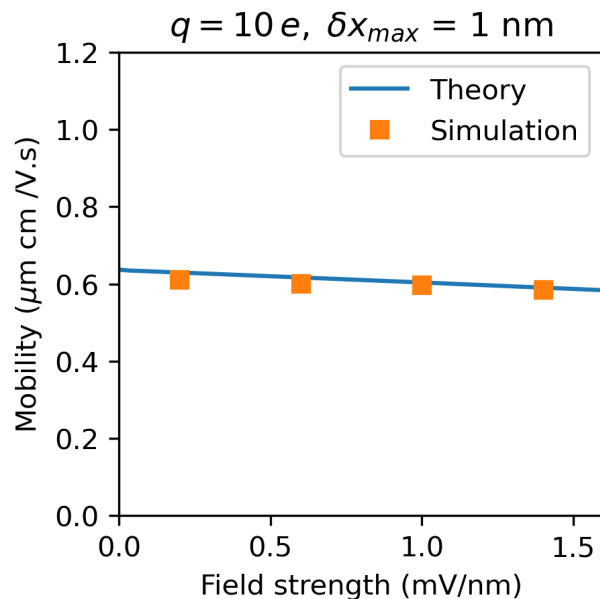
Figure 4.6: Mobility as a function of field strength. $d_{NP} = 30\,nm$, $q = 10\,e$ and $\delta x_{max} = 1\,nm$.

4.4
Comparison with Simulations: Effect of Field Strength

The time scaling used in DMC works under the assumption of acceptance probability does not depend on the step size or direction of the displacement. Although this is never true in a monotonically increasing potential as it is used here, it should hold a good approximation in the case of small displacements. Another consequence of this violation is the fact that mobility turns out to be dependent on the field strength, which is not expected experimentally. However, for field strength values typically found in the configurations in this study, the variation in the mobility with the field is very low, as is shown in Figure 4.6.

4.5
Summary

This chapter presented the dynamic Monte Carlo simulation of unconfined spherical particles in a uniform electrostatic field, allowing the comparison of the results with the predictions from diffusion and electrophoresis theory.

An analytical expression for the expected mobility in DMC simulation was derived, allowing checking the algorithm implementation and accurately scaling the charge of the particles to obtain a desirable electrophoretic mobility.

The results of the simulations using the values of effective charge confirmed the correct modeling of Brownian and electrophoretic motion by dynamic Monte Carlo simulations.

5
Simulation of the Translocation of Spherical Nanoparticles

5.1
Modeling the Electrostatic Potential and Current in a Nanopore by PNP

Before investigating nanoparticle translocation with DMC simulations, PNP calculations were performed to determine the electrostatic potential and ionic current for a series of imposed nanoparticle positions.

5.1.1
Open Pore

Figure 5.1 shows a slice of the electrostatic potential in the xz-plane for $y = 250\ nm$ in the open pore configuration without a nanoparticle present. The dashed lines in the figure indicate the position of the membrane which contains the nanopore.

One important question is how these results can relate to the values in an experimental setup, where the electrodes are several millimeters from each other, much more separated than the size of the domain ("box") used in the simulations. In fact, most of the variation in the electrostatic potential predicted by the PNP simulations occurs in the region of the membrane, in agreement with the literature(OEFFELEN et al., 2012). However, not all the voltage drop is due to the membrane, which indicates the size of the box also
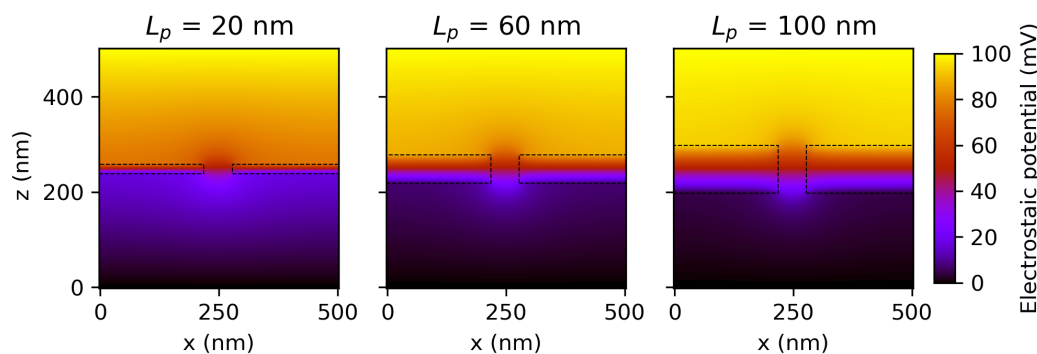
Figure 5.1: Electrostatic potential in the xz-plane for $y = 250\ nm$. The dashed lines denote the boundaries of the membrane.
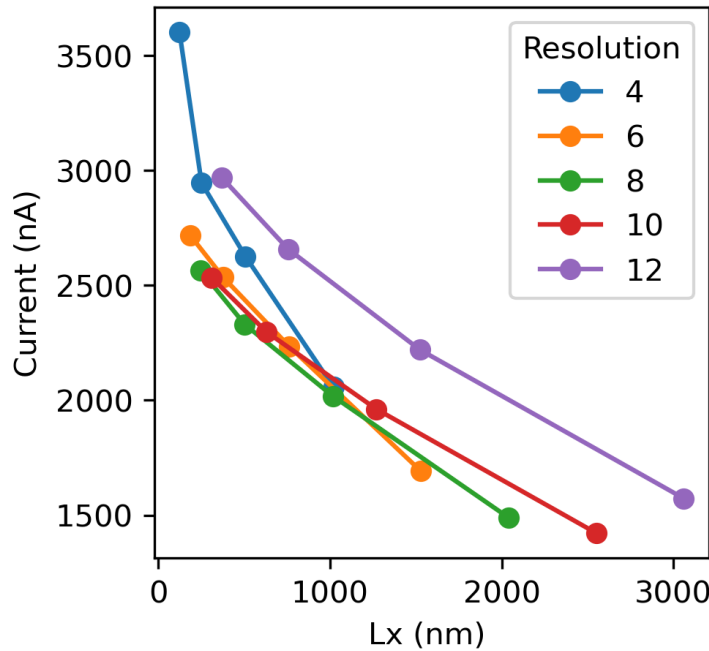
Figure 5.2: Effect of box edge size Lx on the open-pore current calculated by PNP. $d_P = 60$, $L_P = 100$, $[KCl] = 0.1$ and V = 0.1 V.

influences the actual voltage inside the pore and the total current across the pore.

To test that hypothesis, simulations with different box sizes were made. Due to the limitation in the total memory available, larger boxes demanded lower resolution, which can also have an impact on the results. Figure 5.2 shows the effect of box edge size Lx on the open-pore current calculated by PNP, where each line represents a different simulation resolution ($Lx/[N_{layers} - 1]$).

The current values decrease with increasing box size. However, the relative change is lower as the size of the box, suggesting a possible convergence to a single value for very large box sizes. Tsutsui et al. (2019) in their FEM simulations set the size of the domain to match the open-pore current recorded in the experiments. For the size of the box used in the following sections for nanospheres ($L_x = 128$ nm, resolution $\approx 4 \, nm$) the results match the predicted by analytical models of the previous section and the experimental results.

The current response also depends on salt concentration. Figure 5.3 shows the results for the simulated open-pore current for KCl concentrations ranging across several orders of magnitude. The figure shows also the estimated values of the model from Equation 3-10. The results of the simulation have great agreement with the model and scale linearly with salt concentration, as is expected for pores with uncharged surfaces.
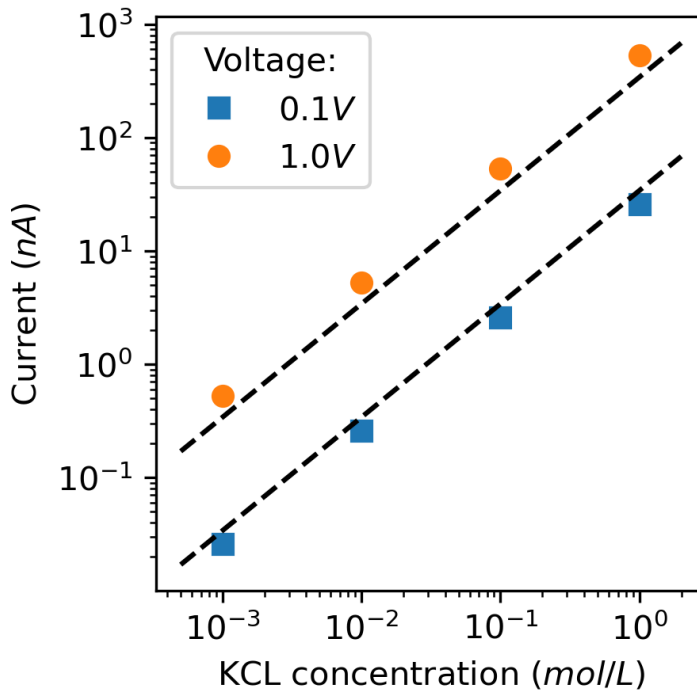
Figure 5.3: Effect of salt concentration. $d_P = 60$ nm, $L_P = 100$ nm, $[KCl] = 0.1$ mol/L and voltages of 0.1 V and 1.0 V.

5.1.2
Effect of a Spherical Particle Inside the Nanopore

When a nanoparticle is placed in the nanochannel it influences the electrostatic potential nearby. However, as both particle and membrane are treated as uncharged surfaces in the PNP calculations, the potential at the center of the particle is the same as the potential calculated in the open pore. Figure 5.4 shows the difference between the electrostatic potential with and without a nanoparticle in the center.

Far from the membrane, the electrostatic potential is essentially unchanged when a nanoparticle is present in the pore. However, near the nanoparticle, the electrostatic potential immediately above and below the particle can vary as much as ± 10 mV relative to the open pore for the parameters that were investigated.

To mimic real particle translocation events, the effect of the particle position on the current was investigated for several off-axis positions. These data confirm that setting the initial particle position *ca.* 100 nm away from the mid-point of the nanopore does not significantly impact the ionic current. Indeed, the presence of the nanoparticle only begins to affect the value of the ionic current when it is within approximately 10 nm of the entrance regardless of the amount the particle is offset from the nanopore's central axis. Previous
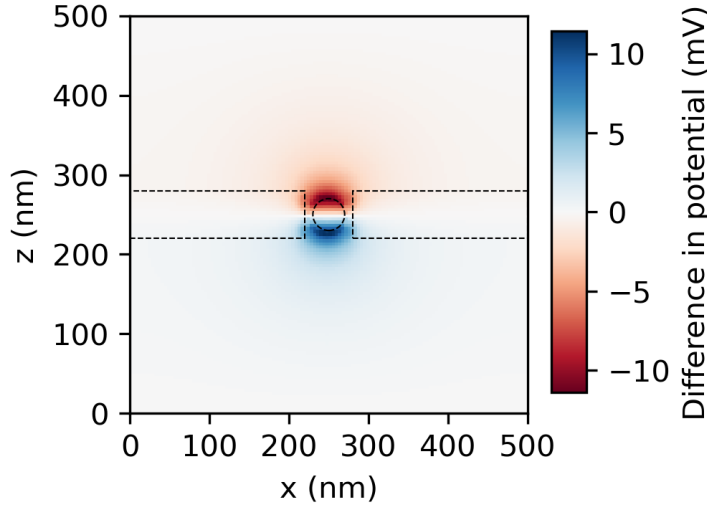
Figure 5.4:   The difference in electrostatic potential between the open pore configuration and with a particle in the center of the pore.

work(TSUTSUI et al., 2015; QIN; ZHE; WANG, 2011) has found that off-axis positions of the nanoparticle lead to higher values of the blockade current than for nanoparticles in the center of the pore, and that this effect becomes more prominent as the pore length decreases. The origin of the increased blockade currents is due to an increase in the resistance attributed to non-uniformities in the electric field that occur for off-axis nanoparticle positions.

Figure 5.5 shows the values of the ionic current as a function of a $d_{NP} = 40 \ nm$ particle's position within a $60 \ nm$ diameter pore (z) in z for three values of the x-position: one at the the central axis of the pore ($x = 250$ nm, blue circles) and two positions that are offset by $5 \ nm$ ($x = 255$ nm, orange circles) and $10 \ nm$ ($x = 260$ nm, green circles). Unlike previous calculations(TSUTSUI et al., 2015), off-axis positions result in smaller blockades. However, this study considered ionic strengths which are orders of magnitude larger those previous studies, making a direct comparison difficult.

Using the model for open-pore resistance (Equation 3-10) and using a term for access resistance (Equation 1-21), the open-pore current can be estimated by:

$$i_0 = \frac{\pi V_b d_p^2}{(4L_p + \pi d_p)} \left[\frac{1}{\rho_{K^+}} + \frac{1}{\rho_{Cl^-}} \right] \qquad (5\text{-}1)$$

where $V_b = 100 \ mV$ is the applied bias.

The above expression predicts $i_0 \approx 2.9 \ nA$, compared to $i_0 \approx 3.2 \ nA$ produced from the PNP calculations. Thus, the PNP calculations are in near quantitative agreement with the expected ionic current through the pore. As expected, as the nanoparticle moves deeper into the pore (i.e., as distance
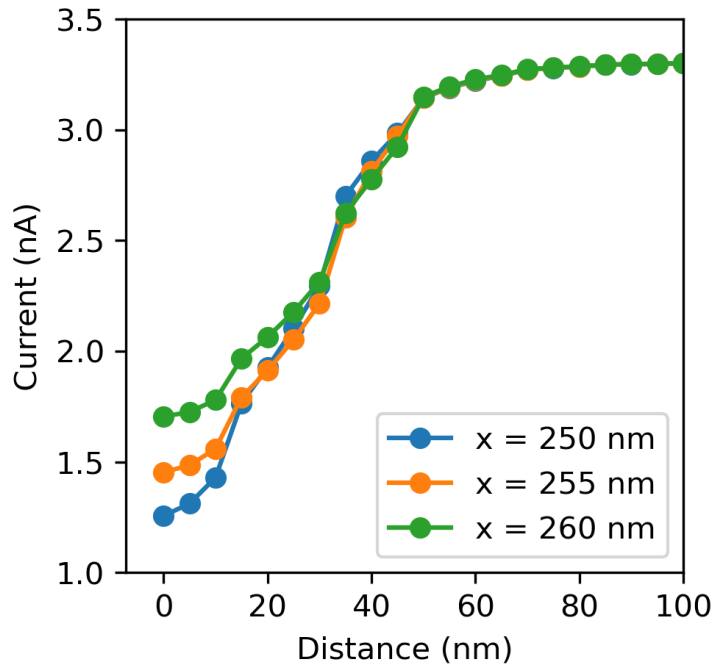
Figure 5.5: Current as a function of distance for three straight trajectories along the z-direction of the nanopore ($d_P = 60\ nm$, $L_P = 60\ nm$). A distance of 0 nm corresponds to the position $z = 250\ nm$. As the particle is offset in increments of 5 and 10 nm ($x = 255\ nm$ and $260\ nm$, respectively) from the central axis of the nanopore ($x = 250\ nm$), the minimum current increases implying that fewer ions are blocked by the particle. The nanoparticles in these simulations had diameters of $d_{NP} = 40\ nm$ and mobilities of $\mu_{NP} = 0.8\ \mu m\ cm/V \cdot s$.

decreases in Figure 5.5), the ionic current decreases due to blockage by the particle.

More positions were evaluated for the three pore diameters and three particle sizes used in this study to ensure enough data for the current interpolation by the DMC code. Figure 5.6 shows the current as a function of the particle position calculated by PNP for three pore lengths and three particle diameters.

5.2
Modeling Electrostatic Potential in a Nanopore by ML

A subset of PNP results were used to train the MLP neural network (NN), and its predictions were compared to a separate set of PNP calculations to assess the accuracy of the predictions as a function of the NN architecture. The difference between the PNP calculation and NN predictions is shown in Figure 5.7 for 2, 6, and 10 layers of neurons (rows, left to right) containing 10, 50, and 100 neurons in each layer (columns, top to bottom). Perfect agreement
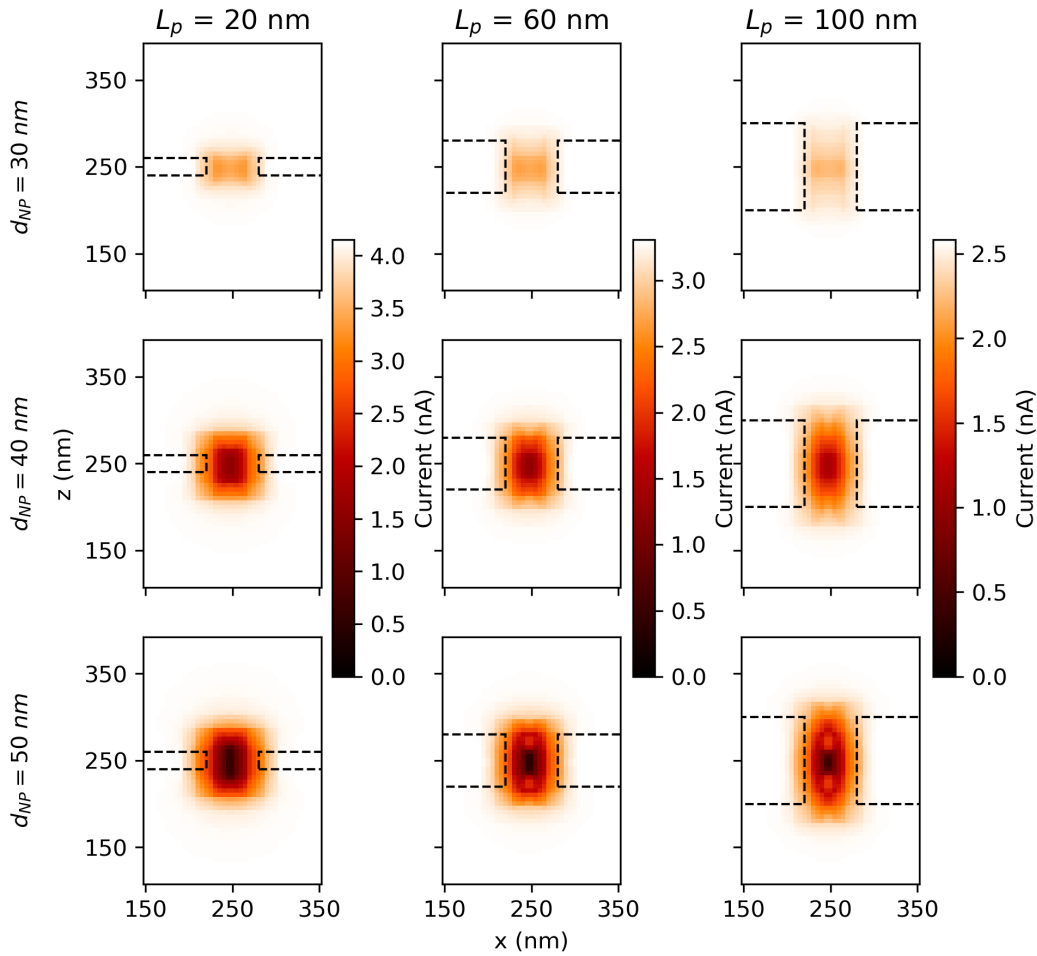
Figure 5.6: Current as a function of the particle position calculated by PNP. Each colorbar represents the scale in the plots of the same L_p.

between PNP and the MLP NN would be indicated by an absence of color. The minimum number of layers and neurons per layer that accurately reproduce the electrostatic potential in the membrane occurs for 6 layers of 50 neurons, and the accuracy of the NN prediction increases with both increasing numbers of layers and/or an increase in the number of neutrons per layer.

5.3
Translocation of Nanospheres

DMC simulations were performed for three values of nanopore lengths of $L_P = 20$, 60, and 100 nm, and three values of nanoparticle diameter of $d_{NP} = 30$, 40, and 50 nm. In all simulations, the nanopore diameter was fixed at $d_p = 60$ nm. Figure 5.8 shows a 2D slice in the xz-plane of two nanoparticle center-of-mass trajectories, highlighting two distinct classes of events. For these trajectories, the nanoparticle mobility was fixed at $\mu_{NP} = 0.8$ μm $cm/V{\cdot}s$. The trajectory drawn in black shows a particle fully translocate through the pore,
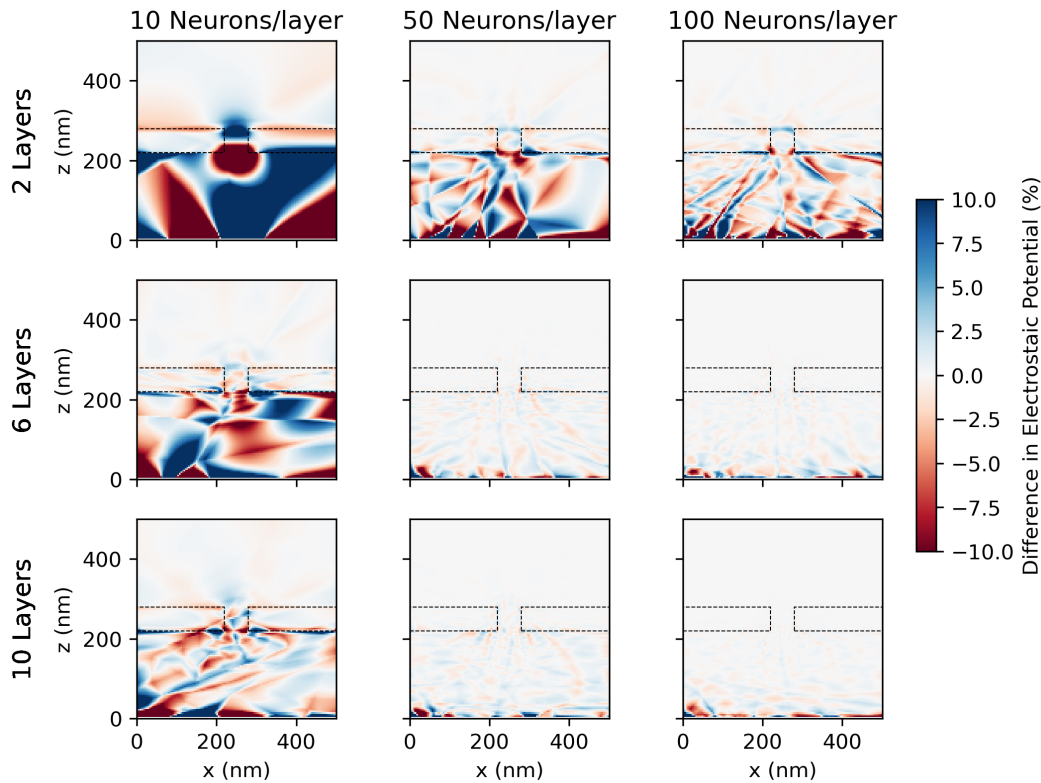
Figure 5.7: Difference between the electrostatic potential calculated by PNP and predicted by the neural network for a nanopore with diameter $d_P = 60$ nm and length $L_p = 60$ nm for (top to bottom) 2, 6, and 10 layers in the network, and for (left to right) 10, 50 and 100 neutrons per layer. The dashed line denotes the position of the membrane. For all NN configurations, the nanoparticle diameter was fixed at $d_{NP} = 40$ nm.

which will be referred to a true "translocation event". In contrast, the trajectory drawn in blue is representative of a class of event in which the particle passes near the entrance of the nanopore and causes a detectable change in the ionic current, but diffuses away from the nanopore without ever entering. Here, these events will be referred as "collisions," although such events have also been called "bounce-off"(LENART et al., 2019) or "fly-by"(TSUTSUI et al., 2015) elsewhere in the literature. Figure 5.8 also shows the relative change in the ionic current through the pore for different particle positions, represented by the red color map of the figure. For the simulations, the current always decreases when a particle is within the pore, and for the values of nanoparticle diameter and pore size considered in the figure, the current decreases by as much as $40 - 60\%$ for positions in the central portion of the channel.

To assess the uniformity of the translocation and collision events, 100 independent events were overlayed, as shown in Figure 5.9. The events are characterized by the z-coordinate (i.e., position along the central axis of the nanopore) of the center-of-mass of a $d_{NP} = 40$ nm nanoparticle as a function
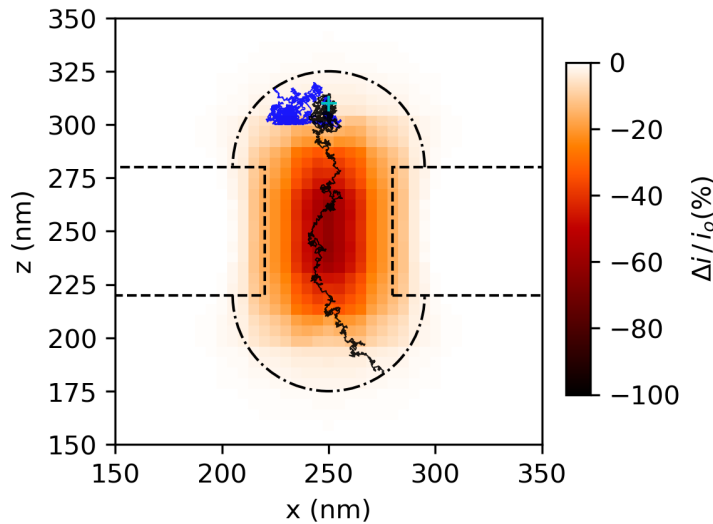
Figure 5.8: Schematic of the configuration used to set the events. Dotted lines represent the membrane/pore location, whereas the dash-dotted lines indicate the boundaries where the trajectories are terminated. Projections of two trajectories are depicted in black (translocation) and blue (collision) lines. The color map shows the relative blockade caused by a $d_{NP} = 40$ nm particle positioned in each location. For these simulations, $d_P = L_P = 60$ nm.

of time for a configuration with $L_P = 60$ nm, and a particle mobility of 0.8 μm $cm/V \cdot s$. The trajectories from translocation and collision events are depicted as black and blue lines, respectively. From the overlayed events, the slope of the black lines between $z = 300$ nm and $z = 200$ nm is relatively consistent between independent events, indicating that the particles move through the pore with comparable velocities with some small variations due to Brownian motion. The dwell time of the nanoparticles is roughly on the order of $\tau = 50$ μs. Additionally, although most collision events consist of nanoparticles that diffuse in the vicinity of the entrance of the nanopore and only slightly disrupt the ionic current, occasionally nanoparticles enter the pore, as shown by those trajectories in the figure with a z-coordinate that is less than the sum of the top surface location and the radius of the nanoparticle ($z = 300$ nm). However, the simulations showed that the nanoparticles in such events do not enter more than about $10 - 15$ nm into the pore (*i.e.*, on the order of the radius of the nanoparticle). Experimentally, these events may be difficult to resolve due to their short duration and the relatively small amplitude of the blockade events, which it is discussed in more detail below. Nevertheless, collision events have been detected experimentally(TSUTSUI et al., 2015; MCMULLEN et al., 2014).

Since the presence of collision events can affect interpretation of the measurements, they usually have to be removed from the analysis or at least
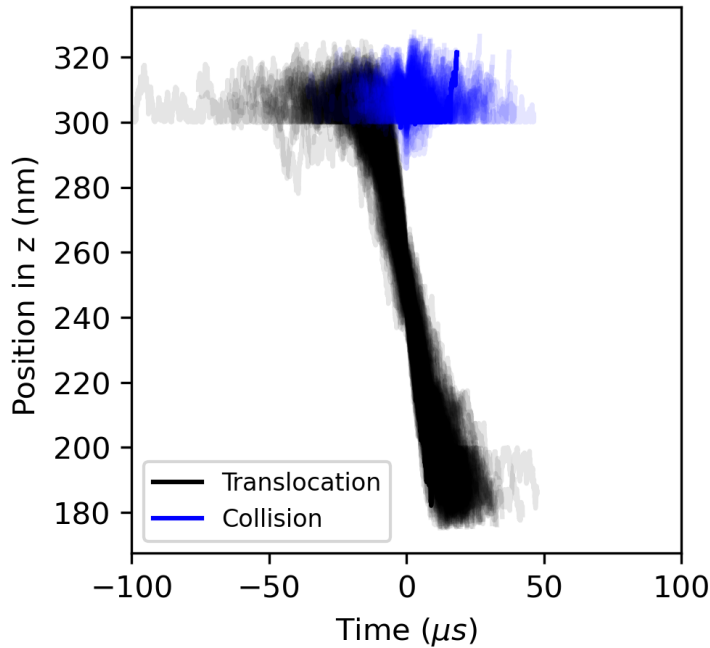
Figure 5.9: Position in the z direction as a function of time for 500 overlapped events for nanoparticles with $d_{NP} = 40$ nm and $\mu_{NP} = 0.8 \mu m \ cm/V \cdot s$. Full translocation events are shown in black while collisions are shown in blue. The nanopore in these simulations had a diameter of $d_P = L_P = 60 \ nm$.

correctly identified. For this reason, DMC simulations were used to determine the relative frequency of true translocation events relative to all events. Figure 5.10 plots the translocation ratio (*i.e.*, the ratio of translocation events relative to all events) as a function of nanoparticle mobility for nanoparticles with varying diameters and for three values of nanopore length. Circle, plus, and square points correspond to nanoparticles with diameters of $d_{NP} = 30, 40,$ and $50 \ nm$. The colors of the points correspond to nanopores with lengths of $L_P = 20 \ nm$ (blue), $60 \ nm$ (orange), and $100 \ nm$ (green). DMC simulations confirmed that for fixed d_{NP} and L_P, the translocation ratio increased from 20% to near 70% as the nanoparticle mobility increased from $\mu_{NP} = 0.4$ $\mu m \ cm/V \cdot s$ to $1.2 \ \mu m \ cm/V \cdot s$ for $d_{NP} = 50 \ nm$ and $L_P = 100$ nm. In general, as either d_{NP} or L_P decreased, the fraction of translocation events increased, but for different reasons. As d_{NP} decreases, there is a greater probability for the nanoparticle to be located in a lateral position in the nanopore that will allow it to fully pass across the membrane. In contrast, as L_P decreases, the probability of the nanoparticle completely move through the channel increases since the path length it must diffuse across decreases.

Coupling the DMC simulations to PNP calculations of the ionic current with the MLP NN allowed the attainment of the current traces for all of the 100 events shown in Figure 5.9. Figure 5.11 plots these current traces as a
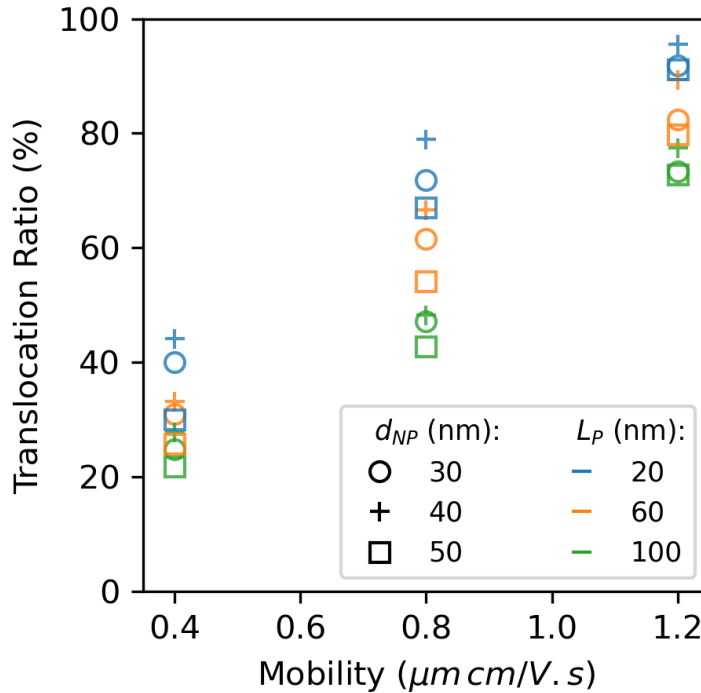
Figure 5.10: Translocation ratio as a function of nanoparticle mobility, diameter, and nanopore length. The nanopore diameter was fixed at $d_P = 60$ nm for all simulations.

function of time, where the events were overlayed such that the minimum current in each event coincided with $t = 0$ μs. Translocation events collapsed into a well defined curve, with average blockades of $\Delta i \approx 3$ nA. Because DMC simulated many different trajectories, the data in Figure 5.11 also provide insight into the variability of the resistive pulses. However, the simulations only contains fluctuations from the Browninan motion of the nanoparticles, whereas experimental signals also influenced for many other sources of noise(LIANG et al., 2020). Thus, the noise that is significantly lower than what might be seen experimentally. Nevertheless, from inspection of the width of the overlayed translocation events, the magnitude of the pulse varied from about 1.25 nA to 3 nA. In contrast to the translocation events, while some collision events produced a noticeable decrease in the current of $\Delta i \approx 0.25 - 0.75$ nA, other events did not produce an appreciable decrease in the current. In terms of dwell times, translocation events took on the order of $\tau = 50$ μs, as previous discussed, while collisions occurred at much shorter times as is evident from the much narrower pulse widths in Figure 5.11. As shown in previous work from White *et al.*, the short duration of the collision events combined with low-pass filters used in typical experiments means that experimentally, such collision events may be extremely attenuated or not detectable, depending on the dwell time, cutoff frequency of the low-pass filter, and the sampling rate
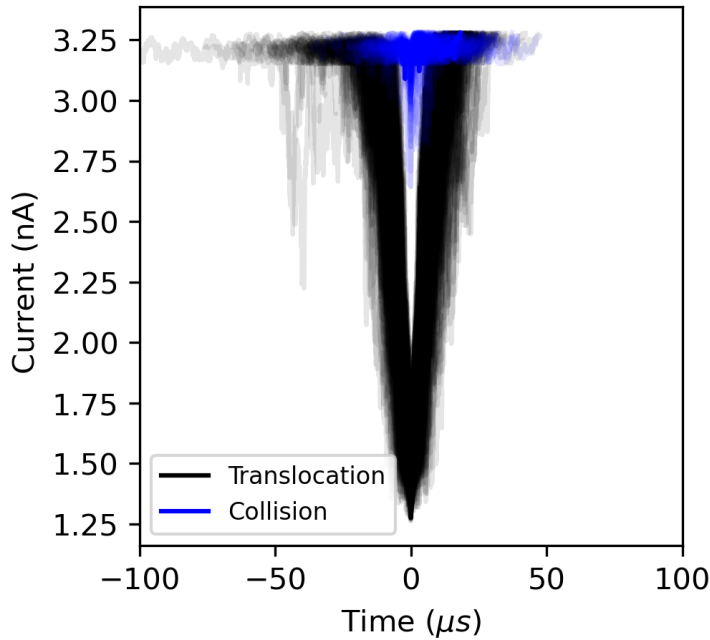
Figure 5.11: Current as a function of time for 100 overlapped events simulating nanoparticles with $d_{NP} = 40 \ nm$ and $\mu_{NP} = 0.8 \mu m \ cm/V \cdot s$. Full translocation events in black and collisions events in blue. The nanopore had dimensions of $d_P = L_P = 60 \ nm$.

of the amplifier(ROBINSON et al., 2018).

To connect the DMC simulations to experimental measurements and extract quantitative trends, each current trace was fit independently with a Gaussian function to obtain the relative blockade $\Delta i/i_0$ and dwell time τ. A representative translocation event and fit is shown in Figure 5.12. While many software packages such as OpenNanopore(RAILLON et al., 2012), EventPro(BANDARA et al., 2021), and PyPore use the cumulative sum algorithm (CUSUM) to call events and subsequently fit them, a Gaussian fit because of its simplicity and the similarity in shape to the simulated events. The event in Figure 5.12 is a relatively short event of $\tau \approx 10 \ \mu$s, with a blockade amplitude of $\Delta i \approx 1.75 \ nA$.

Figure 5.13 plots the relative blockade and dwell time obtained from Gaussian fits to the current traces for all values of particle diameter, pore length, and mobility simulated. In the top row, results for all events were overlayed, with the corresponding mean values and error from each configuration in the lower panels. The error was taken to be $\pm 2\sigma$, where σ is the standard deviation of the mean. Triangles, circles, and squares represent nanoparticles with diameters of $d_{NP} = 30$, 40, and 50 nm, respectively. The color of the points correspond to nanoparticle mobilities of $\mu_{NP} = 0.8 \ \mu m \ cm/V \cdot s$ (blue), $0.8 \ \mu m \ cm/V \cdot s$ (orange), and $1.2 \ \mu m \ cm/V \cdot s$ (green). The compiled results
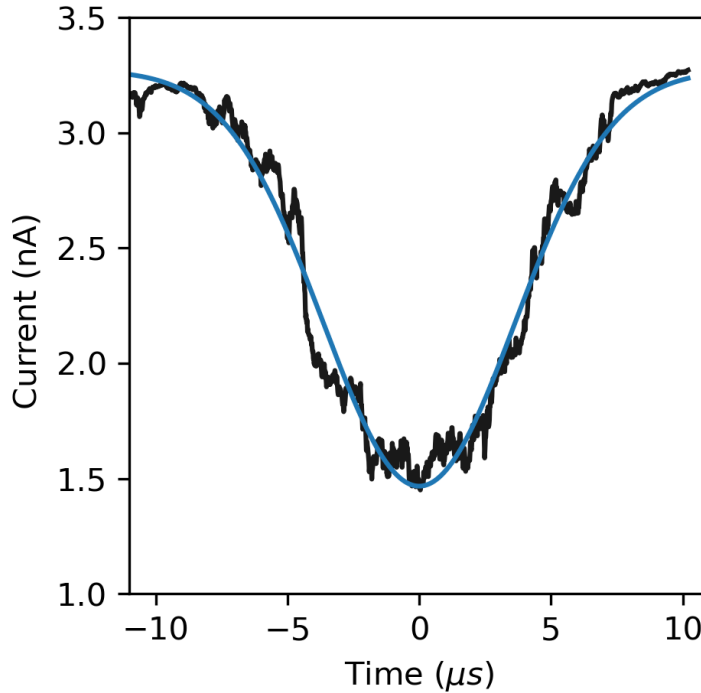
Figure 5.12: Representative current trace from a single translocation event of a $d_{NP} = 40$ nm nanoparticle with mobility of $\mu_{NP} = 0.8$ μm $cm/V \cdot s$. A Gaussian fit (blue line) was used to extract the dwell time and current blockade. The nanopore dimensions were $d_P = L_P = 60$ nm.

provide guidance on experimental conditions for successful translocation measurements of nanoparticles in a few ways. First, for each particle size, there exist three populations of points corresponding to the three values of nanoparticle mobilities. However, while the relative blockage each nanoparticle size is relatively constant (i.e., $\Delta i/i_0$ depends only on the size of the nanoparticle and not the mobility), there is overlap of the three populations of mobilities. This implies that for the values considered in this study, it may be difficult to resolve differences in nanoparticle mobilities by nanopore sensing alone. Regardless, the results show that as the mobility increases, the variability in τ decreases, presumably due to faster, more directed motion of the nanoparticle through the nanopore as electrophoresis overcomes Brownian motion. This trend can be more quantitatively observed in the lower panels, where the extent of the horizontal error bars decreases and the mean dwell time shifts to lower values as mobility increases. However, as the nanopore length increases from $L_P = 20$ nm to $L_P = 100$ nm, the variability in dwell time increases due to the increased path length over which the nanoparticle must diffuse.

In contrast to trends with respect to nanoparticle mobility, the DMC simulations show that nanopores sensing measurements can distinguish between nanoparticles with different sizes independent of their mobilities. For
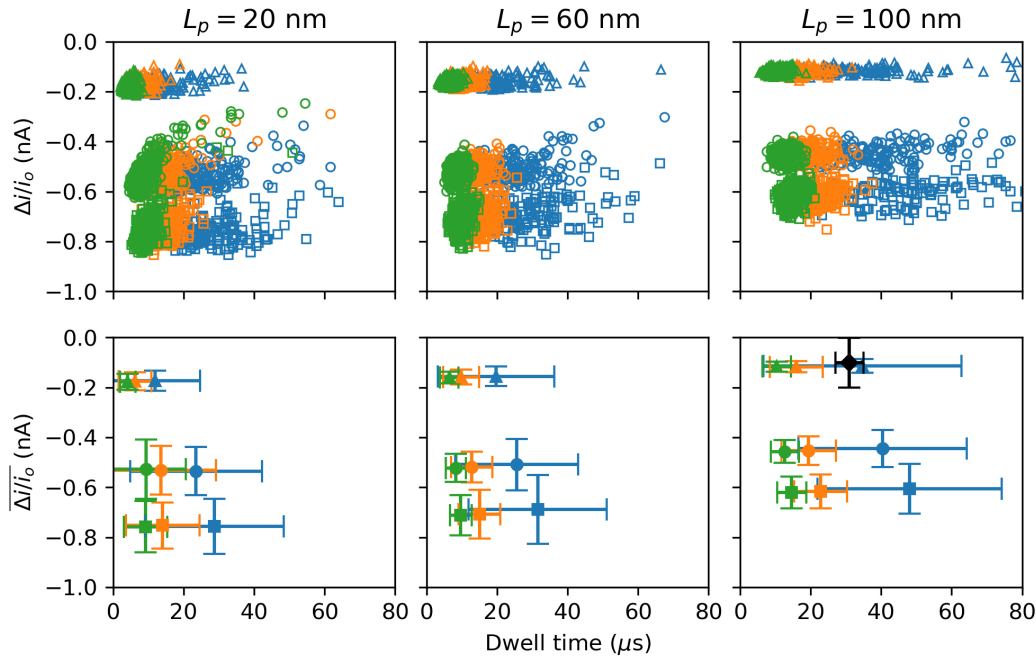
Figure 5.13: Summary of DMC simulation results for all nanoparticle and nanopore combinations. The top row plots the relative blockade versus dwell time for all events at a fixed nanopore diameter of $d_P = 60\ nm$ and nanopore length of (left to right) $L_P = 20\ nm$, $60\ nm$, and $100\ nm$. The lower row displays only the mean values. The symbol type designates nanoparticle diameters of $d_{NP} = 30\ nm$ (triangles), $40\ nm$ (circles), and $50\ nm$ (squares). Nanoparticle mobilities, designated by the symbol color, correspond to $\mu_{NP} = 0.4\ \mu m\, cm/V \cdot s$ (blue), $0.8\ \mu m\, cm/V \cdot s$ (orange) and $1.2\ \mu m\, cm/V \cdot s$. The black point in the lower right panel is from experimental measurements of $d_{NP} = 30\ nm$ Au nanoparticles translocating through a solid-state nanopore with $d_P = 80\ nm$ and $L_P = 100\ nm$. Error bars represent two standard deviations from the mean value.

the conditions studied here, the variability in the relative blockade is larger for the $d_{NP} > 30\ nm$ nanoparticles than for the $d_{NP} = 30\ nm$ particles, and that the variability slightly decreases as L_P increases. Thus, the optimal conditions for nanoparticle sensing should strike a balance between the higher resolution of the relative blockade that occurs for longer nanopores, and the larger translocation ratio that occurs as L_P decreases.

Finally, the simulations results were compared with the model derived on section 3. Using the equation 3-17, the expected relative blockade for $d_{NP} = 30$ nm, $40\ nm$, and $50\ nm$ nanoparticles, based solely on geometric effects, would be $\Delta i/i_0$ = -0.09, -0.24, and -0.49 , respectively, for $L_P = 60\ nm$. Comparing these values to the data in the lower row of Figure 5.13, the DMC simulations predict relative blockades that can vary significantly from those obtained from a purely geometrical estimate. For instance, for the smallest nanoparticles simulated ($d_{NP} = 30\ nm$), the relative blockade is smaller than the geometric
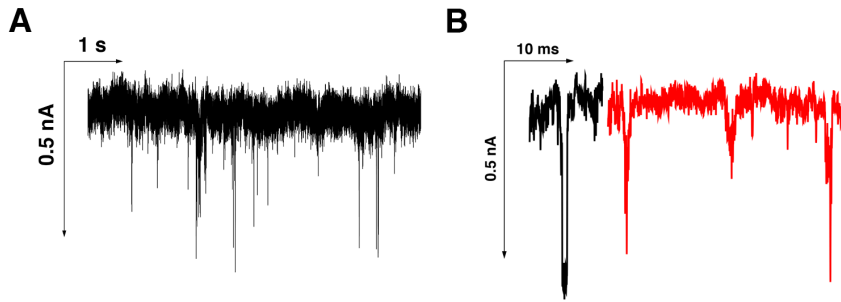
Figure 5.14: Experimental measurements of $d_{NP} = 30$ nm CTAB-coated Au nanoparticles. (a) Ionic current as a function of time over an interval of approximately 10 s. The large downward spikes in the current are translocation events which are roughly on the order of 0.5 nA. (b) Concatenated translocation and collision events extracted from two separate recordings (represented as black and red traces). Collision events can be observed as small pulses while true translocation events occur as large spikes.

estimate by approximately 50%. The reason for this discrepancy may lie with the fact that the PNP calculations which serve as the foundation for training the neural network take into account the manner in which the presence of a nanoparticle in the nanopore changes the electrostatic potential nearby the particle. The resolution of PNP simulations can also play a role on the observed discrepancy.

To assess whether the trends observed from the DMC simulations are representative of real translocation processes, were performed measurements to track Au nanosphere ($d_{NP} = 30$ nm) translocation. CTAB-coated Au nanospheres that were dispersed in a 500 mM KCl solution. Whereas citrate-coated Au nanoparticles can only disperse at concentrations of KCl up to about 10 mM, CTAB-coated nanoparticles can tolerate KCl concentrations up to at least 500 mM. Finally, to amplify the experimental signal, a bias of 200 mV, rather than 100 mV, was applied. However, since the translocation events were characterized by the *relative* blockade, this does not affect the comparison to simulations.

Shown in Figure 5.14 are (a) several seconds of ionic current measurements, showing resistive pulses that correspond to the translocation of $d_{NP} = 30$ nm nanoparticles through a nanopore ($d_P = 80$ nm, $L_P = 100$ nm) etched into a SiO_2-supported SiN_x membrane, and (b) selected translocation events shown at a magnified time scale. The final bandwidth of the measurement after applying a low-pass filter was 20 kHz. It is observed in Figure 5.14a that the translocation pulses are on the order of $\Delta i \approx 0.5$ nA. From the magnified data in Figure 5.14b, some of the events may be true translocation events, such as the one shown in black, but that translocation events appear

alongside what may be collisions, such as the short red pulses towards the right side of the red trace.

The current trace contained 164 events which were fit to a square profile to obtain the average dwell time $\tau = 31$ μs and $\Delta i/i_0 = -0.10$. Although the bandwidth of the measurements will lead to attenuation of events that occur for $\tau < 50$ μs, shorter events were not excluded and the average values are obtained from all events. This may lead to a slightly lower value for $\Delta i/i_0$ relative to the true value. However, since τ is close to the limit of 50 μs, this effect may be small. Figure 5.13 plots the experimental point as a black diamond in the lower right panel where good agreement between the predictions of τ and $\Delta i/i_0$ from the DMC simulations and the experimental measurements. Experimentally, the ratio $d_{NP}/d_P = 0.375$ whereas for DMC simulations of $d_{NP} = 30$ nm nanoparticles, $d_{NP}/d_P = 0.500$. Because of this, it is expected that the experimental value of $\Delta i/i_0$ should be slightly smaller than what was predicted from simulations due to the larger pore diameter used in the experiments. Although the uncertainty in the measurements prevents a definitive conclusion, the mean value obtained from experiments is slightly smaller than what was predicted from simulations, and that the average dwell time is in the range predicted. Thus, the results of DMC simulations are supported by the experimental measurements.

Figure 5.15, 5.16 and 5.17 show the overlaid current-time signals for full translocation in black, collisions in blue. Each figure shows the plots for the three values of particle diameter and three pore lengths for a given expected mobility. As expected, longer pores result in a smaller open current.
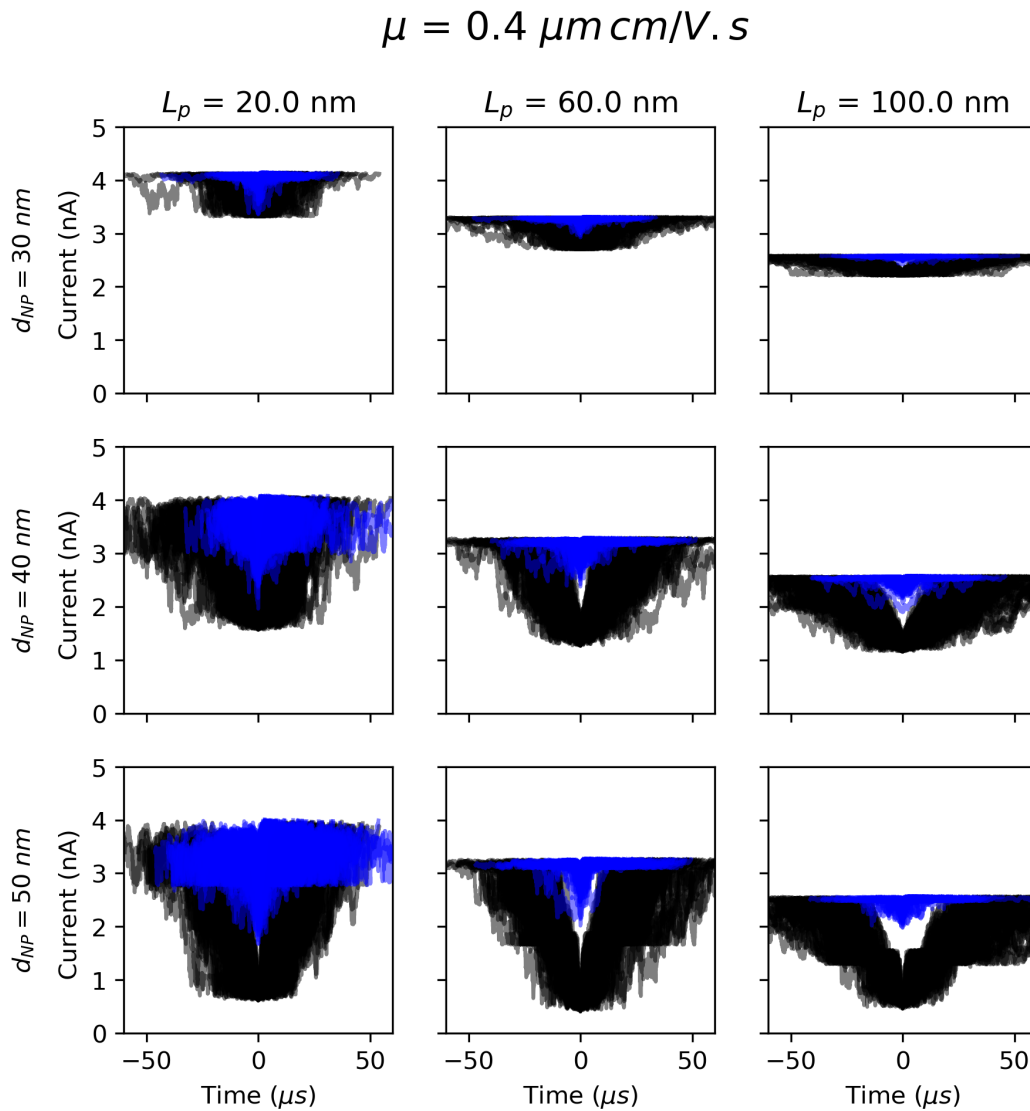
Figure 5.15: Current as a function of time for 100 overlapped events. Particle mobility of 0.4 $\mu m.cm/V.s$ and different conditions of particle diameter (rows) and pore length (columns). Full translocation events in black and collisions events in blue.
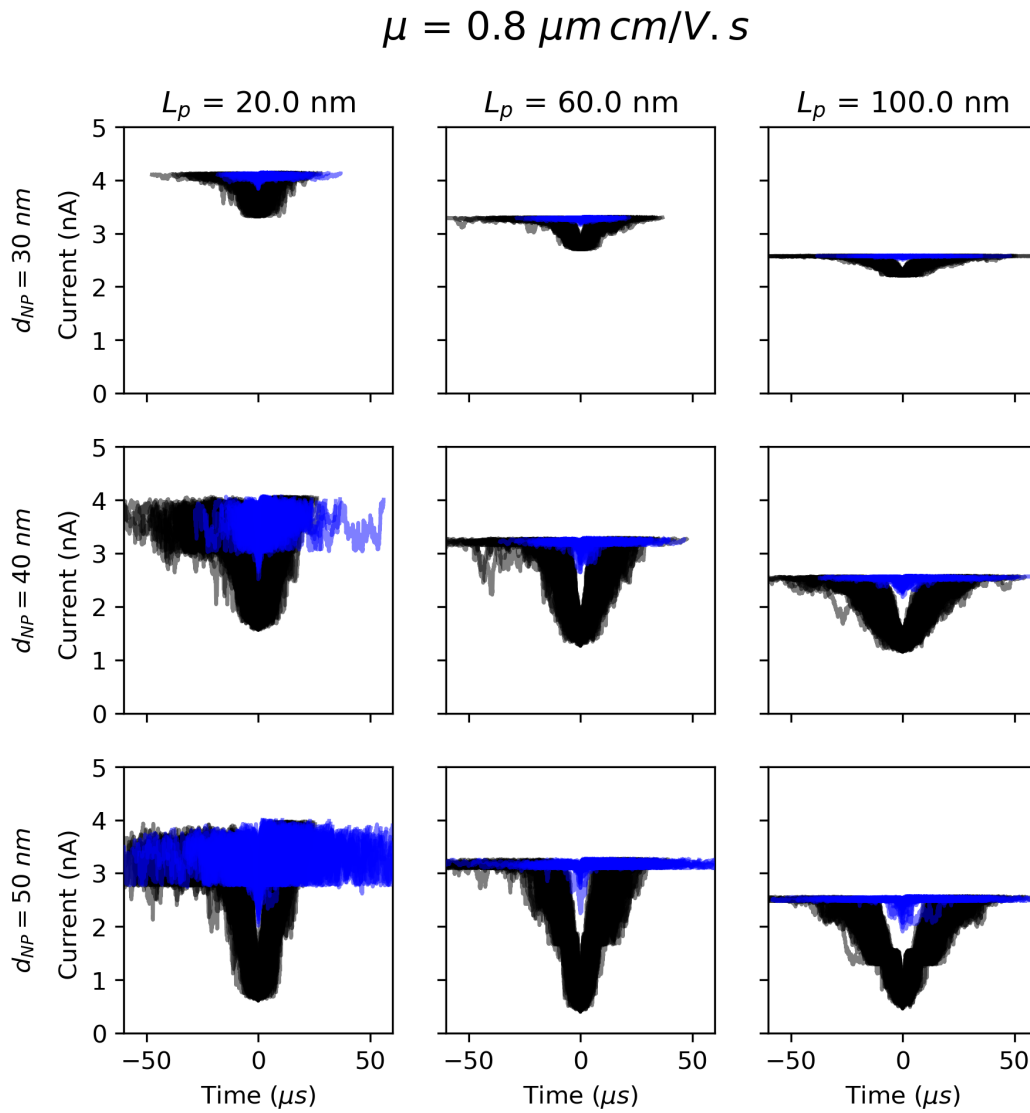
Figure 5.16: Current as a function of time for 100 overlapped events. Particle mobility of 0.8 $\mu m.cm/V.s$ and different conditions of particle diameter (rows) and pore length (columns). Full translocation events in black and collisions events in blue.
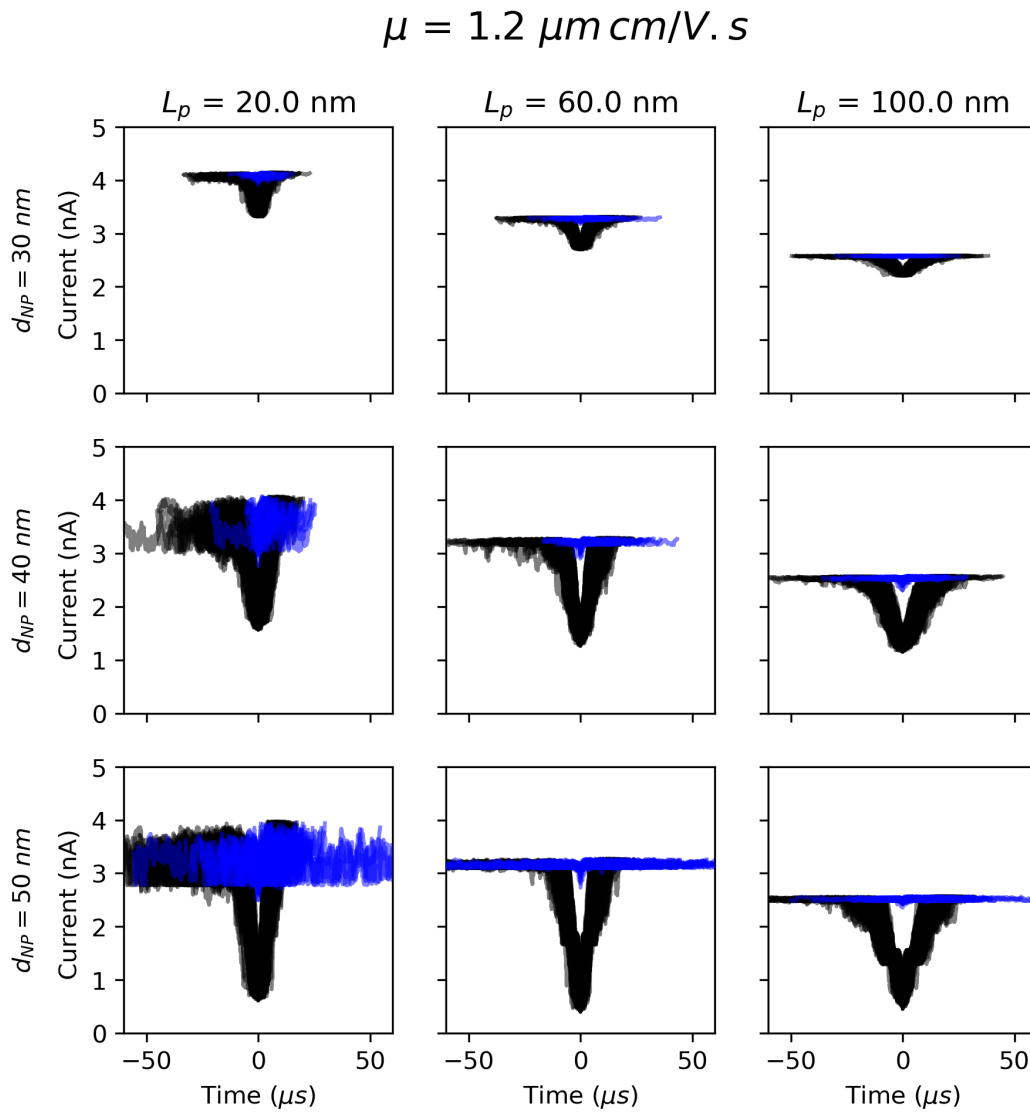
Figure 5.17: Current as a function of time for 100 overlapped events. Particle mobility of 1.2 $\mu m.cm/V.s$ and different conditions of particle diameter (rows) and pore length (columns). Full translocation events in black and collisions events in blue.

5.4
Summary

This chapter presented the simulation of the translocation of spherical particles by dynamic Monte Carlo.

PNP simulations were used to calculate the electrostatic potential around and inside the pore and the current associated with the particle position. The proposed Artificial Neural Network was able to capture the electrostatic potential profile calculated by PNP simulation, allowing the DMC code to efficiently simulate many particle trajectories.

The relative blockade and dwell time results from many trajectories of particles with different sizes and mobilities showed a significant overlap of the populations, indicating the existence of a limit of discrimination of particles of similar properties due to the effect of the Brownian motion.

6
Electrophoretic Motion of Unconfined Anisotropic Nanoparticles

6.1
Field Alignment of Nanorods

An electrostatic field can not only change the position of a charged anisotropic particle, but also its orientation. In each DMC step, there is a trial to change the orientation vector u to a new position $u + \delta u$. δu is formed by the sum of two random radial vectors $\delta v_i w_i$ as is shown in Figure 6.1. Therefore, the maximum possible change in orientation at each step is $90 \deg$. However, the size distribution of $\delta \vartheta$ also depends on the imposed diffusion coefficient and time step:

$$\delta \vartheta_{max} = \sqrt{2D_\vartheta \delta t} \tag{6-1}$$

For a maximum value of δu, both random weights $\hat{w}_1$ and $\hat{w}_2$ need to be at the maximum possible value (≈ 1). Therefore,

$$\delta \hat{u}_{max} = 1 \delta \vartheta_{max} \sqrt{2} \tag{6-2}$$

$$\begin{aligned}
\delta \theta_{max} &= \arctan(\delta \hat{u}_{max}/\hat{u}) \\
&= \arctan(\delta \vartheta_{max} \sqrt{2}) \\
&= \arctan(\sqrt{4D_\vartheta \delta t})
\end{aligned} \tag{6-3}$$
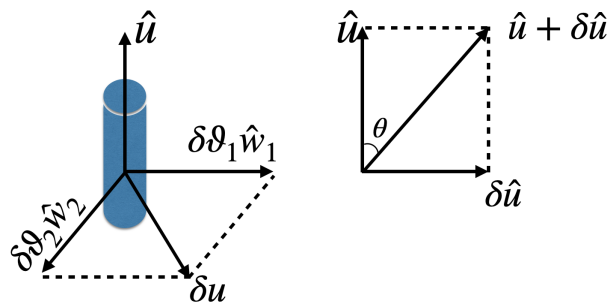
Figure 6.1: Graphical representation of the vectors involved in the changing in the particle orientation on DMC simulation.
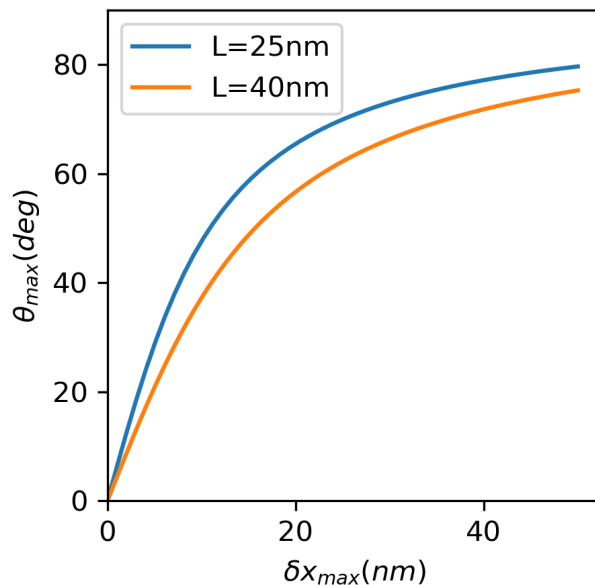
Figure 6.2: Maximum rotation in one DMC step as a function of the maximum displacement for particles with a diameter of 10 nm and lengths L=25 nm and L=40 nm.

Figure 6.2 shows the maximum rotation in one DMC step in function on the maximum displacement for particles with a diameter of 10 nm and two lengths. Longer particles have a smaller diffusion coefficient, therefore with slower rotation and smaller maximum rotation per DMC step. Both curves converge to 90deg for bigger maximum displacements (i.e., longer time-steps).

Figure 6.3 compares the prediction of the analysis above with the distribution of the change in orientation from a DMC simulation.

The trial change in orientation can promote a change in the particle potential, which is interrogated by the Metropolis scheme to accept or not the trial move. Considering a uniform charge density along the particle surface, the potential can be seen as the integration of the product of charge density and the local voltage at the surface.

$$\Psi = \int_S \sigma \, V \, dS \tag{6-4}$$

Numerical integration of the voltage over coordinates on the particle surface would results in a procedure too expensive. Therefore, it is important to develop analytical approximations

Using a Taylor expansion, the voltage at any point at the particle surface can be estimated by the voltage at the center of the particle and the local derivatives. Equation 6-5 shows the expansion up to the second term.

$$V = V_0 + \frac{\partial V}{\partial x_i} dx_i + \frac{\partial^2 V}{\partial x_i{}^2} \frac{dx_i{}^2}{2!} \tag{6-5}$$
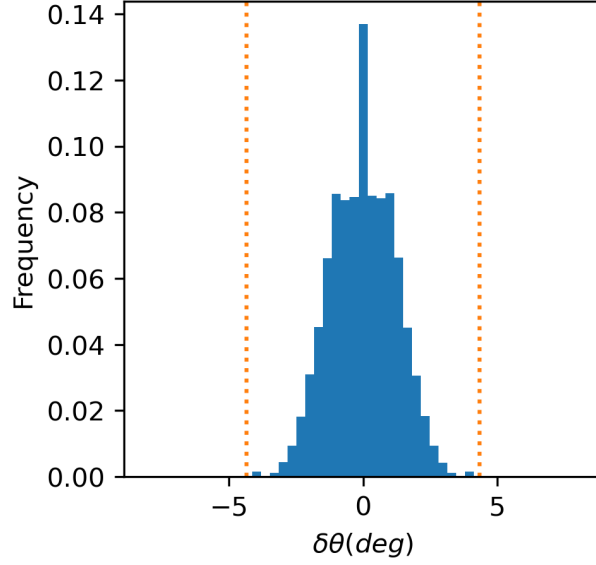
Figure 6.3: Distribution of the change in orientation for a million timesteps. Dotted vertical lines show the prediction for maximum change by Equation 6-3. Particles with a diameter of 10 nm and lengths L=25 nm and L=40 nm, the maximum change in position of 1 nm.

Using an open cylinder as a geometry approximation to perform the integration in cylindrical coordinates:

$$\Psi = \sigma \int_{S} \Big[V_0 + \frac{\partial V}{\partial x_{z_c}} dx_{z_c} + \frac{\partial V}{\partial x_{r_1}} dx_{r_1} + \frac{\partial V}{\partial x_{r_2}} dx_{r_2}$$
$$+ \frac{\partial^2 V}{\partial x_{z_c}{}^2} \frac{dx_{z_c}{}^2}{2} + \frac{\partial^2 V}{\partial x_{r_1}{}^2} \frac{dx_{r_1}{}^2}{2} + \frac{\partial^2 V}{\partial x_{r_2}{}^2} \frac{dx_{r_2}{}^2}{2} \Big] dS \tag{6-6}$$

$$\Psi = A + B + C + D + E + F + G \tag{6-7}$$

$$A = \sigma \int_0^{2\pi} \int_{-L/2}^{L/2} V_o\, R\, dz\, d\theta = \sigma 2\pi RLV_0 = q_{eff} V_0 \tag{6-8}$$

$$B = \sigma \int_0^{2\pi} \int_{-L/2}^{L/2} \frac{\partial V}{\partial x_{z_c}} dx_{z_c}\, R\, dz\, d\theta = 0 \tag{6-9}$$

$$C = \sigma \int_0^{2\pi} \int_{-L/2}^{L/2} \frac{\partial V}{\partial x_{r_1}} dx_{r_1}\, R\, dz\, d\theta = \sigma\, L \int_0^{2\pi} \frac{\partial V}{\partial x_{r_1}} (R\cos\theta) = 0 \tag{6-10}$$

$$D = \sigma \int_0^{2\pi} \int_{-L/2}^{L/2} \frac{\partial V}{\partial x_{r_2}} dx_{r_2}\, R\, dz\, d\theta = \sigma\, L \int_0^{2\pi} \frac{\partial V}{\partial x_{r_2}} (R\sin\theta) = 0 \tag{6-11}$$

$$E = \sigma \int_0^{2\pi} \int_{-L/2}^{L/2} \frac{\partial^2 V}{\partial x_{zc}^2} \frac{dx_{zc}^2}{2} R\,dz\,d\theta = q_{eff}\frac{L^2}{24}\frac{\partial^2 V}{\partial x_{zc}^2} \tag{6-12}$$

$$F = \sigma \int_0^{2\pi} \int_{-L/2}^{L/2} \frac{\partial^2 V}{\partial x_{r1}^2} \frac{dx_{r1}^2}{2} R\,dz\,d\theta = q_{eff}\frac{R^2}{4}\frac{\partial^2 V}{\partial x_{r1}^2} \tag{6-13}$$

$$G = \sigma \int_0^{2\pi} \int_{-L/2}^{L/2} \frac{\partial^2 V}{\partial x_{r2}^2} \frac{dx_{r2}^2}{2} R\,dz\,d\theta = q_{eff}\frac{R^2}{4}\frac{\partial^2 V}{\partial x_{r2}^2} \tag{6-14}$$

By the symmetry of a cylindrical geometry, only the second order derivatives of the potential (the first derivative of the electrical field) have non-null values:

$$\Psi = q_{eff}\left\{ V_o + \frac{L^2}{24}\frac{\partial^2 V}{\partial z_c^2} + \left[\frac{R^2}{4}\left(\frac{\partial^2 V}{\partial r_1^2} + \frac{\partial^2 V}{\partial r_2^2}\right)\right]\right\} \tag{6-15}$$

To check how strongly the field can influence the particle orientation, the mean orientation of a particle over a particular field can be calculated. Due to the assumed particle symmetry, it is not of importance which end of the particle is aligned to a particular direction. Therefore, a squared cosine relation can be used to analyze the particle mean orientation. A random distribution results in a mean $\cos^2$ of $1/3$. The orientation factor Θ shown in equation 6-16 gives a modified dependence on the orientation, with $\Theta = 1$ for completely aligned particles, $\Theta = 0$ for totally random configuration and $\Theta = -0.5$ for particles completely perpendicular to the direction of the field gradient.

$$\Theta = \frac{1}{2}[\,3\langle\cos^2\theta\rangle - 1] \tag{6-16}$$

Finally, to check the DMC algorithm, simulations were done with stationary particles (updating only the orientation) and using analytical expressions for the electrostatic potential. Two equations were used. Equation 6-17 is a pure quadratic equation with the second-order derivative equals to the term V''. The Equation 6-18 is a polynomial with a second-order derivative depending on the parameter n, but also has first and other high order derivatives.

$$V = V_o + \frac{V''}{2}(x - x_o)^2 \tag{6-17}$$

$$V = V_o \left(\frac{x}{x_o}\right)^n \tag{6-18}$$

Figure 6.4 shows the results of electrostatic potential given by the analytical functions using different values of their scaling parameters.

The simulations were done with 100 runs with particles initially randomly orientated, positioned at $x = 100\ nm$, with a diameter of 10 nm, length of 40 nm, and $\delta t \approx 8$ ns. The results of the orientation factor for simulations
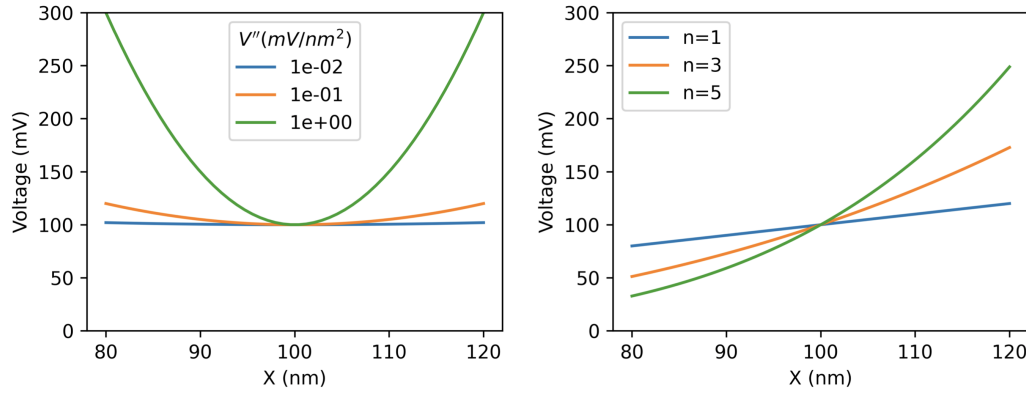
Figure 6.4: Electrostatic potential given by the analytical functions of Equation 6-17 (left) and Equation 6-18 (right).
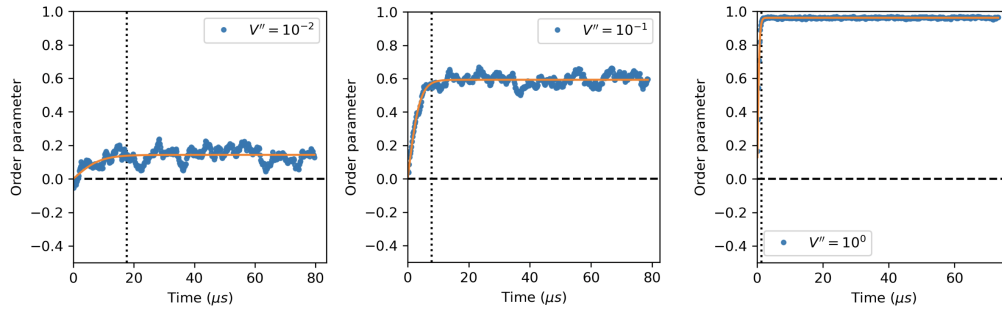
Figure 6.5: Orientation factor as a function of time for voltage following the Equation 6-17. The continuous line represents the fit of the Equation 6-19, and the fitted parameter t_c is indicated by a vertical dotted line.

using the equations and parameters above are shown in Figure 6.5 for voltage following the pure quadratic equation (6-17) and 6.6 for voltage following the pure quadratic equation (6-18)

Equation 6-19 was adjusted to model the data. The choice of a hyperbolic tangent was made based solely on the shape of the function, as it can capture the transient nature of the mean orientation. The parameter Θ_∞ can be related to the terminal mean orientation, and the parameter t_c can be seen as a critical time after that the mean orientation becomes practically constant. With an increase of the second-order derivative (higher V'' and n), the ensemble of particles averages with greater alignment and shorter critical times. One exception to the trend on critical time is the one in the left panel, polynomial with $n = 1$. As the voltage has a nulls second- and higher-order derivative, the mean orientation should stay totally random. It seems that this deviation is just a sampling effect due to the number of runs and time steps.

$$\Theta_{fit} = \Theta_\infty \tanh\left(\frac{t}{0.5\, t_c}\right) \qquad (6\text{-}19)$$
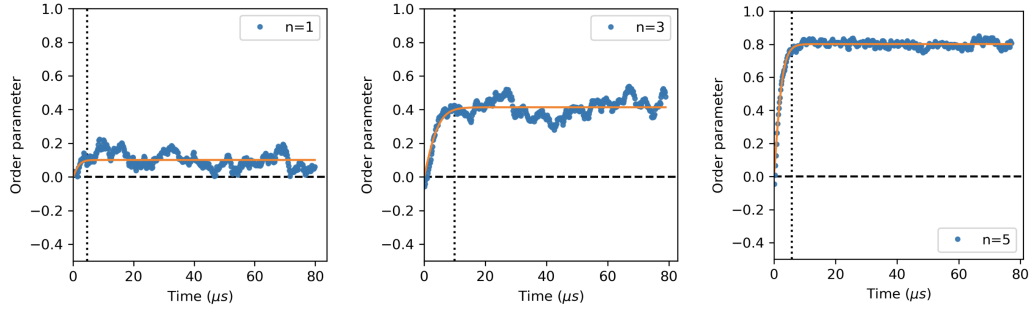
Figure 6.6: Orientation factor as a function of time using the pure quadratic function (Equation 6-18). The continuous line represents the fit of the Equation 6-19, and the fitted parameter t_c is indicated by a vertical dotted line.

From the Metropolis accepting criteria (eq. 2-6), the expected average orientation can be calculated (QIAO; SLATER, 2020):

$$\langle \cos^2 \theta \rangle = \frac{\int_0^\pi \cos^2 \theta \, \sin \theta (-\exp \delta\Psi/k_bT)d\theta}{\int_0^\pi \sin \theta \exp(-\delta\Psi/k_bT)d\theta} \tag{6-20}$$

where $\delta\Psi$ is the difference between potential of the particle aligned to the field gradient ($\Psi_{\theta||}$) and the particle potential at a particular orientation (Ψ_θ):

$$\delta\Psi = \Psi_{\theta||} - \Psi_\theta \tag{6-21}$$

Figure 6.7 shows the comparison between the Θ_∞ results from simulations (markers) and the model (continuous line) from equations 6-20 and 6-16 using the potential following the second-order approximation of Equation 6-15. There are two situations when the agreement is less pronounced: One is from the simulation using the voltage as a polynomial function with $n = 5$. In this case, the high-order derivatives can lead to an important contribution to the field values, and the truncation of Taylor expansion can be insufficient. The other situation is related to the points at lower or null second-order derivatives, which are more prone to errors in the estimation of the order parameter from the simulations due to the larger fluctuation in the results. Nonetheless, in overall the results from the simulation agree considerably with the model, indicating that the DMC code is working as expected and the second-order approximation seems to be a good strategy to avoid direct numeric integration of the electrostatic potential along the particle surface.

Figure 6.8 shows the results of the second derivative of the electrostatic potential in relation to the axial direction of the pore. Based on the values from the PNP simulation, it is not expected a strong alignment of the rod particles during the translocation under the conditions specified for this study.
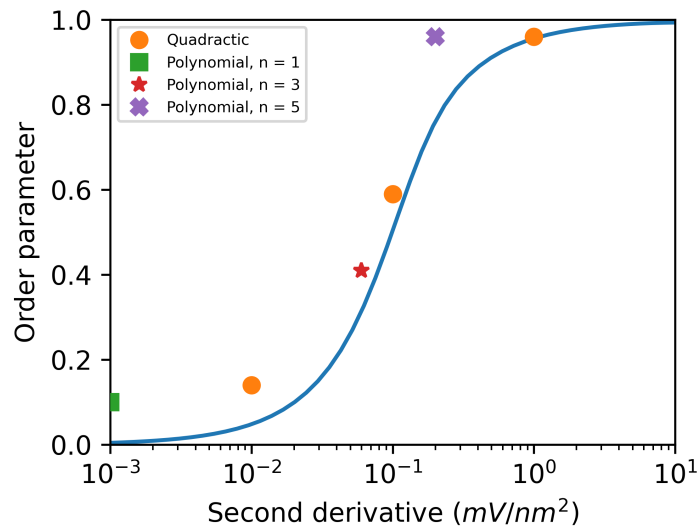
Figure 6.7: Order parameter as a function of the second derivative of the electrostatic potential. Equation with $n = 1$ actually has a null second-order derivative, but the result was included in the lower limit to allow comparison.
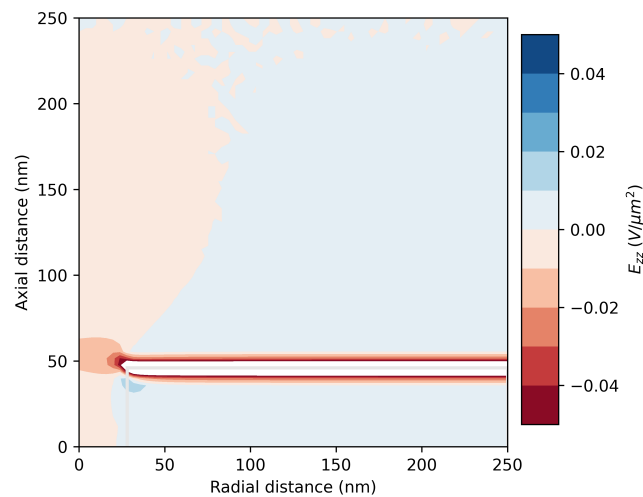
Figure 6.8: The second derivative of the electrostatic potential in relation to the pore axial direction (E_{zz}), truncated to $\pm 0.05 \ V/nm^2$. Most of the voltage decay occurs at the membrane surface outside the pore, which appears in white and has values greater than the truncation limit.
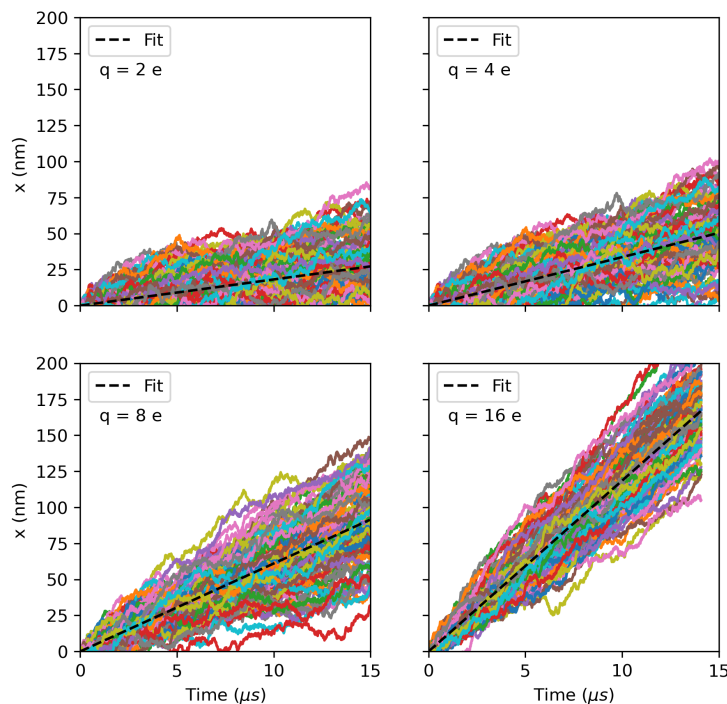
Figure 6.9: Position as a function of time for 100 trajectories at different values of effective charge q. The dotted black line indicates a linear equation adjusted to the data. $d_{rod} = 10\ nm$, $L_{rod} = 40$ nm.

6.2
Diffusion and Mobility of Nanorods

As with the case of spherical particles, it is important to correctly set the effective charge used in DMC simulations in order to capture the correct values of electrophoretic mobility without losing the correct Brownian motion. DMC simulations were done under a constant field along the x-direction ($E_x = 0.1\ mV/nm$), without any components in the Y and Z directions. Figure 6.9 shows the displacement in the x-direction as a function of time for 100 runs for nanorods with length of 40 nm and diameter of 10 nm. Each panel represents a set of simulations with a value of the effective charge. As expected, higher charge results in higher velocities, and the mean value seems to be well captured by a linear relation.

Figure 6.10 summarizes the mobilities extracted from the simulations shown in Figure 6.9 and compares with the model of effective charge of Equation 6-22, based on the Hückle approximation (QIAO; SLATER, 2020). The results seem to deviate to the linear relationship from Equation 6-22 in high values of charge, but are in close agreement in the range of interest.

$$q_{eff} = \frac{k_b T\ \mu}{D} \tag{6-22}$$

Once there is no change in voltage in the directions x and y, we expect a
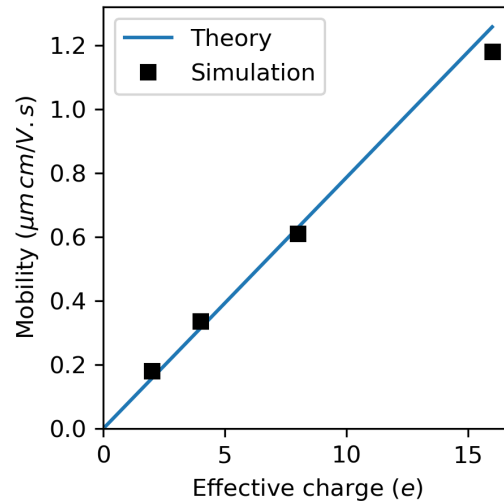
Figure 6.10:   Mobility as a function of effective charge. Squared markers are obtained from DMC simulations, and the continuous line from Equation 6-22. $d_{rod} = 10 \ nm$, $L_{rod} = 40$ nm.

pure Brownian behavior for the displacements in these directions, as is shown in Figure 6.11. The small deviations on the calculated diffusion coefficient from the input value, 22.7 $\mu m^2/s$, can be related to the finite sampling, since is not correlated with the field strength.
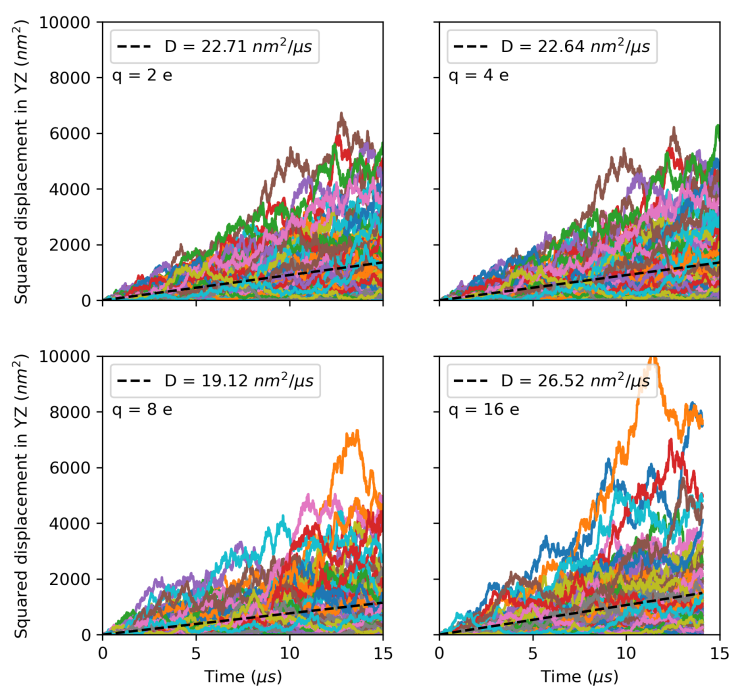
Figure 6.11: Squared displacement (in y and z directions) as a function of time for 100 particles trajectories. Dashed line indicates the MSD, from which the diffusion constant D was calculated. Expect D of $22.7\,nm^2/\mu s = \mu m^2/s$.

6.3
Summary

This chapter showed the simulation by dynamic Monte Carlo of unconfined rod nanoparticles.

A model for the potential energy of the particle as a function of the particle orientation and the local derivatives of the electrostatic potential was derived. Model and simulations show the alignment of a nanorod is not directly affected by the first derivative of the voltage, but mainly by the mean value at the particle center and the second derivatives of the voltage at the center point.

A simplified expression to predict the mobility as a function of effective charge, based on the Hückle approximation, resulted in a good agreement with the simulations in a uniform field.

7
Translocation Simulations of Anisotropic Nanoparticles

7.1
Modeling the Electrostatic Potential and Current in a Nanopore by PNP

7.1.1
Effect of a Nanorod

With anisotropic particles such as nanorods, orientation of the particle becomes another factor that can affect the current response of the pore. Figure 7.1 plots the relationship between the current as a function of the polar angle for a rod-shaped particle at the entrance of the pore and aligned with the pore axis. The current drops slightly with the angle until the particle becomes perpendicular to the pore axis. The results are symmetric in $\theta = 0$deg and 90deg, as expected due to the particle symmetry.
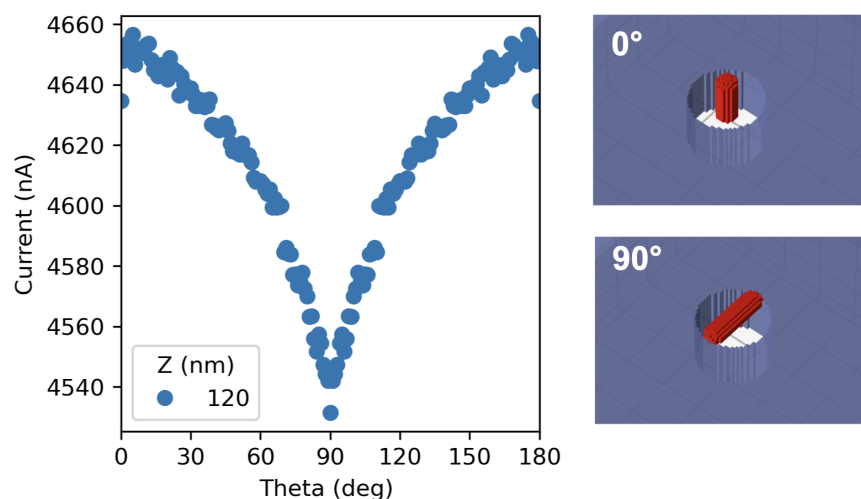
Figure 7.1: Current as a function of the polar angle for a particle at the entrance of the pore. In the right panels is a representation of the geometries of the particles (red) and the membrane (blue) under the resolution used in the simulations.
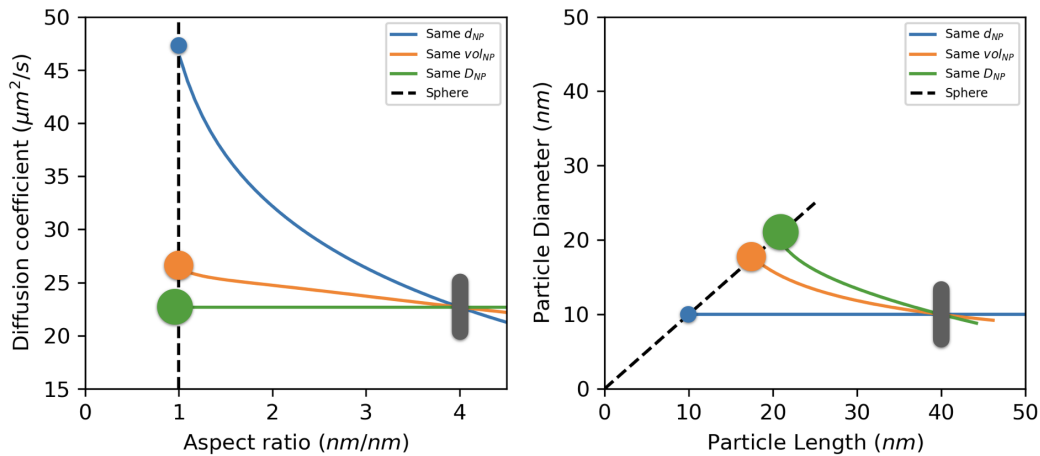
Figure 7.2: Particle properties comparable to a 10×40 nm nanorod. On the left, the diffusion coefficient is plotted as a function of the aspect ratio of the particles; on the right, diameter and length. Geometrical representation overlaid with the plot for spheres and the 10 x 40 nm rod.

7.2
Translocation of Nanorods

7.2.1
Comparison with Nanospheres

To evaluate this, first it is necessary to reflect on what spherical particle would be fairly comparable to a specific nanorod in terms of the dimensions of the particles.

To exemplify this analysis, Figure 7.2 shows a comparison between a rod particle with diameter of 10 nm and length of 40 nm and three spherical particles: one with same diameter ($d_{NP} = 10$ nm), one with same volume ($d_{NP} \approx 18$ nm) and one with same diffusion coefficient ($d_{NP} \approx 22$ nm), predicted by the Stokes-Einstein relation (Equation 2.3.0.1).

Spherical particles with the same diameter of the nanorod have more pronounced blockade and we expect a larger variation in the data due to a larger diffusion coefficient. To have relatively similar current blockades, the volumes of both nanorod and nanosphere have to be similar. The elongated shape of the nanorod results in a larger drag even compared to a spherical particle of the same volume, therefore, a spherical particle needs to have a larger volume than the rod to match its diffusion coefficient.

Regarding the dwell time, the electrophoretic mobility results from the competition between the electrostatic force and the retardation force (e.g.,

Table 7.1: Electropheretic properties as a function of nanoparticles geometries.

d_{NP} (nm)	L_{NP} (nm)	V_{NP} (nm³)	D_{NP} (μm²/s)	A_{NP} (nm²)	σ_{NP} (mC/m²)	q_{NP} (e)	μ_{NP} (μm cm/V.s)
10.0	40.0	2879.8	22.7	1256.6	13.6	106.8	1.20
10.0	10.0	523.6	49.0	314.2	13.6	26.7	1.13
17.7	17.7	2879.8	27.8	978.9	13.6	83.2	1.22
21.6	21.6	5283.6	22.7	1467.0	13.6	124.7	1.25
10.0	40.0	2879.8	22.7	1256.6	13.6	106.8	1.20
10.0	10.0	523.6	49.0	314.2	14.4	28.4	1.20
17.7	17.7	2879.8	27.8	978.9	13.4	82.1	1.20
21.6	21.6	5283.6	22.7	1467.0	13.1	120.0	1.20

friction from the solvent). Particles of the same material at a given salt concentration often have about the same surface charge density independently of the geometry, although it is known that curvature can affect the surface charge density on grafted nanoparticles. Keeping the assumption of constant surface charge density, the differences in geometry from rods to spherical particles have two effects: on the surface area, leading to distinct values of total charge and therefore the electrophoretic force, and on the viscous drag, leading to different levels of retardation force.

However, if the surface charge density can be set independently to compensate for the changes in the surface area, particles with the same volume or same diffusion coefficient and same mobility can exist. In this case, the differences in the current traces between rods and spheres would depend mostly on the differences in the trajectories, rotations, and interactions with the membrane.

Table 7.1 shows the comparison of a nanorod and spherical nanoparticles with geometries as discussed earlier using the equations 1-6, 1-9, 1-11 and 1-12 presented in the chapter 1. Assuming constant surface charge density, the sphere with the same volume of the nanorod presented a close value of mobility, as the lower drag compensates for the smaller surface area. In the case of the sphere with the same diffusion coefficient, an overcompensation due to the larger surface area leads to higher mobility than the rod. In the case of constant mobility, the surface charge density has to be reduced accordingly.

Next, DMC simulations with parameters taken from the last four lines of table 7.1 were performed, setting the effective charge to impose the same electrophoretic mobility for all particles. Figure 7.3 shows the current traces from these simulations. The pulses from the rod particles (panel A) look sharper than the ones from spherical particles (panels B, C, and D), which have a more Gaussian shape.
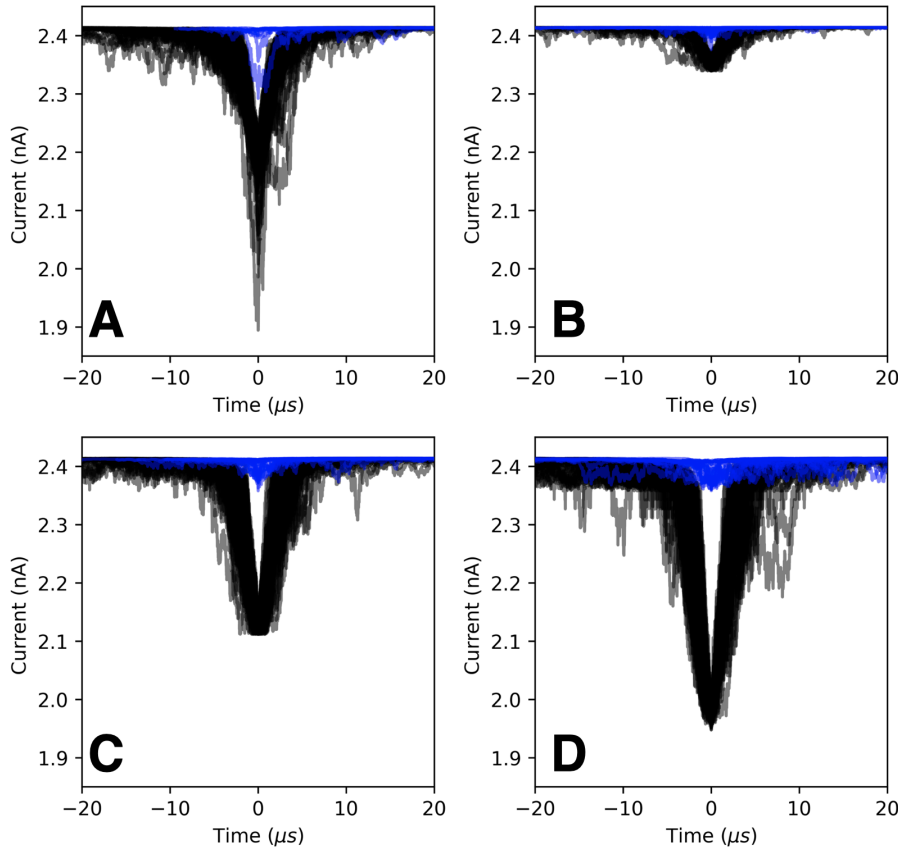
Figure 7.3: Results of DMC simulations of ionic current as a function of time. **A**: Rod with $d_{rod} = 10$ nm and $L_{rod} = 40nm$; **B**: Sphere with $d_{NP} = 10$ nm; **C**: Sphere with $d_{NP} = 18$ nm; **D**: Sphere with $d_{NP} = 22$ nm. $\mu_{NP} = 1.2$ μm cm/V.s, $d_P = 30$ nm, $L_P = 40$ nm, [KCl] $= 0.100$ mol/L, V $= 0.100$ V, 100 runs for each geometry.

Figure 7.4 summarizes the values of the relative blockade and dwell time for each trajectory and the mean values for each particle geometry. As expected, the mean dwell time for all particles is very close, as the result of imposing the same mobility. The slightly shorter mean time for the smaller particle can be a reflection of less steric impediments during the entrance and translocation, but the tendency lacks statistical significance. The smaller particles also have higher dispersion in the results of dwell time, reflecting the effect of their diffusion coefficient. Also as expected, the sphere with the same volume has closer values of relative blockade compared to the rod. The rod particles have higher dispersion in the relative blockade than the sphere of the same volume, indicating the effect of the orientation of the particle on the current signal.
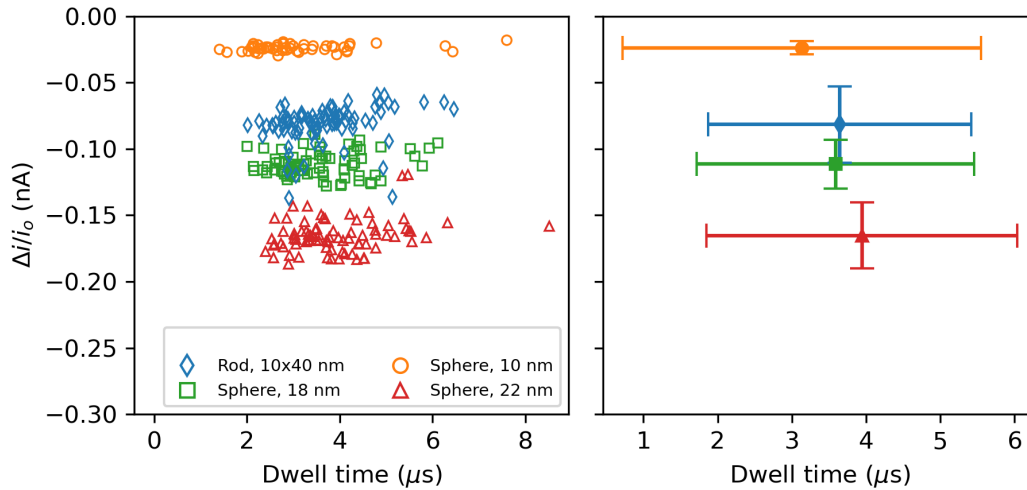
Figure 7.4: Relative blockade versus dwell time from the results presented in the Figure 7.3. Left: individual values only from the translocation events; right: Mean values for each particle geometry, error bars denote limits of 2 standard deviation.

7.2.2
Nanorod Orientation During Translocation

Often the literature reports the alignment of rod particles prior to the entrance of the pore, a result of the influence of the electrical field (QIAO; SLATER, 2020; AI; QIAN, 2011). However, these reports were done in the context of the translocation of DNA segments, with smaller and much more charged particles. Here, the orientation of a 10 nm x 40 nm nanorod was monitored when simulating the translocation through a pore with a diameter of 20 nm, as Figure 7.5 shows. The smaller pore diameter ensures the orientation of the rod when inside the pore. However, not only is such pre-alignment is not visible, but rod particles tend to align perpendicular to the pore axis when approaching the pore, characterized by the sudden decrease in the order parameter between $Z = 150$ nm and $Z = 180$ nm.

Observing tracking of individual trajectories, such as the one shown in Figure 7.6, the "anti-alignment" of the rod seems to be caused by the steric restriction of the rod rotation when approaching the pore membrane. Comparing the current (upper panel) and orientation (lower panel) in time, we did not observe any signs of the anti-alignment within the current signal.
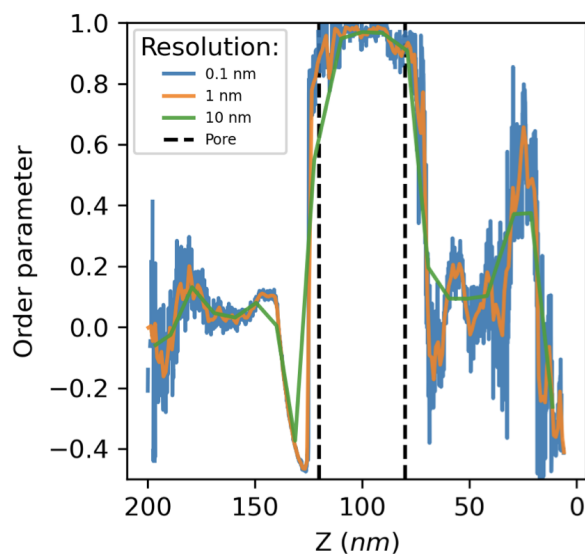
Figure 7.5: Orientational order parameter as a function of the height of the particle in the system. Dotted lines indicate the position of the pore. Each curve represents a bin size in height where the polar angle was averaged, according to the values shown in the legend.
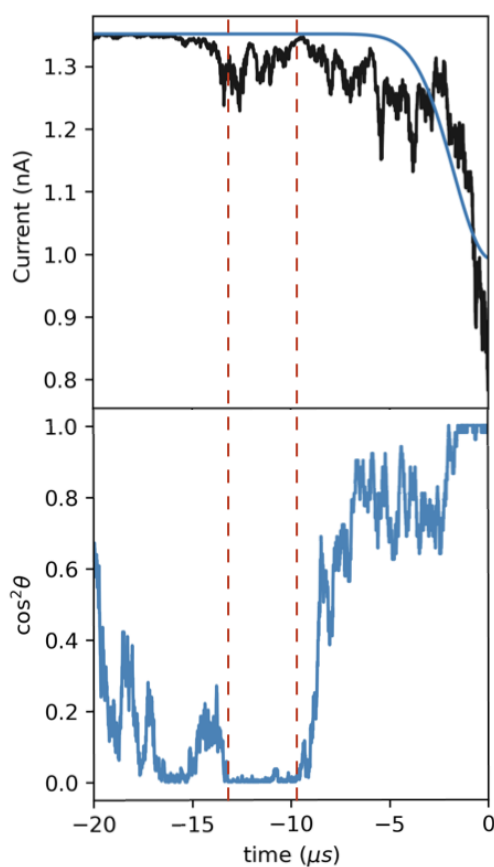
Figure 7.6: Current (upper panel) and squared polar angle (lower panel) for one particle trajectory. No influence of the nanorod orientation on the ionic current was observed.

7.3
Summary

This chapter presented dynamic Monte Carlo simulations of rod nanoparticles translocating a nanopore.

Comparing the results of relative blockade of nanorods and nanospheres of same diameter, volume or diffusion coefficient, the spheere of same volume of showed the closer values to ones obtained with the rods. However, the shape of the current traces appears to reflect the differences in the geometry of the particles, with sharper pulses for the rods.

Contrary to literature reports on alignment of small rod particles prior to the entrance of the pore as a result of the influence of the electrical field, simulations with larger particles with properties related to gold nanorods shows no prior alignment, with the particles even tumbling in a perpendicular direction due to collisions with the membrane surface.

8
Summary and Future Work

The present research aimed to expand the analytical and simulation tools to study the translocation of nanoparticles and the application of such process as a characterization tool, the nanopore sensing. The techniques developed as part of this work have allowed new approaches to simulating translocation measurements that provide new information to experimental researchers.

The first chapter introduced the fundamental aspects of nanoparticle motion in the nanopore, pointing to an extensive collection of literature about the technology, application, and simulation of nanopore sensing.

Chapter 3 presented simple analytical models for predicting the characteristic current in nanopores. In this chapter, some models available in the literature were revisited and new models for spherical and rod particles were proposed. The phenomenon of current *increasing* by the presence of a charged particle inside the pore at low salt concentration was also discussed. Although general trends from the models are supported by the experimental results, such as the crossover to conductive pulses with the decrease of the salt concentration and the appearance of conductive pulses concentrated with intermediate values of the ratio between particle diameter and pore diameter, a quantitative agreement with the obtained experimental results and with other examples in the literature was not observed. This topic remains to be further explored.

The simulation of unconfined spherical particles in a uniform electrostatic field was presented in Chapter 4. The results confirmed the correct modeling of Brownian and electrophoretic motion by dynamic Monte Carlo (DMC) simulations. An analytical expression for the expected mobility was also derived, based on arguments from the Metropolis algorithm and the time scaling of DMC simulations. The analytical model provided an accurate means to scale the effective charge of the particle to obtain the correct electrophoretic mobility.

Chapter 5 proceeded with the study of the translocation of spherical particles. The proposed Artificial Neural Network was able to capture the voltage profile around and inside the pore calculated by PNP. The prediction performance of the neural network was also investigated, depending on the architecture of the model. The strategy of employing a neural network was

found successful in quickly estimating the potential depending on the particle position, allowing the simulation of many trajectories. The relative blockade and dwell time results from many trajectories of particles with different sizes and mobilities showed a significant overlap of the populations, indicating the existence of a limit of discrimination of particles of similar properties, coming from the effect of Brownian motion. Longer pores, although promoting more scattering in the results of dwell time, enhanced the differences in the mean value, with the net effect of helping the discrimination of the particles of similar size and different values of mobility. Longer pores, on the other hand, *reduced* the variability of the values of the relative blockade, also helping the discrimination of particles with distinct sizes.

Chapter 6 expanded the simulation tool to study the motion of anisotropic particles. A model derived from the DMC expressions and simulations using analytical expressions for the voltage has shown that the alignment of a nanorod is not directly affected by the first derivative of the voltage, but mainly by the mean value at the particle center and the second derivatives of the voltage at the center point. With the use of Hückle approximation, a simplified expression to predict the mobility as a function of effective charge resulted in a good agreement with the simulations in a uniform field.

Finally, Chapter 7 presented the simulation of the translocation of nanorods. The results of the relative blockade of a nanorod and spheres with electrophoretic mobility, the sphere with same volume presented close mean values to the rod compared to the spheres with same diameter or same diffusion coefficient. However, the shape of the current traces appears to reflect the differences in the geometry of the particles, with sharper pulses for the rods.

8.1
Future Work

Much remains to be done in the development of accurate modeling and simulation of nanoparticle translocation. Here, suggestions for future work are presented, either to attack the current limitations of this study or to provide further development based on the present findings.

8.1.0.1
Charged Surfaces and Explicit Fluid

In the present study, the fluid flow is not explicitly modeled, which neglects the effect of hydrodynamic interactions that can hinder both Brownian and electrophoretic motion. Also, the membrane and particle surface during the PNP calculations were left uncharged, which in conjunction with the lack

of hydrodynamics, neglects the effect of electro-osmotic flow. The main reason for these choices came from the limitation in the resolution attainable by the PNP simulation. The use of multi-physics software (TSUTSUI et al., 2019; MITSCHA-BAUDE et al., 2017) with adaptive meshing can address these limitations.

8.1.0.2
DMC versus Langevin Dynamics

Another way to explore the hindering of diffusion and electrophoresis is the use of explicit-fluid Langevin Dynamics simulations, such as Dissipative Particle Dynamics. Although the computational cost would be prohibitive to simulate hundreds of trajectories as it was done here with DMC simulations, this study would be useful to validate or improve upon the results obtained here. Additionally, implicit fluid Langevin Dynamics could be used as an alternative to DMC simulations with comparable computational effort.

8.1.0.3
Voltage Modeling by Artificial Neural Networks

At the level of simplifications in this study, the mapping of the electrostatic potential into the DMC code by a neural network was not more advantageous than the mapping by linear interpolation. However, the machine learning approach has the potential to be much further developed considering the recent growth of the field. For instance, the network architecture could be greatly improved by hyperparameter optimization(YANG; SHAMI, 2020), allowing better prediction of the potential with the same computational cost. Classes of neural networks other than MPLs can also be investigated. A highly promising approach seems to be the use of Physics-Informed Machine Learning (BEUCLER et al., 2021; KARNIADAKIS et al., 2021; RAISSI; PERDIKARIS; KARNIADAKIS, 2019). In this approach, physical constraints are applied to the network training, with recent work achieving great generalization from small data sets.

8.1.0.4
Conductive Pulses

The analytical models developed in this study could not quantitatively match the experimental results for the case of conductive pulses. A combined analytical and numerical study, with the charged surface and explicit fluid modeling as suggested before, can shed light on this still not well-understood phenomenon.

8.1.0.5
Grafted Particles

Grafted nanoparticles are important nanoengineered materials that present challenges in their characterization. The presence of molecules on the surface, in particular long molecules such as polymer chains, can affect both the electrophoresis, diffusion, and interaction of the pore surface. Self-consistent field theory (SCFT) can be a useful tool to be used to predict the conformation of the chains as a function of the brush and solvent properties, particle geometry, and confinement effect. Electrophoretic mobility of grafted particles also is a field in expansion (OHSHIMA, 2016; DOANE et al., 2011), and the correct modeling of these particles during translocation can lead to an advance in nanopore sensing.

8.1.0.6
Multiparticle Simulations

Under typical concentrations used in nanopore sensing considering particles without interactions with each other and the pore, the probability of multiple particles translocating the pore is very low (section 1.3.4). However, under higher concentrations and depending on the interactions of the surface, this effect can become more visible. The DMC code is ready for computing the dynamics of multiple particle events, with the rod contact algorithm by Vega e Lago (1994). However, to compute the current even for two particles, an exponential multiplication of PNP simulations would be needed.

8.1.0.7
Nanoparticle Dispersion in Salt Solutions

The salt concentration can greatly affect the translocation process and represent a barrier to performing the measurements. Higher salt concentrations result in higher ionic currents, a desirable characteristic from the standpoint of pulse detection. However, the screening effect on particle surface charge can result in particle aggregation, as was the case with many trials in the experiments done during this research. Experiments can be done in reduced salt concentrations. However, the detection of the pulses is more difficult to obtain and prone to distortions. Lower concentrations also highlight the effect of the electric double layer, which can be an interesting phenomenon to explore but also can be of difficult interpretation, as seen in Chapter 3. Although the stability of nanoparticles is a very broad field, studies focused on strategies for dispersion of common nanoparticles under convenient salt concentration ranges can help the development of nanopore sensing.

8.2
Concluding Remarks

Nanpore sensing is a promising tool to characterize nanoparticles with high throughput and measure one particle at a time. Going forward, smaller and more automated/robust devices, cheaper (even disposable) membranes with highly defined geometries, and a better understanding of the relationships between the electrical signal and particles, membrane, solution, and device properties are needed. Combined efforts in modeling, simulation, and experimental development can help these tools to become more accessible and reliable and get to the level of maturity of currently established characterization techniques.

Bibliography

AI, Y.; QIAN, S. Electrokinetic particle translocation through a nanopore. **Phys. Chem. Chem. Phys.**, Royal Society of Chemistry (RSC), v. 13, n. 9, p. 4060, 2011. Disponível em: <https://doi.org/10.1039%2Fc0cp02267e>.

AKAHORI, R. et al. Target DNA detection by solid-state nanopores using gold nanoparticle probes. **Japanese Journal of Applied Physics**, IOP Publishing, v. 59, n. 10, p. 107001, 2020. ISSN 13474065. Disponível em: <http://dx.doi.org/10.35848/1347-4065/abb4a9>.

ANDERSON, W. et al. A comparative study of submicron particle sizing platforms: Accuracy, precision and resolution analysis of polydisperse particle size distributions. **Journal of Colloid and Interface Science**, Elsevier Inc., v. 405, p. 322–330, 2013. ISSN 00219797. Disponível em: <http://dx.doi.org/10.1016/j.jcis.2013.02.030>.

ARIMA, A. et al. Selective detections of single-viruses using solid-state nanopores. **Scientific Reports**, Springer Science and Business Media {LLC}, v. 8, n. 1, nov 2018. ISSN 2045-2322. Disponível em: <https://doi.org/10.1038/s41598-018-34665-4http://dx.doi.org/10.1038/s41598-018-34665-4>.

ARJMANDI, N. et al. Measuring the electric charge and zeta potential of nanometer-sized objects using pyramidal-shaped nanopores. **Analytical Chemistry**, v. 84, n. 20, p. 8490–8496, 2012. ISSN 00032700.

BACRI, L. et al. Dynamics of Colloids in Single Solid-State Nanopores. **The Journal of Physical Chemistry B**, American Chemical Society ({ACS}), v. 115, n. 12, p. 2890–2898, mar 2011. Disponível em: <https://doi.org/10.1021/jp200326w>.

BANDARA, Y. M. N. D. Y. et al. Nanopore data analysis: Baseline construction and abrupt change-based multilevel fitting. **Analytical Chemistry**, American Chemical Society (ACS), v. 93, n. 34, p. 11710–11718, ago. 2021. Disponível em: <https://doi.org/10.1021/acs.analchem.1c01646>.

BEAMISH, E. et al. Precise control of the size and noise of solid-state nanopores using high electric fields. **Nanotechnology**, v. 23, 2012.

BEAMISH, E. et al. Fine-tuning the size and minimizing the noise of solid-state nanopores. **Journal of Visualized Experiments**, MyJove Corporation, n. 80, out. 2013. Disponível em: <https://doi.org/10.3791/51081>.

BEUCLER, T. et al. Enforcing Analytic Constraints in Neural Networks Emulating Physical Systems. **Physical Review Letters**, American Physical Society, v. 126, n. 9, p. 98302, 2021. ISSN 10797114. Disponível em: <https://doi.org/10.1103/PhysRevLett.126.098302>.

BLUNDELL, E. L. C. J.; VOGEL, R.; PLATT, M. Particle-by-Particle Charge Analysis of {DNA}-Modified Nanoparticles Using Tunable Resistive Pulse Sensing. **Langmuir**, American Chemical Society ({ACS}), v. 32, n. 4, p. 1082–1090, jan 2016. Disponível em: <https://doi.org/10.1021/acs.langmuir.5b03024>.

CAMPOS, E. et al. Sensing Single Mixed-Monolayer Protected Gold Nanoparticles by the α-Hemolysin Nanopore. **Analytical Chemistry**, American Chemical Society ({ACS}), v. 85, n. 21, p. 10149–10158, oct 2013. Disponível em: <https://doi.org/10.1021/ac4014836>.

CHANTIWAS, R. et al. Flexible fabrication and applications of polymer nanochannels and nanoslits. **Chemical Society Reviews**, Royal Society of Chemistry ({RSC}), v. 40, n. 7, p. 3677, 2011. Disponível em: <https://doi.org/10.1039/c0cs00138d>.

COGLITORE, D. et al. Revealing the nanoparticle-protein corona with a solid-state nanopore. **Materials**, v. 12, n. 21, p. 1–11, 2019. ISSN 19961944.

COLBY, A. H.; COLSON, Y. L.; GRINSTAFF, M. W. Microscopy and tunable resistive pulse sensing characterization of the swelling of pH-responsive, polymeric expansile nanoparticles. **Nanoscale**, v. 5, n. 8, p. 3496–3504, 2013. ISSN 20403364.

COUMANS, F. A. W. et al. Reproducible extracellular vesicle size and concentration determination with tunable resistive pulse sensing. **Journal of Extracellular Vesicles**, Informa {UK} Limited, v. 3, n. 1, p. 25922, jan 2014. Disponível em: <https://doi.org/10.3402/jev.v3.25922>.

CUETOS, A.; PATTI, A. Equivalence of brownian dynamics and dynamic monte carlo simulations in multicomponent colloidal suspensions. **Physical Review E**, American Physical Society (APS), v. 92, n. 2, ago. 2015. Disponível em: <https://doi.org/10.1103/physreve.92.022302>.

DARVISH, A. et al. Nanoparticle mechanics: Deformation detection: Via nanopore resistive pulse sensing. **Nanoscale**, Royal Society of Chemistry, v. 8, n. 30, p. 14420–14431, 2016. ISSN 20403372.

DARVISH, A.; GOYAL, G.; KIM, M. Sensing, capturing, and interrogation of single virus particles with solid state nanopores. **Advances in Global Health through Sensing Technologies 2015**, v. 9490, p. 94900M, 2015. ISSN 1996756X.

DEBLOIS, R. W.; BEAN, C. P. Counting and sizing of submicron particles by the resistive pulse technique. **Review of Scientific Instruments**, AIP Publishing, v. 41, n. 7, p. 909–916, jul. 1970. Disponível em: <https://doi.org/10.1063/1.1684724>.

DEBLOIS, R. W.; BEAN, C. P.; WESLEY, R. K. Electrokinetic measurements with submicron particles and pores by the resistive pulse technique. **Journal of Colloid And Interface Science**, v. 61, n. 2, p. 323–335, 1977. ISSN 00219797.

DOANE, T. L. et al. Nanoparticle $zeta$-potentials. **Accounts of Chemical Research**, American Chemical Society (ACS), v. 45, n. 3, p. 317–326, nov. 2011. Disponível em: <https://doi.org/10.1021/ar200113c>.

EDWARDS, M. A. et al. High-Speed Multipass Coulter Counter with Ultrahigh Resolution. **ACS Nano**, v. 9, n. 12, p. 12274–12282, 2015. ISSN 1936086X.

EGGENBERGER, O. M.; MAYER, M. Surface coatings for solid-state nanopores. **Nanoscale**, Royal Society of Chemistry, v. 11, p. 19636–19657, 2019.

FORSTATER, J. H. et al. MOSAIC: A modular single-molecule analysis interface for decoding multistate nanopore data. **Analytical Chemistry**, American Chemical Society (ACS), v. 88, n. 23, p. 11900–11907, nov. 2016. Disponível em: <https://doi.org/10.1021/acs.analchem.6b03725>.

FRAIKIN, J.-L. et al. A high-throughput label-free nanoparticle analyser. **Nature Nanotech**, Springer Science and Business Media LLC, v. 6, n. 5, p. 308–313, mar 2011. Disponível em: <https://doi.org/10.1038%2Fnnano.2011.24>.

GOYAL, G.; FREEDMAN, K. J.; KIM, M. J. Gold nanoparticle translocation dynamics and electrical detection of single particle diffusion using solid-state nanopores. **Anal. Chem.**, American Chemical Society (ACS), v. 85, n. 17, p. 8180–8187, aug 2013. Disponível em: <https://doi.org/10.1021%2Fac4012045>.

GRABAREK, A. D. et al. Critical Evaluation of Microfluidic Resistive Pulse Sensing for Quantification and Sizing of Nanometer- and Micrometer-Sized Particles in Biopharmaceutical Products. **Journal of Pharmaceutical Sciences**, Elsevier Ltd, v. 108, n. 1, p. 563–573, 2019. ISSN 15206017. Disponível em: <https://doi.org/10.1016/j.xphs.2018.08.020>.

GRAF, M. et al. Fabrication and practical applications of molybdenum disulfide nanopores. **Nature Protocols**, Springer Science and Business Media LLC, v. 14, n. 4, p. 1130–1168, mar. 2019. Disponível em: <https://doi.org/10.1038/s41596-019-0131-0>.

GROOT, G. W. de et al. Switching transport through nanopores with pH-responsive polymer brushes for controlled ion permeability. **ACS Applied Materials & Interfaces**, American Chemical Society (ACS), v. 5, n. 4, p. 1400–1407, fev. 2013. Disponível em: <https://doi.org/10.1021/am302820y>.

HALL, A. R. et al. Translocation of single-wall carbon nanotubes through solid-state nanopores. **Nano Letters**, v. 11, n. 6, p. 2446–2450, 2011. ISSN 15306984.

HALL, J. E. Access resistance of a small circular pore. **Journal of General Physiology**, Rockefeller University Press, v. 66, n. 4, p. 531–532, oct 1975. Disponível em: <https://doi.org/10.1085%2Fjgp.66.4.531>.

HARMS, Z. D. et al. Nanofluidic devices with two pores in series for resistive-pulse sensing of single virus capsids. **Analytical Chemistry**, v. 83, n. 24, p. 9573–9578, 2011. ISSN 00032700.

HE, F. et al. Detection of gold nanoparticles based on solid-state nanopore. **Conference Program Digest - 7th International Conference on Manipulation, Manufacturing and Measurement on the Nanoscale, IEEE 3M-NANO 2017**, v. 2017-Janua, p. 388–391, 2017.

HOLDEN, D. A. et al. Resistive pulse analysis of microgel deformation during nanopore translocation. **Journal of Physical Chemistry C**, v. 115, n. 7, p. 2999–3004, 2011. ISSN 19327447.

HOLDEN, D. A.; WATKINS, J. J.; WHITE, H. S. Resistive-pulse detection of multilamellar liposomes. **Langmuir**, v. 28, n. 19, p. 7572–7577, 2012. ISSN 07437463.

ITO, T. et al. Comparison of nanoparticle size and electrophoretic mobility measurements using a carbon-nanotube-based coulter counter, dynamic light scattering, transmission electron microscopy, and phase analysis light scattering. **Langmuir**, v. 20, n. 16, p. 6940–6945, 2004. ISSN 07437463.

JUBERY, T. Z. et al. Modeling and simulation of nanoparticle separation through a solid-state nanopore. **Electrophoresis**, v. 33, n. 2, p. 325–333, 2012. ISSN 01730835.

KARNIADAKIS, G. E. et al. Physics-informed machine learning. **Nature Reviews Physics**, v. 3, n. 6, p. 422–440, 2021. ISSN 25225820.

KIKUCHI, K. et al. Metropolis monte carlo method as a numerical technique to solve the fokker—planck equation. **Chemical Physics Letters**, v. 185, n. 3, p. 335–338, 1991. ISSN 0009-2614. Disponível em: <https://www.sciencedirect.com/science/article/pii/S000926149185070D>.

KIM, Y. et al. Probing nanoparticle translocation across the permeable endothelium in experimental atherosclerosis. **Proceedings of the National Academy of Sciences**, Proceedings of the National Academy of Sciences, v. 111, n. 3, p. 1078–1083, jan 2014. Disponível em: <https://doi.org/10.1073/pnas.1322725111>.

KISHIMOTO, S. et al. Crucial Role of Out-of-Pore Resistance on Temporal Response of Ionic Current in Nanopore Sensors. **ACS Sensors**, v. 5, n. 6, p. 1597–1603, 2020. ISSN 23793694.

KOZAK, D. et al. Simultaneous Size and ζ - Potential Measurements of Individual Nanoparticles in Dispersion Using Size-Tunable Pore Sensors. **ACS Nano**, v. 6, n. 8, p. 6990–6997, 2012.

KURON, M. et al. Moving charged particles in lattice boltzmann-based electrokinetics. **The Journal of Chemical Physics**, AIP Publishing, v. 145, n. 21, p. 214102, dez. 2016. Disponível em: <https://doi.org/10.1063/1.4968596>.

LAN, W. J. et al. Pressure-driven nanoparticle transport across glass membranes containing a conical-shaped nanopore. **Journal of Physical Chemistry C**, v. 115, n. 38, p. 18445–18452, 2011. ISSN 19327447.

LAN, W.-J. et al. Pressure-Driven Nanoparticle Transport across Glass Membranes Containing a Conical-Shaped Nanopore. **The Journal of Physical Chemistry C**, American Chemical Society ({ACS}), v. 115, n. 38, p. 18445–18452, aug 2011. Disponível em: <https://doi.org/10.1021/jp204839j>.

LAN, W.-J. et al. Nanoparticle Transport in Conical-Shaped Nanopores. **Analytical Chemistry**, American Chemical Society ({ACS}), v. 83, n. 10, p. 3840–3847, may 2011. Disponível em: <https://doi.org/10.1021/ac200312n>.

LAN, W. J. et al. Effect of surface charge on the resistive pulse waveshape during particle translocation through glass nanopores. **Journal of Physical Chemistry C**, v. 118, n. 5, p. 2726–2734, 2014. ISSN 19327447.

LAN, W. J.; WHITE, H. S. Diffusional motion of a particle translocating through a nanopore. **ACS Nano**, v. 6, n. 2, p. 1757–1765, 2012. ISSN 19360851.

LANE, R. E. et al. Analysis of exosome purification methods using a model liposome system and tunable-resistive pulse sensing. **Scientific Reports**, v. 5, p. 1–7, 2015. ISSN 20452322.

LEE, J. S. et al. Multiple consecutive recapture of rigid nanoparticles using a solid-state nanopore sensor. **Electrophoresis**, v. 39, n. 5-6, p. 833–843, 2018. ISSN 15222683.

LEE, J. S. et al. Stiffness measurement of nanosized liposomes using solid-state nanopore sensor with automated recapturing platform. **Electrophoresis**, Wiley, v. 40, n. 9, p. 1337–1344, jan 2019. Disponível em: <https://doi.org/10.1002/elps.201800476>.

LENART, W. R. et al. Translocation of soft phytoglycogen nanoparticles through solid-state nanochannels. **Journal of Materials Chemistry B**, Royal Society of Chemistry ({RSC}), v. 7, n. 41, p. 6428–6437, 2019. Disponível em: <https://doi.org/10.1039/c9tb01048c>.

LIANG, S. et al. Noise in nanopore sensors: Sources, models, reduction, and benchmarking. **Nanotechnology and Precision Engineering**, AIP Publishing, v. 3, n. 1, p. 9–17, mar. 2020. Disponível em: <https://doi.org/10.1016/j.npe.2019.12.008>.

LIGNELL, D. **Multilinear interpolation in C++**. 2020. <https://github.com/BYUignite/multilinear_interpolation>. Accessed: 2022-03-31.

LIOT, O. et al. Transport of nano-objects in narrow channels: influence of Brownian diffusion, confinement and particle nature. **Journal of Physics: Condensed Matter**, {IOP} Publishing, v. 30, n. 23, p. 234001, may 2018. Disponível em: <https://doi.org/10.1088/1361-648x/aac0af>.

LIU, Y. W.; PENNATHUR, S.; MEINHART, C. D. Electrophoretic mobility of a spherical nanoparticle in a nanochannel. **Physics of Fluids**, v. 26, n. 11, p. 1–12, 2014. ISSN 10897666.

MAUGI, R. et al. A methodology for characterising nanoparticle size and shape using nanopores. **Nanoscale**, Royal Society of Chemistry (RSC), v. 12, n. 1, p. 262–270, 2020. Disponível em: <https://doi.org/10.1039/c9nr09100a>.

MCMULLEN, A. et al. Buckling Causes Nonlinear Dynamics of Filamentous Viruses Driven through Nanopores. **Physical Review Letters**, American Physical

Society, v. 120, n. 7, p. 78101, 2018. ISSN 10797114. Disponível em: <https://doi.org/10.1103/PhysRevLett.120.078101>.

MCMULLEN, A. et al. Stiff filamentous virus translocations through solid-state nanopores. **Nature Communications**, Springer Science and Business Media {LLC}, v. 5, n. 1, jun 2014. Disponível em: <https://doi.org/10.1038/ncomms5171>.

MCMULLEN, A. J.; TANG, J. X.; STEIN, D. Nanopore measurements of filamentous viruses reveal a sub-nanometer-scale stagnant fluid layer. **ACS Nano**, American Chemical Society (ACS), v. 11, n. 11, p. 11669–11677, nov 2017.

MENARD, L. D.; RAMSEY, J. M. Fabrication of sub-5 nm nanochannels in insulating substrates using focused ion beam milling. **Nano Letters**, American Chemical Society (ACS), v. 11, n. 2, p. 512–517, fev. 2011. Disponível em: <https://doi.org/10.1021/nl103369g>.

MICHAELIDES, E. E. Nanoparticle diffusivity in narrow cylindrical pores. **International Journal of Heat and Mass Transfer**, Elsevier Ltd, v. 114, p. 607–612, 2017. ISSN 00179310. Disponível em: <http://dx.doi.org/10.1016/j.ijheatmasstransfer.2017.06.098>.

MITSCHA-BAUDE, G. et al. Adaptive and iterative methods for simulations of nanopores with the PNP–Stokes equations. **Journal of Computational Physics**, Elsevier Inc., v. 338, p. 452–476, 2017. ISSN 10902716. Disponível em: <http://dx.doi.org/10.1016/j.jcp.2017.02.072>.

MUTHUKUMAR, M. **Polymer Translocation**. [S.l.: s.n.], 2011. ISBN 9781420075175.

NIE, X.-L. et al. Recognition of plastic nanoparticles using a single gold nanopore fabricated at the tip of a glass nanopipette. **Chemical Communications**, Royal Society of Chemistry ({RSC}), v. 55, n. 45, p. 6397–6400, 2019. Disponível em: <https://doi.org/10.1039/c9cc01358j>.

NIEDZWIECKI, D. J. et al. Detection of single analyte and environmental samples with silicon nitride nanopores: Antarctic dirt particulates and DNA in artificial seawater. **Review of Scientific Instruments**, AIP Publishing, v. 91, n. 3, p. 031301, mar. 2020. Disponível em: <https://doi.org/10.1063/1.5138210>.

O'BRIEN, R. W.; WHITE, L. R. Electrophoretic mobility of a spherical colloidal particle. **Journal of the Chemical Society, Faraday Transactions 2**, Royal Society of Chemistry (RSC), v. 74, p. 1607, 1978. Disponível em: <https://doi.org/10.1039/f29787401607>.

OEFFELEN, L. van et al. Modelling solid-state nanopores with a combination of the poisson-nernst-planck equations and brownian dynamics. In: **Nanopores for Bioanalytical Applications**. Royal Society of Chemistry, 2012. p. 51–56. Disponível em: <https://doi.org/10.1039/9781849735278-00051>.

OHSHIMA, H. A simple expression for henry's function for the retardation effect in electrophoresis of spherical colloidal particles. **Journal of Colloid And Interface Science**, v. 168, n. 1, p. 269–271, 1994. ISSN 00219797.

OHSHIMA, H. Electrophoresis. In: **Reference Module in Chemistry, Molecular Sciences and Chemical Engineering**. Elsevier, 2016. p. 873–877. ISBN 978-0-12-409547-2. Disponível em: <https://www.sciencedirect.com/science/article/pii/B9780124095472121997>.

PATTI, A.; CUETOS, A. Brownian dynamics and dynamic Monte Carlo simulations of isotropic and liquid crystal phases of anisotropic colloidal particles: A comparative study. **Physical Review E - Statistical, Nonlinear, and Soft Matter Physics**, v. 86, n. 1, p. 1–9, 2012. ISSN 15393755.

PENG, R.; LI, D. Fabrication of polydimethylsiloxane (PDMS) nanofluidic chips with controllable channel size and spacing. **Lab on a Chip**, Royal Society of Chemistry (RSC), v. 16, n. 19, p. 3767–3776, 2016. Disponível em: <https://doi.org/10.1039/c6lc00867d>.

PEVARNIK, M. et al. Polystyrene particles reveal pore substructure as they translocate. **ACS Nano**, v. 6, n. 8, p. 7295–7302, 2012. ISSN 19360851.

PEVARNIK, M. et al. Particle deformation and concentration polarization in electroosmotic transport of hydrogels through pores. **ACS Nano**, v. 7, n. 4, p. 3720–3728, 2013. ISSN 19360851.

PLATT, M.; WILLMOTT, G. R.; LEE, G. U. Resistive Pulse Sensing of Analyte-Induced Multicomponent Rod Aggregation Using Tunable Pores. **Small**, Wiley, v. 8, n. 15, p. 2436–2444, may 2012. Disponível em: <https://doi.org/10.1002/smll.201200058>.

PRABHU, A. S. et al. Chemically modified solid state nanopores for high throughput nanoparticle separation. **Journal of Physics: Condensed Matter**, IOP Publishing, v. 22, n. 45, p. 454107, out. 2010. Disponível em: <https://doi.org/10.1088/0953-8984/22/45/454107>.

QIAN, S.; WANG, A.; AFONIEN, J. K. Electrophoretic motion of a spherical particle in a converging-diverging nanotube. **Journal of Colloid and Interface Science**, v. 303, n. 2, p. 579–592, 2006. ISSN 00219797.

QIAO, L.; IGNACIO, M.; SLATER, G. W. Voltage-driven translocation: Defining a capture radius. **Journal of Chemical Physics**, AIP Publishing, LLC, v. 151, n. 24, p. 1–11, 2019. ISSN 00219606. Disponível em: <https://doi.org/10.1063/1.5134076>.

QIAO, L.; SLATER, G. W. Capture of rod-like molecules by a nanopore: Defining an "orientational capture radius". **Journal of Chemical Physics**, AIP Publishing, LLC, v. 152, n. 14, p. 1–6, 2020. ISSN 00219606. Disponível em: <https://doi.org/10.1063/5.0002044>.

QIN, Z.; ZHE, J.; WANG, G.-X. Effects of particle's off-axis position, shape, orientation and entry position on resistance changes of micro coulter counting devices. **Measurement Science and Technology**, IOP Publishing, v. 22, n. 4, p. 045804, mar. 2011. Disponível em: <https://doi.org/10.1088/0957-0233/22/4/045804>.

RAILLON, C. et al. Fast and automatic processing of multi-level events in nanopore translocation experiments. **Nanoscale**, Royal Society of Chemistry (RSC), v. 4, n. 16, p. 4916, 2012. Disponível em: <https://doi.org/10.1039/c2nr30951c>.

RAISSI, M.; PERDIKARIS, P.; KARNIADAKIS, G. E. Physics-informed neural networks: A deep learning framework for solving forward and inverse problems involving nonlinear partial differential equations. **Journal of Computational Physics**, Elsevier Inc., v. 378, p. 686–707, 2019. ISSN 10902716. Disponível em: <https://doi.org/10.1016/j.jcp.2018.10.045>.

REBOUX, S. et al. Lattice-Boltzmann simulations of ionic current modulation by DNA translocation. **Journal of Chemical Theory and Computation**, v. 2, n. 3, p. 495–503, 2006. ISSN 15499618.

ROBERTS, G. S. et al. Tunable pores for measuring concentrations of synthetic and biological nanoparticle dispersions. **Biosensors and Bioelectronics**, Elsevier B.V., v. 31, n. 1, p. 17–25, 2012. ISSN 09565663. Disponível em: <http://dx.doi.org/10.1016/j.bios.2011.09.040>.

ROBINSON, D. A. et al. Effects of Instrumental Filters on Electrochemical Measurement of Single-Nanoparticle Collision Dynamics. **ChemElectroChem**, Wiley, v. 5, n. 20, p. 3059–3067, jul 2018. Disponível em: <https://doi.org/10.1002/celc.201800696>.

ROMAN, J. et al. Functionalized Solid-State Nanopore Integrated in a Reusable Microfluidic Device for a Better Stability and Nanoparticle Detection. **{ACS} Applied Materials & Interfaces**, American Chemical Society ({ACS}), v. 9, n. 48, p. 41634–41640, nov 2017. Disponível em: <https://doi.org/10.1021/acsami.7b14717>.

RYU, J. et al. Sensors and Actuators B : Chemical Ultralow-aspect-ratio micropore sensor for a particle translocation : Critical role of the access region. **Sensors & Actuators: B. Chemical**, Elsevier, v. 288, n. January, p. 454–459, 2019. ISSN 0925-4005. Disponível em: <https://doi.org/10.1016/j.snb.2019.02.090>.

RYUZAKI, S. et al. Rapid structural analysis of nanomaterials in aqueous solutions. **Nanotechnology**, {IOP} Publishing, v. 28, n. 15, p. 155501, mar 2017. ISSN 1361-6528. Disponível em: <https://doi.org/10.1088/1361-6528/aa5e66http://dx.doi.org/10.1088/1361-6528/aa5e66>.

SHI, L.; RANA, A.; ESFANDIARI, L. A low voltage nanopipette dielectrophoretic device for rapid entrapment of nanoparticles and exosomes extracted from plasma of healthy donors. **Scientific Reports**, Springer US, v. 8, n. 1, p. 1–12, 2018. ISSN 20452322. Disponível em: <http://dx.doi.org/10.1038/s41598-018-25026-2>.

SHI, W.; FRIEDMAN, A. K.; BAKER, L. A. Nanopore Sensing. **Analytical Chemistry**, American Chemical Society ({ACS}), v. 89, n. 1, p. 157–188, nov 2016. Disponível em: <https://doi.org/10.1021/acs.analchem.6b04260>.

SI, W. et al. Shape characterization and discrimination of single nanoparticles using solid-state nanopores. **The Analyst**, Royal Society of Chemistry (RSC), v. 145, n. 5, p. 1657–1666, 2020. Disponível em: <https://doi.org/10.1039/c9an01889a>.

SIKORA, A.; SHARD, A. G.; MINELLI, C. Size and ζ-Potential Measurement of Silica Nanoparticles in Serum Using Tunable Resistive Pulse Sensing. **Langmuir**, v. 32, n. 9, p. 2216–2224, 2016. ISSN 15205827.

SLOTBOOM, J.; de Graaff, H. Measurements of bandgap narrowing in si bipolar transistors. **Solid-State Electronics**, v. 19, n. 10, p. 857–862, 1976. ISSN 0038-1101. Disponível em: <https://www.sciencedirect.com/science/article/pii/0038110176900435>.

SMEETS, R. M. M. et al. Salt Dependence of Ion Transport and {DNA} Translocation through Solid-State Nanopores. **Nano Letters**, American Chemical Society ({ACS}), v. 6, n. 1, p. 89–95, jan 2006. Disponível em: <https://doi.org/10.1021/nl052107w>.

SOMERVILLE, J. A. et al. Size and charge characterisation of a submicrometre oil-in-water emulsion using resistive pulse sensing with tunable pores. **Journal of Colloid and Interface Science**, v. 394, n. 1, p. 243–251, 2013. ISSN 00219797. Disponível em: <http://dx.doi.org/10.1016/j.jcis.2012.11.071>.

SOUZA, T. G.; CIMINELLI, V. S.; MOHALLEM, N. D. A comparison of TEM and DLS methods to characterize size distribution of ceramic nanoparticles. **Journal of Physics: Conference Series**, v. 733, n. 1, p. 1–5, 2016. ISSN 17426596.

STARK, W. J. et al. Industrial applications of nanoparticles. **Chemical Society Reviews**, Royal Society of Chemistry (RSC), v. 44, n. 16, p. 5793–5805, 2015. Disponível em: <https://doi.org/10.1039/c4cs00362d>.

SUN, L.; CROOKS, R. M. Single carbon nanotube membranes: a well-defined model for studying mass transport through nanoporous materials. **Journal of the American Chemical Society**, American Chemical Society (ACS), v. 122, n. 49, p. 12340–12345, nov. 2000. Disponível em: <https://doi.org/10.1021/ja002429w>.

SWAN, J. W.; FURST, E. M. A simpler expression for henry's function describing the electrophoretic mobility of spherical colloids. **Journal of Colloid and Interface Science**, Elsevier BV, v. 388, n. 1, p. 92–94, dez. 2012. Disponível em: <https://doi.org/10.1016/j.jcis.2012.08.026>.

TABARD-COSSA, V. et al. Noise analysis and reduction in solid-state nanopores. **Nanotechnology**, IOP Publishing, v. 18, n. 30, p. 305505, jun 2007. Disponível em: <https://doi.org/10.1088%2F0957-4484%2F18%2F30%2F305505>.

TAN, S. et al. Single Nanoparticle Translocation Through Chemically Modified Solid Nanopore. **Nanoscale Research Letters**, Nanoscale Research Letters, v. 11, n. 1, p. 1–10, 2016. ISSN 1556276X. Disponível em: <http://dx.doi.org/10.1186/s11671-016-1255-6>.

TANAKA, S. et al. Tailoring particle translocation via dielectrophoresis in pore channels. **Nature Publishing Group**, Nature Publishing Group, n. August, p. 1–8, 2016.

TANIGUCHI, M. Combination of single-molecule electrical measurements and machine learning for the identification of single biomolecules. **ACS Omega**,

American Chemical Society (ACS), v. 5, n. 2, p. 959–964, jan. 2020. Disponível em: <https://doi.org/10.1021/acsomega.9b03660>.

TEREJÁNSZKY, P. et al. Calibration-less sizing and quantitation of polymeric nanoparticles and viruses with quartz nanopipets. **Analytical Chemistry**, v. 86, n. 10, p. 4688–4697, 2014. ISSN 15206882.

TIRADO, M. M.; MARTÍNEZ, C. L.; TORRE, J. G. de la. Comparison of theories for the translational and rotational diffusion coefficients of rod-like macromolecules. application to short DNA fragments. **The Journal of Chemical Physics**, AIP Publishing, v. 81, n. 4, p. 2047–2052, aug 1984. Disponível em: <https://doi.org/10.1063%2F1.447827>.

TSUTSUI, M. et al. Particle Trajectory-Dependent Ionic Current Blockade in Low-Aspect-Ratio Pores. **{ACS} Nano**, American Chemical Society ({ACS}), v. 10, n. 1, p. 803–809, dec 2015. Disponível em: <https://doi.org/10.1021/acsnano.5b05906>.

TSUTSUI, M. et al. Particle trajectory-dependent ionic current blockade in low-aspect-ratio pores. **ACS Nano**, v. 10, n. 1, p. 803–809, 2016. ISSN 1936086X.

TSUTSUI, M. et al. High-throughput single nanoparticle detection using a feed-through channel-integrated nanopore. **Nanoscale**, Royal Society of Chemistry ({RSC}), v. 11, n. 43, p. 20475–20484, 2019. Disponível em: <https://doi.org/10.1039/c9nr07039g>.

TSUTSUI, M. et al. Temporal Response of Ionic Current Blockade in Solid-State Nanopores. **ACS Applied Materials and Interfaces**, v. 10, n. 40, p. 34751–34757, 2018. ISSN 19448252.

TSUTSUI, M. et al. Particle Capture in Solid-State Multipores. **ACS Sensors**, v. 3, n. 12, p. 2693–2701, 2018. ISSN 23793694.

TSUTSUI, M. et al. Electric field interference and bimodal particle translocation in nano-integrated multipores. **Nanoscale**, Royal Society of Chemistry, v. 11, p. 7547–7553, 2019. ISSN 2040-3372. Disponível em: <http://dx.doi.org/10.1039/c8nr08632j>.

TU, J. et al. EasyNanopore: A ready-to-use processing software for translocation events in nanopore translocation experiments. **Langmuir**, American Chemical Society (ACS), v. 37, n. 33, p. 10177–10182, ago. 2021. Disponível em: <https://doi.org/10.1021/acs.langmuir.1c01597>.

URAM, J. D. et al. Submicrometer pore-based characterization and quantification of antibody-virus interactions. **Small**, v. 2, n. 8-9, p. 967–972, 2006. ISSN 16136810.

VEGA, C.; LAGO, S. A fast algorithm to evaluate the shortest distance between rods. **Computers & Chemistry**, v. 18, n. 1, p. 55–59, 1994. ISSN 0097-8485. Disponível em: <https://www.sciencedirect.com/science/article/pii/0097848594800235>.

VENTA, K. E. et al. Gold nanorod translocations and charge measurement through solid-state nanopores. **Nano Letters**, v. 14, n. 9, p. 5358–5364, 2014. ISSN 15306992.

VENTA, K. E. et al. Gold Nanorod Translocations and Charge Measurement through Solid-State Nanopores. **Nano Letters**, American Chemical Society ({ACS}), v. 14, n. 9, p. 5358–5364, aug 2014. Disponível em: <https://doi.org/10.1021/nl502448s>.

VOGEL, R. et al. A variable pressure method for characterizing nanoparticle surface charge using pore sensors. **Analytical Chemistry**, v. 84, n. 7, p. 3125–3131, 2012. ISSN 00032700. Disponível em: <https://doi.org/10.1038/s41598-017-14981-x>.

VOGEL, R. et al. Quantitative sizing of nano/microparticles with a tunable elastomeric pore sensor. **Analytical Chemistry**, v. 83, n. 9, p. 3499–3506, 2011. ISSN 00032700.

WANG, L.; BENICEWICZ, B. C. Synthesis and characterization of dye-labeled poly(methacrylic acid) grafted silica nanoparticles. **ACS Macro Letters**, 2013. ISSN 21611653.

WEN, C.; DEMATTIES, D.; ZHANG, S.-L. A guide to signal processing algorithms for nanopore sensors. **ACS Sensors**, American Chemical Society (ACS), v. 6, n. 10, p. 3536–3555, out. 2021. Disponível em: <https://doi.org/10.1021/acssensors.1c01618>.

WEN, C. et al. Group behavior of nanoparticles translocating multiple nanopores. **Analytical Chemistry**, American Chemical Society (ACS), v. 90, n. 22, p. 13483–13490, out. 2018. Disponível em: <https://doi.org/10.1021/acs.analchem.8b03408>.

WILLMOTT, G. R. et al. Use of tunable nanopore blockade rates to investigate colloidal dispersions. **Journal of Physics Condensed Matter**, v. 22, n. 45, 2010. ISSN 09538984.

WILLMOTT, G. R.; YU, S. S.; VOGEL, R. Pressure dependence of particle transport through resizable nanopores. **ICONN 2010 - Proceedings of the 2010 International Conference on Nanoscience and Nanotechnology**, IEEE, p. 128–131, 2010.

WU, H. et al. Translocation of Rigid Rod-Shaped Virus through Various Solid-State Nanopores. **Analytical Chemistry**, American Chemical Society ({ACS}), v. 88, n. 4, p. 2502–2510, feb 2016. ISSN 15206882. Disponível em: <https://doi.org/10.1021/acs.analchem.5b04905>.

YANG, L.; SHAMI, A. On hyperparameter optimization of machine learning algorithms: Theory and practice. **Neurocomputing**, Elsevier BV, v. 415, p. 295–316, nov. 2020. Disponível em: <https://doi.org/10.1016/j.neucom.2020.07.061>.

YUSKO, E. C. et al. Controlling protein translocation through nanopores with bio-inspired fluid walls. **Nature Nanotechnology**, Springer Science and Business Media LLC, v. 6, n. 4, p. 253–260, fev. 2011. Disponível em: <https://doi.org/10.1038/nnano.2011.12>.

ZHANG, H. et al. Bioinspired artificial single ion pump. **Journal of the American Chemical Society**, American Chemical Society (ACS), v. 135, n. 43, p. 16102–16110, jul. 2013. Disponível em: <https://doi.org/10.1021/ja4037669>.

ZHANG, Y. et al. Multipass Resistive-Pulse Observations of the Rotational Tumbling of Individual Nanorods. **J. Phys. Chem. C**, American Chemical Society, v. 120, n. 37, p. 20781–20788, may 2016.

ZHANG, Y. et al. Fabrication of nanochannels. **Materials**, MDPI AG, v. 8, n. 9, p. 6277–6308, set. 2015. Disponível em: <https://doi.org/10.3390/ma8095304>.